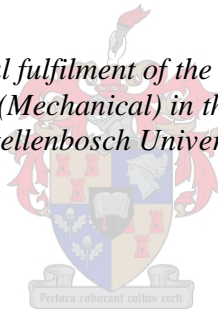# The Performance and Simulation of a Spark-Ignition Engine Employing an Aftermarket Engine Control Unit

by
André Daniel Brink

Thesis presented in partial fulfilment of the requirements for the degree of Master of Engineering (Mechanical) in the Faculty of Engineering at Stellenbosch University

Supervisor: Mr Richard Walter Haines

April 2019

Declaration

By submitting this thesis electronically, I declare that the entirety of the work contained therein is my own, original work, that I am the sole author thereof (save to the extent explicitly otherwise stated), that reproduction and publication thereof by Stellenbosch University will not infringe any third party rights and that I have not previously in its entirety or in part submitted it for obtaining any qualification.

Date: April 2019

Abstract

This thesis discusses the development and upgrade of an internal combustion spark-ignition engine test cell. Existing test cell equipment was upgraded and additional sensors were installed onto the engine. Engine refurbishment was also performed.

The baseline engine performance was then tested using the original manufacturer equipment engine control unit. An aftermarket ECU was later installed onto the engine to allow for greater control of engine performance parameters.

The influence of spark-ignition timing and air-fuel ratio on engine performance and in-cylinder pressure was studied. Engine power and efficiency were greatly affected by these parameters.

A single-zone and two-zone heat-release model was implemented to analyse the influence of spark-ignition timing and air-fuel ratio on combustion. The single-zone model provided satisfactory results when compared to the two-zone model.

Commercially available software was used to simulate the engine performance and was found to be within 15% of experimental results for high power test conditions.

Opsomming

In hierdie tesis word die ontwikkeling en opgradering van 'n interne verbranding vonkontsteking enjin toetssel. Die bestaande toetssel se toerusting was opgradeer en bykoemende sensors was geinstalleer in die enjin. Daar is ook opknappings werk aan die enjin gedoen.

Die oorspronklike vervaardige enjin-kontrole eenheid was gebruik om die basislyn van die enjin optrede te bepaal. Op 'n later stadium is 'n na-mark-enjinkontrole eenheid (ECU) geinstalleer om sodoende beter kontrole te kan handhaaf op die enjin se prestasie.

Die invloed van die vonkontsteking tydsberekening en die brandstof verhouding sowel op enjin prestasie as ook die druk binne-in die silinder was bestudeer. Die enjinkrag en doeltreffendheid was grootliks beinvloed deur hierdie grense.

'n Enkel sone en dubbel sone hittevrystellings model is geïmplimenteer om die uitwerking van vonkontstekingstyd en lug-brandstof verhouding op verbranding te aniliseer. Die enkel sone hittevrystellings model het bevredigende resultate gelewer in vergelyking met die dubbel sone model.

Kommersiële beskikbare sagteware is gebruik om die enjin prestasie te simuleer. Daar is bevind dat dit binne die 15% van eksperimentele resultate vir hoë krag toetstande was.

Dedication

This thesis is dedicated to Richard Haines, Reynaldo Rodriguez, Julian Stanfliet, Cobus Zietsman, Ferdi Zietsman, and all those who assisted me with this project.

Thank you all for your continued and unwavering support throughout my studies.

Table of Contents

List of Tables

Page

List of Figures

Nomenclature

ATDC	After top dead centre
BMEP	Brake mean effective pressure
BSFC	Brake specific fuel consumption
BTDC	Before top dead centre
COV	Coefficient of variation
COV_{IMEP}	Coefficient of variation for indicated mean effective pressure
EMF	Electromotive force
ECU	Engine control unit
ETA	Engine test automation
FEMP	Friction mean effective pressure
IMEP	Indicated mean effective pressure
LES	Lotus Engine Simulation
MON	Motor octane number
MBT	Maximum brake torque
PLC	Programmable logic controller
PFI	Port fuel injected
RON	Research octane number
RTD	Resistor temperature detector
SI	Spark-ignition
TDC	Top dead centre
$IMEP_{gross}$	Gross indicated mean effective pressure
$IMEP_{net}$	Net indicated mean effective pressure
A	Combustion chamber surface area
D	Load cell moment arm
DI	Direct injection
e	Internal energy
F	Load cell force

h	Enthalpy
HC	Hydrocarbons
k	Thermal conductivity of gas
m	Mass
N	Engine speed
n	Rotational speed
IC	Internal combustion
p	Pressure
R	Specific gas constant
Re	Reynolds number
V	Volume
c_p	Specific heat at constant pressure
c_v	Specific heat at constant volume
D_{cyl}	Cylinder bore
h_{ht}	Heat transfer coefficient
m_{CR}	Mass in crevice
n_{bt}	Brake thermal efficiency
n_c	4 Stroke constant
P_b	Brake power
p_{motor}	Motoring pressure
p_{soc}	Pressure at start of combustion
Q_{net}	Net calorific value of fuel
Q_L	Heat lost
Q_R	Heat released
r_c	Compression ratio
S_{rat}	Wochni open or closed cycle swirl ratio
T_{gas}	Temperature of gas
T_{soc}	Temperature at start of combustion
T_{torque}	Engine Torque
T_{wall}	Temperature of wall
V_{CR}	Crevice volume
V_c	Clearance volume

V_{cyl}	Volume of cylinder
V_d	Displaced volume
V_{soc}	Volume at start of combustion
$\dot{m}_f$	Mass flow rate
$\bar{T}_b$	Temperature of burnt region
$\bar{T}_u$	Temperature of unburnt region
$\bar{U}_{piston}$	Mean piston velocity
$\bar{U}_{swirl}$	Mean swirl velocity
°CA	Degree crank angle
γ	Specific heat ratio
δF	Loss function
ΔP	Pressure differential
θ	Crankshaft angle
ϑ	Angular position
λ	Relative air-fuel ratio
μ	Rod to crank ratio
ω	Rotational speed
γ_b	Specific heat ratio of burnt region
γ_u	Specific heat ratio of unburnt region
θ_{fuel}	Equivalence ratio
ρ_{cr}	Compression ratio

1. Introduction

Test facilities for internal combustion (IC) engines are vital for the testing and analysis of engines and fuels to be used in real-world applications. Various kinds of equipment are required to correctly capture useful data that can be utilised in the analysis of an internal combustion engine.

This study involved the development and upgrade of an existing spark-ignition (SI) engine test facility in the Mechanical Engineering Faculty of Stellenbosch University, South Africa. This task required a complete overhaul and modernisation of the test cell through the installation of new equipment and an aftermarket engine control unit (ECU).

The ECU is vital for controlling various parameters of an engine during operation. Original equipment manufacturer (OEM) ECUs, however, do not allow for an engine operator to adjust important parameters such as spark-ignition timing or air-fuel ratio. Aftermarket ECUs can allow the operator to investigate the influence of these parameters on combustion.

Spark-ignition engine combustion can be simulated using either a single-zone or a two-zone heat-release model. Commercial software packages such as Lotus Engine Simulation (LES) can also be used to simulate engine performance. The simulation results can then be compared to experimental data to see the viability of using simulation packages to predict engine performance.

The tasks and objectives of this study were:

1. To upgrade and refurbish the existing engine test cell facility by installing new equipment such as a personal computer, programmable logic controller, additional temperature sensors and an air volume flow rate sensor.
2. To test the OEM performance of the internal combustion engine.
3. To install an aftermarket ECU in order to measure the influence of the spark-ignition timing and air-fuel ratio of the engine.
4. To measure the in-cylinder pressure and model the combustion using both a single-zone and a two-zone model.
5. To simulate the engine performance in Lotus Engine Simulation software using derived burn rates.

2. Literature Review

A literature review comprising the various aspects of internal combustion engines and engine testing, including spark-ignition timing systems, fuel metering, combustion, engine management, pressure indicating, analytical heat-release models, engine testing, and Lotus Software Simulation was completed.

2.1 Ignition Systems

SI engines require an ignition point within the cylinder for combustion to start; this is provided by a spark plug. The spark plug ignition timing is an important parameter to control due to its effects on combustion. Modern engine management systems make use of electronic control to adjust the timing, with older engine designs using a mechanical system, such as a distributor. Electronic engine management uses a crankshaft position sensor on the flywheel to measure the position of the pistons and the engine management can also use a camshaft position sensor to determine on which stroke each piston is.

Spark-ignition timing affects the combustion due to controlling when the combustion begins, thus determining the pressure in the cylinder relative to the piston position. Spark-ignition timing that is set too early will have detrimental effects on combustion due to causing engine knock, while timing that is set too late will result in inefficient combustion.

A high voltage is used to create a spark in the air-fuel mixture, heating the mixture up to several thousands of degrees Kelvin. This raises the temperature of the air-fuel mixture to above the auto-ignition temperature, causing the mixture to start burning (Blair, 1999).

2.2 Fuel Metering

Fuel can be introduced in more than one manner in modern engines. Two modern methods used would be via either port fuel injection (PFI) or direct injection (DI). An older, and practically obsolete, method would be carburation, which involves the mixing of atomised fuel with air most commonly using the venturi principle (Probst, 1991). The venturi principle relies on Bernouli's principle, resulting in an increase in the air flow velocity alongside a reduction in pressure. Fuel is introduced via thin channels that draw in the fuel due to a pressure differential (Banapurmath, *et al*, 2010) and atomises it; before mixing the fuel with the moving air.

PFI engines (also referred to as multi-point injection engines) have the fuel injected via electronically controlled injectors into the air-stream prior to the mixture entering the combustion chamber, resulting in a near homogenous air-fuel

mixture, similar to carburation. PFI allows for fine control over the amount of fuel being introduced into the engine. An increase in injection pressure leads to increase turbulence of the fuel spray, therefore resulting in a smaller fuel droplet size (Anand, *et al*, 2009).

Once the air-fuel mixture has entered the combustion chamber, the fuel must vaporise in the air in the combustion chamber for ignition to occur. High temperatures are required to vaporise the fuel (Roby, *et al*, 2014). Thermal heating occurs during the compression stage of the cycle. The heat of vaporisation of the fuel is the amount of energy needed for the fuel to turn from liquid to vapour. The higher the octane number of the fuel, the greater the compression ratio of the cycle can be without engine knock occurring.

The value of the air-to-fuel ratio compared to the ideal stoichiometric air-to-fuel ratio is referred to as the relative air-fuel ratio as seen in equation 1.

$$\lambda = \frac{(A/F)_{actual}}{(A/F)_{\text{stoichiometric}}} \quad\quad\quad (1)$$

The value of the relative air-fuel ratio will vary depending on whether the mixture is rich (<1) or lean (>1) (Heywood, 2018). The equivalence ratio is the inverse of the relative air-fuel ratio, as illustrated in equation 2.

$$\theta_{fuel} = \lambda^{-1} = \frac{(F/A)_{actual}}{(F/A)_{\text{stoichiometric}}} \qu\quad\quad (2)$$

DI engines have electronic injectors placed directly in the combustion chamber. This method allows for fine fuelling control, similar to that of PFI. DI can be classified into two variants where one system uses stoichiometric mixtures for combustion, while the other system uses a mixed mode. This mixed mode uses a stratified mixture with a lean air-fuel ratio at low power conditions and a stoichiometric mixture at high power conditions. The use of a lean combustion brings advantages in terms of fuel economy, pumping losses, and heat transfer. Higher compression ratios may also be used due to the fuel spray evaporating once injected and reducing the charge temperature, further benefiting this method of fuel delivery (Alkidas, 2007).

2.3 Spark-Ignition Combustion

Combustion at the spark plug can only propagate within a certain window of air-fuel ratio. If the air-fuel ratio is too lean, the mixture burnt will not release enough energy to start a chain reaction; if the mixture is too rich then there is not enough oxygen near the combustion to sustain it. Once the combustive mixture is burning, a flame front forms, which burns through the mixture.

Uncontrolled combustion (also referred to as engine knock) occurs when the fuel mixture begins to ignite before the intended time. This can occur when the advancing flame front pressurises and heats the unburnt regions of the air-fuel charge. These regions will then reach auto-ignition conditions and spontaneously combust. The resulting flame front travels in orders of magnitude faster than the conventional flame front, resulting in a rapid increase in temperature and pressure. This causes damage to the physical combustion chamber and can be heard as a distinct high-pitched knocking noise (Blair, 1999).

The causes of knocking can include a high compression ratio, low octane fuel, incorrect spark timing, or too much pressure in the intake manifold from a forced induction system. Excessive turbocharging (or supercharging) results in high temperatures and pressures, which can in turn promote an event referred to as super-knock. This usually occurs at low-speed, high-load conditions where the knock pressure wave magnitude is in an order of magnitude greater than conventional knock (Liu, *et al*, 2017).

This can be alleviated by reducing the inlet manifold pressure or spark timing can be retarded (delayed) to avoid excessive combustion pressures when the piston is near top dead centre (TDC).

The octane number of a fuel indicates the resistance to knock. Therefore, using a high-octane fuel can reduce engine knock. The compression ratio also directly affects the probability of engine knock. Therefore, a correct compression ratio must be determined for the engine's use, fuel, and whether the engine is naturally aspirated or forced induction.

As the power output is directly related to the mass flow rate of air moving through the engine, IC engines can use a forced induction system where an external device is used to force more air into the cylinder. This compressor is usually powered by the engine crankshaft (supercharged) or by using the exhaust gas energy (turbocharged). This can result in high power outputs for physically small engines. This has become commonplace in modern passenger and commercial vehicles.

2.4 Engine Management

Modern engine designs include electronic control of the engine using an ECU. The ECU uses inputs from a variety of sensors to control the spark plug ignition timing and the air-fuel mixture.

Figure 1 shows an engine management system similar to the engine management system used in this study. The ECU uses multiple sensors as inputs to determine the state of the engine and controls the ignition and the fuelling.

The angular position of the crankshaft and camshaft is sent to the ECU for the timing of the spark-ignition and fuel injection. This sensor on the crankshaft is also used to calculate the engine speed. In older designs, a sensor on the throttle body measures the angular rotation caused by the driver (through using a cable to pull the butterfly valve open). Newer engine management systems use an electronic throttle that is opened by an actuator after the ECU receives a signal from the throttle pedal.

The amount of fuel injected into the inlet port or combustion chamber can be controlled through various means. The first method is to use a pre-installed map in the ECU, which uses throttle position, air-mass flow sensor, or intake manifold pressure and engine speed to inject a predetermined amount of fuel based on how long the fuel injectors are held open. The pressure behind the fuel injector is controlled by the fuel pump and pressure regulator (Stone, 2012). There is no feedback using this method, but it is suited to transient engine conditions where the fuelling rate is constantly changing. The second method employed is to use the lambda sensor to provide feedback to adjust the fuelling. This method provides better fuelling control but cannot always respond fast enough to engine load changes and is thus usually employed only in steady state conditions.

The ECU controls the idle actuator to adjust the idle bypass valve. The knock sensor is used to prevent knock conditions by sensing vibrations typical of engine knock. If engine knock is detected, the ECU can either retard ignition timing, enrich the air-fuel mixture, or both.
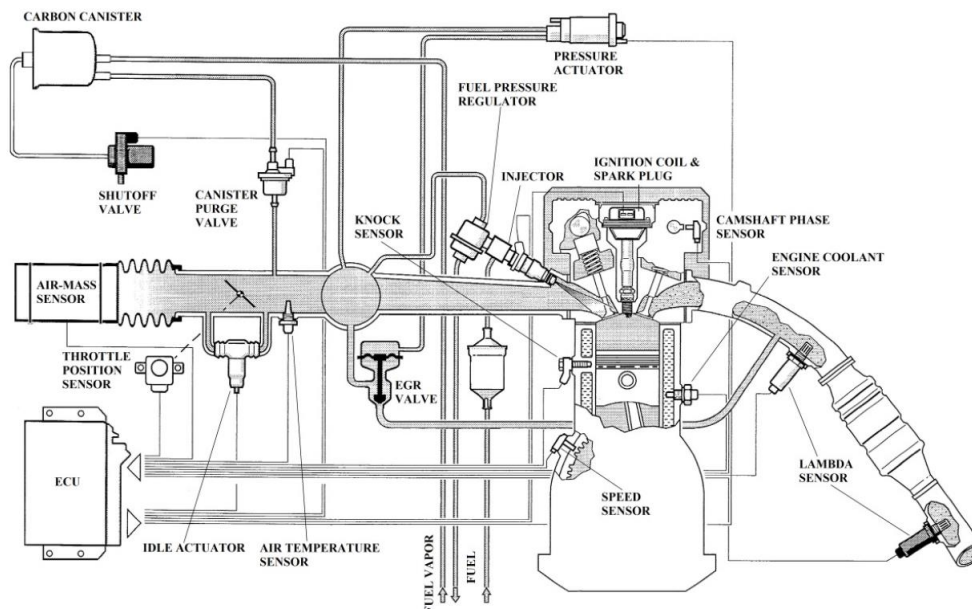
Figure 1: PFI Engine Management System (Bosch, 1995)

2.5 Pressure Indicating

An important pressure measurement that can be made relates to in-cylinder pressure. This, along with a crankshaft angle measurement reference, can provide valuable data on the combustion dynamics occurring within the combustion chamber.

Due to the direct placement of the transducer in the combustion chamber, great care needs to be taken to place the transducer in the best possible location to avoid incorrect measurements.

Regions of the combustion chamber that have high temperature gradients, such as near the injector spray, should be avoided. A position near the intake valve is cooler and has less temperature variation, making it better suited to the placement of the pressure transducer.

Placement of the transducer in the squish gap is relevant if the piston bowl is eccentric. It is also noted that placement on the bowl edge is preferable to placement on the piston edge to avoid gas oscillations. The transducer does, however, undergo more heat flow near the piston bowl compared to near the piston edge. This may result in greater cyclic temperature drift. Installing the transducer recessed into the chamber surface may help with thermal shock effects in both these locations (AVL, 2002).

Installation near the valve is equally possible. The high gas flow rates in these regions, however, must be accounted for; this could cause pressure variations as well as heat flow, which can in turn result in cyclic temperature drifting. The cylinder head temperature can be greatest near the valves. This can cause the transducer to operate in too high a temperature range, affecting the accuracy of measurements (AVL, 2002).

The chosen position must be determined by the borehole needed to mount the pressure transducer. There must be sufficient wall thickness to securely mount the transducer; the borehole cannot penetrate the water or oil galleries.

An alternative method of installation would be to house the sensor in the spark plug. This would greatly simplify installation as the cylinder head does not need to be modified to house the sensor. However, this method could be detrimental if the spark plug location falls within unsuitable regions of the combustion chamber.

Figure 2 shows how the cylinder pressure and mass fraction burnt changes over crankshaft angle during a single spark-ignition event. The mass fraction burnt region lying between 0 - 10% is referred to as the flame development period while the region of 10 - 90% is referred to as the rapid burning period. The slope of the curve is the burn rate and depends greatly on the fuel and engine. (Heywood, 2018).
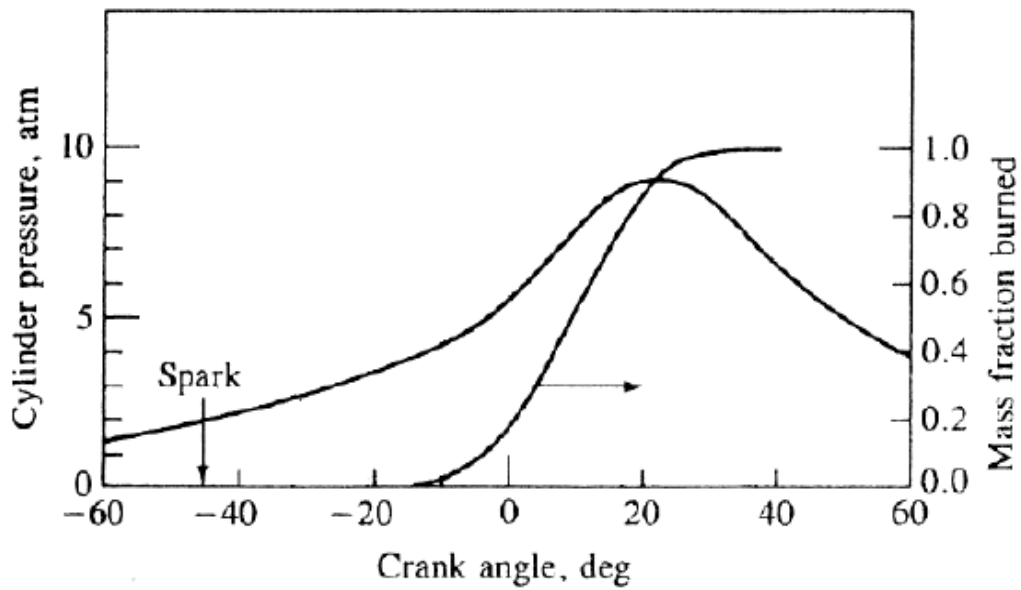
Figure 2: Cylinder Pressure and Mass Fraction Burnt (Heywood, 2018)

2.5.1 Pressure Transducer

Piezoelectric pressure transducers utilise a crystalline material such as quartz (SiO_2) or Gallium Orthophosphate ($GaPO_4$). These materials experience a change in electrical properties when a mechanical load is applied to them. Quartz has a high temperature dependence, meaning the sensor must be water cooled in order to reliably measure pressure. This is important to note as in-cylinder pressure measurement sensors are subject to high temperature ranges (AVL, 2002).

Figure 3 shows an image of a 2010 model spark plug pressure transducer manufactured by Kistler. It allows for pressure measurement without having to modify the engine to mount the sensor. This does, however, expose the sensor to thermal shock. This may adversely affect the in-cylinder pressure signal.

Figure 3: Spark Plug Pressure Transducer (Kistler, 2010)

Gallium Orthophosphate on the other hand shows a piezoelectric sensitivity that is largely independent of temperature, making it ideal for in-cylinder pressure measurement (AVL, 2002).

2.5.2 Shaft Encoder

In order to record in-cylinder pressure relative to the position of the piston, a shaft encoder is required for the pressure indicating. The resolution of the angular position measurement of the crankshaft is an important factor in the quality of the signal.

One type of shaft encoder is an inductive type, which uses a permanent magnet and a coil. When magnetic material moves past a sensor, a voltage is induced. Using a toothed wheel, this voltage signal can be interpreted as measured rotation. Accuracy is limited by the number of teeth on the wheel and can be affected by external interference (AVL, 2002).

A more accurate and reliable method used by shaft encoders is the optical method. A light source is intermittently blocked by a rotating disc with openings in it. A

light sensor detects when the opening passes, generating a voltage pulse which can then be used to detect rotation.

2.5.3 Data Acquisition System

Figure 4 displays a system, constituting various components, used to measure the in-cylinder pressure. A pressure transducer, charge amplifier, shaft encoder, and data acquisition system are required. A charge amplifier is used to convert the raw current signal from the pressure transducer into a voltage signal by providing power. This voltage signal is then recorded. The shaft encoder signal is in the form of pulses produced as the shaft encoder is turned. There are two separate signals: one signal for every complete rotation and another signal for every 0.1° crankshaft angle rotation. The pulse for every rotation is used to signal the data acquisition system that a rotation has been completed. The angular signal every 0.1° is used to trigger the data acquisition system. This trigger will record the immediate voltage signal from the charge amplifier. The data acquisition system requires two signals: a pressure signal and a shaft encoder signal.
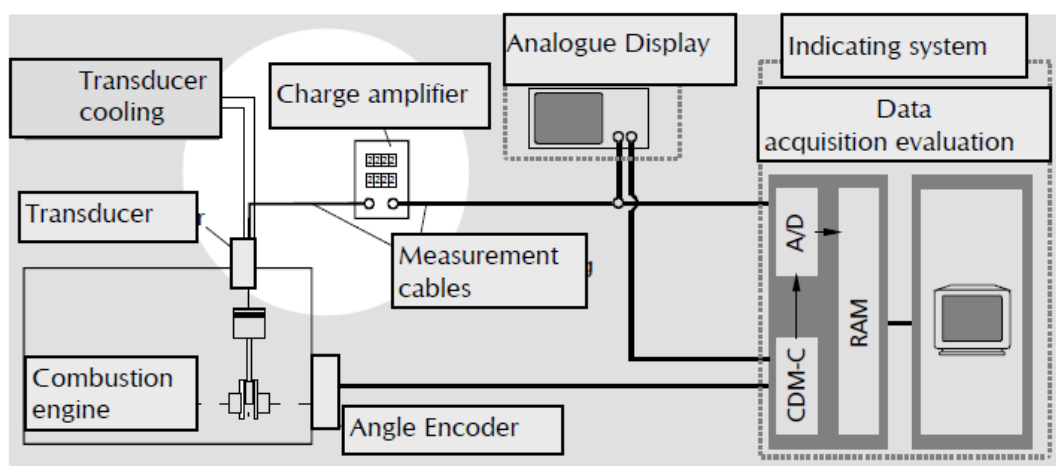
Figure 4: Pressure Indicating Setup (AVL, 2002)

2.5.4 Pegging / Phasing

The data acquisition system can record consecutive pressure cycles. This data can be averaged over a set number of cycles to find a mean pressure trace and to smooth out cycle by cycle variation. Pressure transducer calibration is then used to convert the voltage signal into a pressure signal.

The pressure signal is pegged by using the average manifold pressure value when the inlet valve is about to close. This will reference the gauge pressures measured by the transducer to the absolute pressures needed for the ensuing calculations. Using an optical shaft encoder does not provide a reference for the phase of the pressure trace; an external reference is thus required. This can be done through two methods, as discussed below:

Method A: Log P – Log V

The motored pressure trace is plotted with log P against log V, as seen in Figure 5. A motoring pressure trace is obtained by removing the energy released from combustion. This can be done by disconnecting the fuel injection from one cylinder and running the engine.

If the motoring data is phased correctly, the compression and expansion pressure curve will not cross each other. The gradient of these lines can also be calculated to determine the effective ratio of specific heats γ (Heywood, 2018).
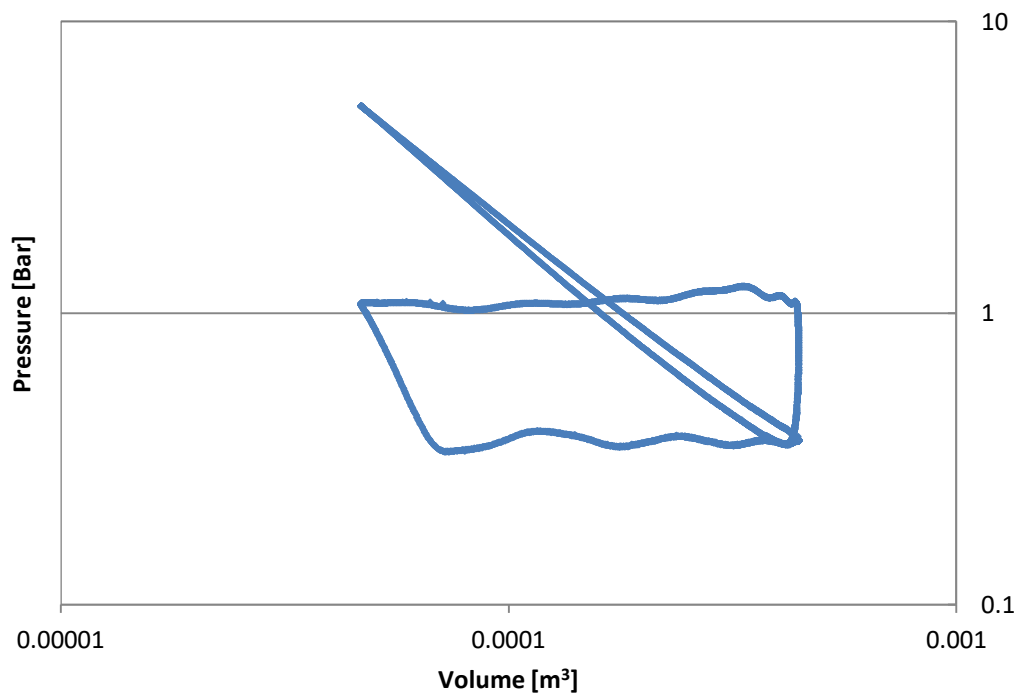
Figure 5: log P – log V of Phased Motoring Pressure Trace at Idle

Method B: Thermodynamic Loss Angle

The motored pressure in a cylinder can be used to determine TDC if no physical reference is available. The pressure trace will not be symmetrical around TDC due to two losses: the mass of gas that leaks out the cylinder and heat lost to the cylinder wall (Beccari & Pipitone, 2009).

Two angular positions are firstly needed defined by the equation:

$$\vartheta_{1,2} = \pm 76.307 \mu^{0.123} \rho_{cr}^{-0.466} \tag{3}$$

The variable μ in equation 3 refers to the rod to crank ratio and ρ_{cr} refers to the compression ratio. The motored pressure trace must then be phased so that the peak pressure coincides with TDC.

Two loss function δF_1 and δF_2 must be calculated at the angular positions ϑ_1 and ϑ_2 using equation 4:

$$\delta F = c_p \frac{\delta V}{V} + c_v \frac{\delta p}{p} \tag{4}$$

where c_p and c_v refers to the specific heat at constant pressure and volume. A mean lost function must then be calculated using:

$$\delta F_m = \frac{\delta F_1 + \delta F_2}{2} \tag{5}$$

The loss function increment can then be calculated by:

$$\delta F_{LPP} = \emptyset \cdot \delta F_m \tag{6}$$

The constant $\emptyset$ can be assumed to be equal to 1.95 (Beccari & Pipitone, 2009).

The loss angle can then be determined by:

$$\vartheta_{loss} = \frac{2}{\rho_{cr}} \cdot \frac{\mu}{\mu+1} \cdot \left[\frac{1}{c_p} \frac{\delta F}{\delta \vartheta} \right]_{LPP} \tag{7}$$

2.6 Heat-Release Models

Analytical models of IC engines can be categorised by the number of individual zones of combustion as well as the dimensionality of the equations used. The simplest model is the single-zone zero-dimensional model, implemented in this

study. A two-zone zero-dimensional model was also used for this study as a means of comparison.

2.6.1 Single-Zone Heat-Release Model

Single-zone models assume that the conditions in the cylinder are uniform in terms of pressure, temperature, and composition. These models additionally assume that there is no variation in the working fluid through any spatial dimensions and that the combustion is a heat addition process (Ramos, 1989).

The volume of the combustion chamber as a function of the crankshaft angle can be expressed as:

$$V = V_c \times \left[1 + \tfrac{1}{2}(r_c - 1)[R + 1 - cos\theta - (R^2 - sin^2\theta)^{1/2}\right] \qquad (8)$$

Where V_c is the clearance volume, r_c is the compression ratio, R is the ratio between the connecting rod length and crank radius, and θ is the crankshaft angle (Heywood, 2018).

The first law of thermodynamics for a closed system is:

$$\delta Q_R - \delta Q_L = mc_v\delta T + \delta W \qquad (9)$$

where Q_R is the heat released from combustion, Q_L is the heat lost to the cylinder block and piston head and W is the work done by the gas on the piston. The other variables are the mass (m), specific heat (c_v), and the temperature (T). (Blair, 1999)

Equation 9 does not account for gasses that move into crevices (the space above the piston ring between the cylinder walls and piston sides) and thus do not work on the piston. A term can be added to equation 9 in the form of:

$$(h - e)\delta m_{CR} \qquad (10)$$

where h is the enthalpy of the mass flowing into the crevice, e is the internal energy of the mass of gas in the combustion chamber, and m_{CR} is the mass of gas in the crevices. The change of the mass in the crevice can be written as:

$$\delta m_{CR} = V_{CR}\frac{\delta p}{RT_{wall}} \qquad (11)$$

where V_{CR} is the volume of the crevice, R is the specific gas constant p is the combustion chamber pressure, and T_{wall} is the wall temperature (Ramos, 1989). The final equation to be used is derived by dividing equation 9 and 10 by a crankshaft angle differential:

$$\frac{dQ_R}{d\theta} = mC_v\frac{dT}{d\theta} + p\frac{dV}{d\theta} + \frac{dQ_L}{d\theta} + (h - e)\frac{dm_{CR}}{d\theta} \qquad (12)$$

The ideal gas law can be used to obtain an equation for the temperature differential. It assumes that the gas constant value is constant:

$$dT = \frac{pdV}{mR} + \frac{Vdp}{mR} - \frac{pVdm}{m^2R} \qquad (13)$$

$$dT = \frac{Tdp}{p} + \frac{TdT}{V} - \frac{dm}{m} \qquad (14)$$

Equation 14 can be put into equation 12 to obtain:

$$\frac{dQ_R}{d\theta} = \frac{c_v Vdp}{Rd\theta} + \left(\frac{c_v}{R} + 1\right)p\frac{dV}{d\theta} + \frac{dQ_L}{d\theta} + (h - e + c_v T)\frac{dm_{CR}}{d\theta} \qquad (15)$$

To determine the specific heat ratio $\gamma = (\frac{c_p}{c_p - R})$, an equation for γ as a function of in-cylinder temperature must be used: This will account for variations in temperature as well as the composition of the working fluid.

$$\gamma = a + b.T + c.T^2 \qquad (16)$$

$a = 1.338$

$b = -6 \times 10^{-5}$

$c = 1 \times 10^{-8}$

Equation 16 can be used to determine the specific heat of air (Brunt et al., 1998)

If we define $\gamma = (1 + \frac{R}{c_v})$ then equation 15 becomes:

$$\frac{dQ_R}{d\theta} = \frac{Vdp}{(\gamma - 1)d\theta} + \frac{\gamma pdV}{(\gamma - 1)d\theta} + \frac{dQ_L}{d\theta} + (h - e + C_v T)\frac{dm_{CR}}{d\theta} \qquad (17)$$

The crevice volume is very small relative to the volume of the piston and is not critical to the energy balance; the crevice work term can be dropped without reducing the model accuracy in any significant way (Ramos, 1989).

2.6.2 Two-Zone Heat-Release Model

The abovementioned single-zone model does not account for regions in the combustion chamber having different thermodynamic properties or different temperatures. As combustion occurs, a burnt region expands while an original unburnt region reduces in size. This effect on combustion can be accounted for

using a two-zone heat-release model. This model is also zero-dimensional and does not allow for variation in the spatial dimensions.

Figure 6 shows the two regions assumed in this model. On the left the unburnt region is shown while the burnt region is shown on the right. $\dot{Q}$ and $\dot{W}$ refer to the heat lost from the control volume and the work done by the contents in the cylinder.
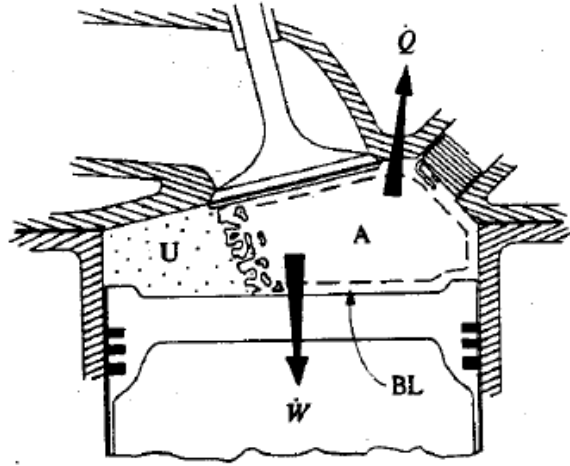
Figure 6: Two-Zone Heat-Release Model (Heywood, 2018)

Applying the conservation of mass:

$$\frac{V}{m} = \int_0^{x_b} v_b dx + \int_{x_b}^1 v_u dx \tag{18}$$

and the conservation of energy:

$$\frac{U_0 - W - Q}{m} = \int_0^{x_b} u_b dx + \int_{x_b}^1 u_u dx \tag{19}$$

where V is the volume of the cylinder, m is the mass of the cylinder contents, x_b is the mass fraction burnt, U_0 is the internal energy at some reference point θ_0, u is the specific internal energy, Q is the heat lost, and W is the work done:

$$W = \int_{V_0}^V p dV \tag{20}$$

$$Q = \int_{\theta_0}^\theta \left(\frac{\dot{Q}}{360N} \right) d\theta \tag{21}$$

14

$\dot{Q}$ refers to the rate of heat lost.

The two separate regions must be defined in terms of thermodynamics properties.

$$pv_b = R_b T_b \tag{22}$$

$$pv_u = R_u T_u \tag{23}$$

$$u_b = c_{v,b} T_b + h_{f,b} \tag{24}$$

$$u_u = c_{v,u} T_u + h_{f,u} \tag{25}$$

where h_f refer to the enthalpy of formation, T the temperature, R the specific gas constant, u the internal energy, c the specific heat and v the specific volume of the burnt and unburnt region.

Combining equations 18 to 25 leads to:

$$\frac{pV}{m} = x_b R_b \bar{T}_b + (1 - x_b) R_u \bar{T}_u \tag{26}$$

$$\frac{U_0 - W - Q}{m} = x_b \left(c_{v,b} \bar{T}_b + h_{f,b} \right) + (1 - x_b)(C_{v,u} \bar{T}_u + h_{f,u}) \tag{27}$$

where:

$$\bar{T}_b = \frac{1}{x_b} \int_0^{x_b} T_b dx \tag{28}$$

$$\bar{T}_u = \frac{1}{1 - x_b} \int_{x_b}^1 T_u dx \tag{29}$$

refer to the mean temperatures.

Equation 26 and 27 can be solved to obtain:

$$x_b = \frac{pV - p_0 V_0 + (\gamma_b - 1)(W + Q) + (\gamma_b - \gamma_u) m c_{v,u}(\bar{T}_u - T_0)}{m[(\gamma_b - 1)(h_{f,u} - h_{f,b}) + (\gamma_b - \gamma_u)c_{v,u}\bar{T}_u]} \tag{30}$$

and:

$$\bar{T}_b = \frac{R_u}{R_b} \bar{T}_u + \frac{pV - mR_u \bar{T}_u}{mR_b x_b} \tag{31}$$

If we assume that the unburnt gas is initially uniform and undergoes isentropic compression, then:

15

$$\frac{\bar{T}_u}{T_o} = \left(\frac{p}{p_0}\right)^{\frac{(\gamma_u - 1)}{\gamma_u}} \tag{32}$$

Equation 32 can be used to determine the unburnt region temperature while equation 30 can be used to determine the mass fraction burnt. In a fully mixed model, $T_b = \bar{T}_b$. The thermodynamic properties of the burnt region were determined using Heywood (2018).

This assumption ignores the effect of a temperature gradient within the burnt region as sections that burn earlier undergo compression after combustion, while sections that burnt later undergo compression before combustion. This results in different sections ending up at different temperatures at the end of the combustion process (Heywood, 2018).

2.6.3 Heat Transfer

The heat transfer term can be employed through various models such as the Annand, Woschni, or Eichelberg heat transfer models. The Eichelberg heat transfer model is traditionally used for diesel combustion. The coefficients used for the heat transfer models were those by Lotus Engine Simulation (Lotus Engine Software [*sa*]).

Annand Heat Transfer Model

The heat transfer coefficient is calculated as follows:

$$h_{ht} = \frac{A_A \, k \, Re^{B_A}}{D_{cyl}} \tag{33}$$

where h_{ht} is the heat transfer coefficient, A_A is the Annand open or closed cycle coefficient, B_A is the Annand open or closed cycle coefficient, k is the thermal conductivity of the gas, D_{cyl} is the cylinder bore, and Re is the Reynolds number based upon the mean piston speed, cylinder bore, and gas density (Annand, 1963).

The total heat transfer is calculated by:

$$Q_L = A \, h_{ht} \left(T_{gas} - T_{wall}\right) + A \, C_A \left(T_{gas}^{\,4} - T_{wall}^{\,4}\right) \tag{34}$$

where C_A is the Annand closed cycle coefficient and A is the chamber surface area. T_{gas} and T_{wall} are the temperatures of the gas and wall respectively.

The T_{gas} variable is calculated by:

$$T_{gas} = \frac{p}{p_{ivc}} \frac{V}{V_{ivc}} T_{ivc} \tag{35}$$

where p_{ivc}, V_{ivc}, and T_{ivc} are the pressure, volume, and temperature at inlet valve closing (Beccari & Pipitone, 2009).

The values for the coefficients are shown in Table 1.

Table 1: Coefficients for Annand Heat Transfer

Combustion System	Open Cycle		Closed Cycle		
	A_A	B_A	A_A	B_A	C_A
Carburetted or Port injected	0.2	0.8	0.12	0.8	$4.29*10^{-9}$
Direct or Indirect Injection	1.1	0.7	0.45	0.7	$3.271*10^{-8}$

Woschni Heat Transfer Model

The convective heat transfer coefficient can be calculated by:

$$h_{ht} = \frac{A_W \, p^{0.8}}{T^{0.55} \, D_{cyl}^{0.2}} \left(B_W \, \bar{U}_{piston} + C_W \, \bar{U}_{swirl} + D_W \, \frac{T_{soc} \, V \, (p - p_{motor})}{p_{soc} * V_{soc}} \right)^{0.8} \quad (36)$$

where:

h_{ht} = heat transfer coefficient

A_W = Woschni open or close cycle A coefficient

B_W = Woschni open or close cycle B coefficient

C_W = Woschni open or close cycle C coefficient

D_W = Woschni closed cycle D coefficient

p = Cylinder pressure

T = Cylinder temperature

V = Cylinder volume

$\bar{U}_{swirl}$ = Mean swirl velocity

T_{soc} = Cylinder gas temperature at start of combustion

p_{soc} = Cylinder gas pressure at start of combustion

V_{soc} = Cylinder volume at start of combustion

p_{motor} = Motoring cylinder pressure

The mean piston speed is calculated by:

$$\overline{U}_{piston} = \frac{2\,N\,stroke}{60} \tag{37}$$

The mean swirl velocity can be calculated by:

$$\overline{U}_{swirl} = \frac{N\,\pi\,D_{cyl}\,S_{rat}}{30} \tag{38}$$

where S_{rat} is the Wochni open or closed cycle swirl ratio.

The motoring cylinder pressure is given by:

$$p_{motor} = p_{soc}\left(\frac{V_{soc}}{V_{cyl}}\right)^{G} \tag{39}$$

where G is the Woschni ratio of specific heats and V_{cyl} is the maximum volume of the cylinder (Sihling & Woschni, 1979).

The heat transfer from the cylinder is:

$$Q_L = A\,h_{ht}\,(T_{gas} - T_{wall}) \tag{40}$$

The open cycle coefficients are shown in Table 2.

Table 2: Coefficients for Woschni Heat Transfer

Combustion system	Open cycle			
	A_W	B_W	C_W	S_{rat}
Carburetted or Port injected	3.3	9.12	0.834	0
Direct or Indirect Injection	3.3	6.18	0.417	0

Combustion system	Closed Cycle					
	A_W	B_W	C_W	D_W	G	S_{rat}
Carburetted or Port injected	3.3	4.56	0.616	0.00324	1.33	0
Direct or Indirect Injection	3.3	2.28	0.308	0.00324	1.33	0

Eichelberg Heat Transfer Model

The heat transfer coefficient is given by:

$$h_{ht} = A_E\,\overline{U}_{piston}^{\;0.33}\,(p\,T)^{B_E} \tag{41}$$

where

A_E = Eichelberg open or close cycle A coefficient

B_E = Eichelberg open or close cycle B coefficient (Eichelberg, 1939)

The heat loss from the cylinder is:

$$Q_L = A\, h_{ht}\, (T_{gas} - T_{wall}) \tag{42}$$

The open cycle coefficients are shown in Table 3:

Table 3: Coefficients for Eichelberg Heat Transfer

Combustion System	Open/Closed Cycle	
	A_E	B_E
All Combustion system Types	2.43	0.5

Figure 7 shows a comparison of the heat transfer coefficients over a compression and expansion stroke. The Annand heat transfer model predicts the highest heat loss over the entire compression and expansion stroke. Woschni and Eichelberg follow one another on the compression stroke. However, Woschni has a higher peak heat transfer coefficient. During the expansion stroke, Eichelberg predicts higher heat loss as compared to Woschni.

The study will use the Woschni heat transfer model due to the convective heat loss modelled. For spark-ignition combustion, radiation may account for up to 20% of the heat transfer which is lower than that of compression-ignition combustion. The Woschni heat loss model takes into account the convective loss due to piston motion as well as due to combustion. (Stone, 2012).
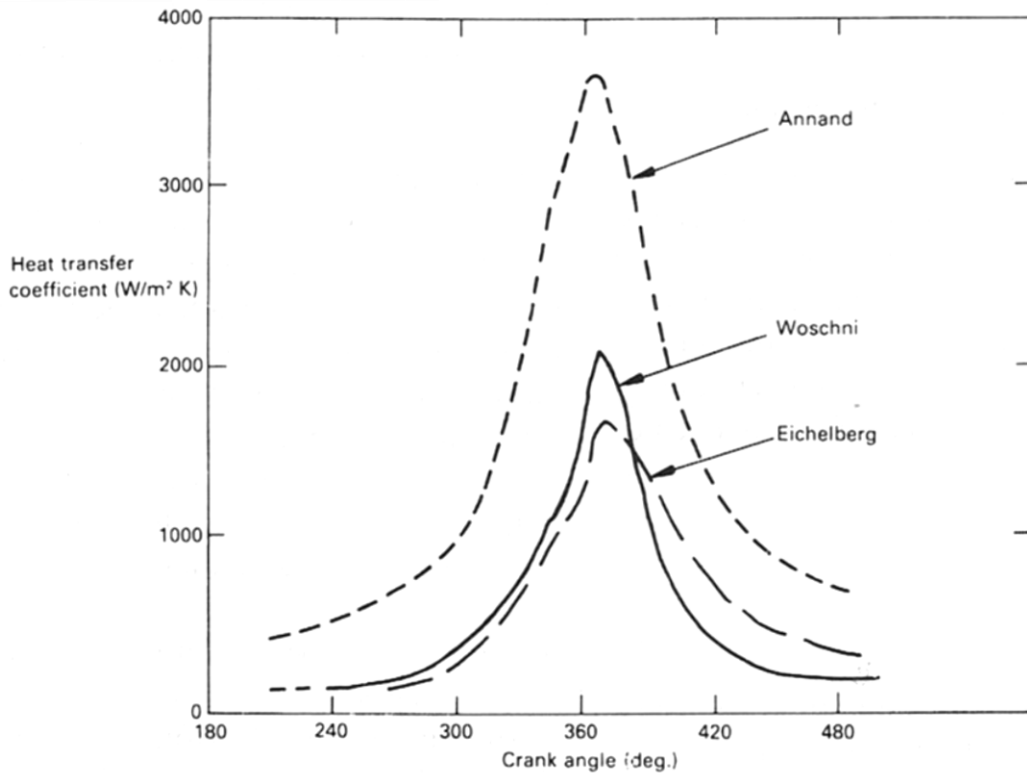
Figure 7: Comparison of Heat Transfer Coefficients for Different Heat Transfer Models (Stone, 2012)

2.6.4 Wiebe Function

The heat-release within an engine can be estimated using a function of mass fraction burnt:

$$x(\theta) = 1 - e^{-a[\frac{\theta - \theta_0}{\Delta\theta_b}]^{m+1}} \tag{43}$$

where $x(\theta)$ is the mass fraction burnt at crankshaft angle θ, θ_b is the crankshaft angle at the start of combustion and $\Delta\theta_b$ is the duration of combustion, usually $a = 5$ and $m = 2$ (Stone, 2012).

2.7 Engine Testing

An engine test facility requires a wide range of equipment related to various engineering fields. This is due to the increased focus on electronic control of the IC engines. This integration in electronics results in test facilities containing vast amount of electrical equipment to control the engine. The engine test facility, safety, dynamotor and measurement equipment will be discussed in this section.

20

2.7.1 Test Facility Infrastructure and Safety

An engine test facility is a test cell where an IC engine can be connected to a dynamometer and tests can be run on the engine while various sensors record a multitude of relevant data. This equipment can include the engine, driveshaft, dynamometer, fuel delivery system, pressure sensors, temperature sensors, throttle controller, dynamometer controller, and programmable logic controller.

The engine must be mounted onto a frame that can safely support the weight of the engine as well as allow space for adjustment if necessary. Furthermore, vibration isolation is important to reduce noise and mechanical wear on structural components.

Other important considerations for the test cell include ventilation, sound isolation, a fire suppression system, a water-cooling system, and a control room adjacent to the test cell.

The correct software must also be used so that accurate and predictable control over the test cell can be exercised. The appropriate software is also needed to record the data that the measurement devices feed back to the engine tester.

Engine exhaust contains carbon monoxide, which may lead to asphyxiation when inhaled. This, together with the introduction of a flammable liquid, can impose various dangers on engine testers. Exhaust evacuation systems and fire extinguishing systems are compulsory for a test facility to function safely. A strict testing procedure is also needed to ensure all engine and testing components are operating as designed. Regular checks on equipment are therefore necessary to ensure overall safety measures are adhered to.

2.7.2 Dynamometer

To simulate a load on the test engine, a dynamometer must be coupled to the engine to absorb the energy output. In order to measure rotating torque, the dynamometer consists of a rotor and stator. The rotor is fixed to the engine crankshaft via a drive shaft and spins at the same speed as the crankshaft. The stator is mounted on bearings that are co-axial to the rotor and does not provide resistance to the rotor torque. The stator is fixed to the dynamometer mount via the load cell.

Through braking action, the stator applies a force to the rotor. The reaction force on the stator is applied through the load cell to the dynamometer mount.

Hydraulic dynamometers provide the braking action through the rotor transferring energy to the stator via the water. The energy being absorbed by the dynamometer

is in the form of turbulence and friction. This will cause the water temperature to rise. The load can vary by changing the water level within the dynamometer.

An electrical dynamometer can be used to absorb the energy from the engine and create electricity. This is the simple generator principle of an electric motor. Both direct current and alternating current motors can be used; transient tests can be performed using electronic control systems. The dynamometers can be water-cooled or air-cooled. The dynamometer can be used to supply energy as well as drive the engine setup at set speeds. This is useful for doing friction tests on IC engines.

An alternative electrical dynamometer that can be used is an eddy current dynamometer. The coil of this dynamometer creates a magnetic field that intersects the rotor parallel to the axis of rotation. The spinning rotor cuts these magnetic field lines perpendicularly causing eddy currents to form in the loss plates. These eddy currents interact with the excitation coil magnetic field, creating a force in the opposite direction of the rotor to act upon the rotor. This is the braking torque that the engine will feel. The magnitude of this force is controlled by changing the excitation coil current.

The energy being absorbed by the dynamometer manifests in the form of heat energy in the loss plates. These plates have channels cut into them for water to pass through and remove the heat (Gitano, [*sa*]).

An eddy current dynamometer was chosen for this study due to the reliability and control provided by the dynamometer. It can provide stable steady state engine braking with a simple design that can be controlled easily using the control equipment within the test cell.

2.7.3 Engine Power

One of the most important engine outputs to measure is the torque produced by the IC engine. This measurement is needed to determine the power output of the engine.

The torque is usually measured using a load cell that is connected to an arm that is a known distance from the centre of rotation for the dynamometer with the load cell line up tangentially to the driven dynamometer axis.

$$T_{torque} = F \cdot D \tag{44}$$

Equation 44 shows how the torque is calculated where F is the force experienced by the load cell, D is the distance the load cell is located from the dynamometer axis, and T_{torque} is the engine torque.

Engine speed is a vital measurement to obtain as it is needed for a power output calculation. It also plays a role in other calculations as engine speed affects many control aspects including spark timing.

The speed of the engine and the dynamometer are identical as they are directly coupled. The dynamometer shaft extends out the rear of the dynamometer and a toothed wheel is attached to it. Located close to the teeth of the wheel is a hall sensor that produces a voltage spike as each tooth passes near the sensor. Using the number of teeth on the wheel, the engine speed can be calculated with the voltage signal produced. This signal is usually sent to the dynamometer controller, which can feed it back to the PLC and control computer.

The ECU can also receive its own speed measurement, which it obtains by using an inductive speed sensor on a toothed flywheel. The sensor contains a soft iron core that is enclosed by windings. The toothed flywheel changes the level of magnetic flux through the coil inducing a sinusoidal voltage output. A gap in the tooth wheel indicates a full revolution of the crankshaft (Robert Bosch GmbH (Ed.), 2007).

Depending on what the speed sensor output is, a conversion from revolutions per minute to radians per second may be necessary.

$$\omega = N \frac{2\pi}{60} \qquad \qquad (45)$$

The engine speed is denoted by ω in rad/s and N in rpm (revolutions per minute). The brake power from the engine can then be calculated using:

$$P_b = T_{torque} \cdot \omega \qquad \qquad (46)$$

The power that was recorded during testing was corrected using the ECE R49:2008 standard. This allows the recorded data to be compared to other test data recorded in different testing conditions.

2.7.4 Fuel Mass Flow Rate

In order to make accurate efficiency calculations, accurate fuel mass flow rates must be measured. A parameter often used in engine analysis is brake specific fuel consumption.

Fuel flow rate can be measured using a cumulative method. This involves measuring the time taken to use a known mass or volume of fuel. This gives the average fuel rate over the measurement time. A more accurate fuel rate measurement method would be an instantaneous fuel flow measurement. This can be done by measuring the change in mass of a vessel of fuel over time. The rate of

change in the mass would equate to the mass flow rate. The Coriolis Effect flow meter can also be used as an instantaneous fuel flow measurement device.

The method of instantaneous flow measurement provides the most detailed measurement and was therefore used in this study. An AVL 7130-06 gravimetric flow meter, measuring the mass of fuel flowing to the engine, provided the fuel flow measurement needed for this study

2.7.5 Air Mass Flow Rate

The air mass flow rate can be measured using an orifice plate. A large box is connected via a pipe to the engine intake and the orifice plate is attached to the box. The large box is used to dampen variations in the air flow. The pressure drop is measured across the orifice plate and the air mass flow rate can be calculated. This method is disadvantageous as it requires a large box that uses space in a test cell as well as requiring a restriction in the flow, which can in turn have adverse effects on the performance of the engine.

The air mass flow rate can also be measured using the principle of the Hagen-Poiseuille equation. A laminar flow section of pipe causes a pressure drop that is dependent on the volumetric flow rate of the fluid. This device can be connected to the intake of the engine once calibrated and the pressure drop measured across it can be used to calculate the mass flow rate after the air density is accounted for. The pressure drop across the flow element is very small relative to the variation in manifold pressure therefore the effect on performance is negligible.

2.7.6 Lambda Sensor

The lambda sensor measures the amount of oxygen in the exhaust and compares it to the ambient oxygen level. It determines whether the ratio of the incoming air-fuel mixture is lean, rich, or stoichiometric. Two sensor surfaces are coated with zirconium dioxide ($ZrO2$) electrolyte and porous platinum, respectively. A voltage that is dependent on the oxygen-ion flow rate is then sent back to the ECU (Ferguson & Kirkpatrick, 2001).

Modern third-party lambda sensors can be used to independently measure the air-fuel ratio of the engine during operation. These units are connected to their own sensor that is mounted in the appropriate place in the exhaust system. The units are self-calibrating once turned on and they can then give the operator more accurate readings to compare to OEM or aftermarket ECU readings.

2.7.7 Temperatures and Pressures

Temperature measurement is a crucial tool in the analysis of IC engines. It is used for data collection, for example, inlet manifold temperatures, exhaust temperatures, as well as for safety management, as seen in coolant water temperatures.

Commonly used temperature measurement devices are based on electrical resistance or thermoelectric effects. A resistor temperature detector (RTD) uses the change in resistance to detect the change in temperature. Platinum is the most common material used in RTDs. A certainty in temperature measurement as low as ±0.005 °C allows for high accuracy in measurements (Figliola & Beasley, 2011).

Thermistors are thermally sensitive resistors made from ceramic materials. Their resistances change with temperatures similar to that of RTDs but an increase in temperature yields a rapid decrease in resistance. They are useful for rugged usage with fast response times.

The most commonly used temperature measurement device used is the thermocouple. It uses the Seebeck Effect to generate an electromotive force (EMF) in an open thermocouple circuit. When two circuit junctions are at different temperatures with two different materials at each junction, an EMF is created, which can be measured (Figliola & Beasley, 2011).

J-type and K-type thermocouples are often used in engine testing. J-type thermocouples use iron and constantan copper-nickel metals and have a measurement range between -210 – 1200 °C. K-type thermocouples use nickel-chromium and nickel-aluminium metals with a temperature range between -270 - 1372 °C (ANSI and IEC Colour Codes).

Pressure measurement is useful for engine analysis alongside ensuring safe engine operation. Fuel pressure measurement is required to confirm that the fuel pump is operational and that an appropriate amount of pressure is behind the fuel injectors. Oil pressure measurement is also needed to confirm that the oil distribution system is operating correctly. These pressure measurements do not contribute to engine performance directly but help the operator in knowing that the engine is functioning within the designed limits.

Inlet manifold pressure is an equally important measurement as it is used for the referencing of the in-cylinder pressure trace. It also provides useful data to calibrate aftermarket ECU that require manifold pressure for engine mapping.

Fuel and oil pressure measurements require a sensor that is cable of measurements above atmospheric pressure while inlet manifold pressure requires a vacuum

sensor due to the vacuum created in the inlet manifold by a throttled spark-ignition internal combustion engine.

2.8 Engine Operating Parameters

The recorded engine data can be used to calculate the various engine parameters used to analyse the performance of the engine.

2.8.1 Mean Effective Pressure

Indicated Mean Effective Pressure

Using a pressure trace where the pressure in the cylinder can be plotted versus crankshaft angle, the IMEP can be calculated as:

$$IMEP = \frac{\int p dV}{V_d} \tag{47}$$

Brake Mean Effective Pressure

The brake mean effective pressure (BMEP) is a measure of the work done by the engine over a 4-stroke cycle divided by the displaced volume. It can be described as:

$$BMEP = \frac{T_{torque}\, n_c\, 2\pi}{V_d} \tag{48}$$

where n_c is equal to 2 (for a 4-stroke cycle) and V_d is the displaced volume of the cylinder. The numerator equates to energy as it is the torque multiplied by the 2 revolutions of angular distance. Since for all 4-stroke engines the $n_c*2\pi$ term is the constant, the BMEP can be interpreted as proportional to the torque per displacement volume of an engine when comparing amongst 4 stroke engines.

Friction Mean Effective Pressure

The friction mean effective pressure (*FMEP*) can be calculated by:

$$FMEP = IMEP_{gross} - BMEP \tag{49}$$

where $IMEP_{gross}$ is the pressure work delivered to the piston during only the compression and expansion stokes.

2.8.2 Specific Fuel Consumption

The brake specific fuel consumption of an engine is given by

$$BSFC = \frac{\dot{m}_f}{P_b} = \frac{1}{n_{bt}\,Q_{net}} \tag{50}$$

where $\dot{m}_f$ is the mass flow rate of fuel, P_b is the engine power output, n_{bt} is the brake thermal efficiency, and Q_{net} is the lower calorific heating value of the fuel.

Mechanical efficiency can be calculated by:

$$n_m = \frac{BMEP}{IMEP} \tag{51}$$

2.8.3 Coefficient of Variation for IMEP

The cycle by cycle variation of combustion can be quantified through using the coefficient of variation (COV) for IMEP. The recorded consecutive in-cylinder pressure cycles are processed to determine the IMEP$_{net}$ for each individual cycle. This data is then used in equation 52 to calculate the cycle by cycle variability of the combustion:

$$COV_{imep}(\%) = \frac{\sigma_{imep}}{imep_{ave}} \times 100 \tag{52}$$

In the above equation, σ_{imep} is the standard deviation of the IMEP data while $imep_{ave}$ is the average IMEP of the data. A value of between 2 - 5% is deemed drivable (Heywood, 2018).

2.9 Lotus Engine Simulation

Lotus Engine Simulation (LES) is a versatile, easy-to-use software package that can be used to simulate the performance of two stroke or four stroke engine using various types of fuels. Naturally aspirated or forced induction can also be implemented.

Parameters such as pressure, temperature, air and fuel mass flow rates, heat transfer coefficients, and various other measurements can be tracked and recorded for analysis. These can be recorded anywhere along the air flow path or from any of the cylinders. LES uses a one-dimensional pipe flow model to account for the air flow through the engine piping. It utilises a zero-dimensional, single-zone heat-release model for the combustion chamber (Lotus Engine Software [*sa*]). The energy balance equation is as follows:

$$\frac{\partial Q}{\partial t} + \frac{\partial B}{\partial t} + \frac{\partial W}{\partial t} = \frac{\partial E}{\partial t} + \sum \delta H \tag{53}$$

where B is the heat-release through combustion, H the enthalpy, Q the heat transfer, W the work done, and E the internal energy.

Inputs for the software include variables such as air-fuel ratio, engine speed, throttle position, heat-release (Wiebe function), air temperature, barometric pressure, humidity, friction, amongst other settings used for the simulation parameters (for example, the number of simulation cycles).

The software can output numerous performance parameters such as torque, net and gross IMEP, FMEP, and power. The program also calculates the air mass flow rates, volumetric efficiency, fuel mass per cycles, mechanical and thermal efficiencies, and cylinder heat loss.

Emissions can also be calculated. The software also has tools that can calculate friction estimates and do heat-release analyses. Models are built by arranging components together on a 2-dimensional plane and connecting them to one another. Components include each cylinder, the valves, ports, and pipes. The simulation can be run as the components are set.

There is an additional load finder function that allows the user to specify a desired power, torque or BMEP output, alongside a function to indicate what parameters (for example, the throttle butterfly valve angle) can be altered to reach these specific outputs.

The software will progress through a specified number of cycles or until a mass convergence has been reached. The final results can then be saved from a specified cycle (usually the last cycle as this will have come closest to a mass convergence).

3. Test Facility Setup

Modern testing of internal combustion engines is done mostly on fixed test benches where the engine is operated under controlled conditions. Engine parameters are closely monitored while engine performance is recorded using data received from the attached dynamometer and other sensors.

3.1 Test Facility Layout

Figure 8 shows the general layout of the test facility as worked on in this study. Compared to the previous student (Kenny, 2013), an altered setup, with the addition of an air volumetric flow sensor element, additional thermocouples, and an aftermarket ECU was used. The existing test cell contained the test engine, test bench, eddy current dynamometer, fuel flow meter cooling systems, exhaust extraction system, and control electronics.
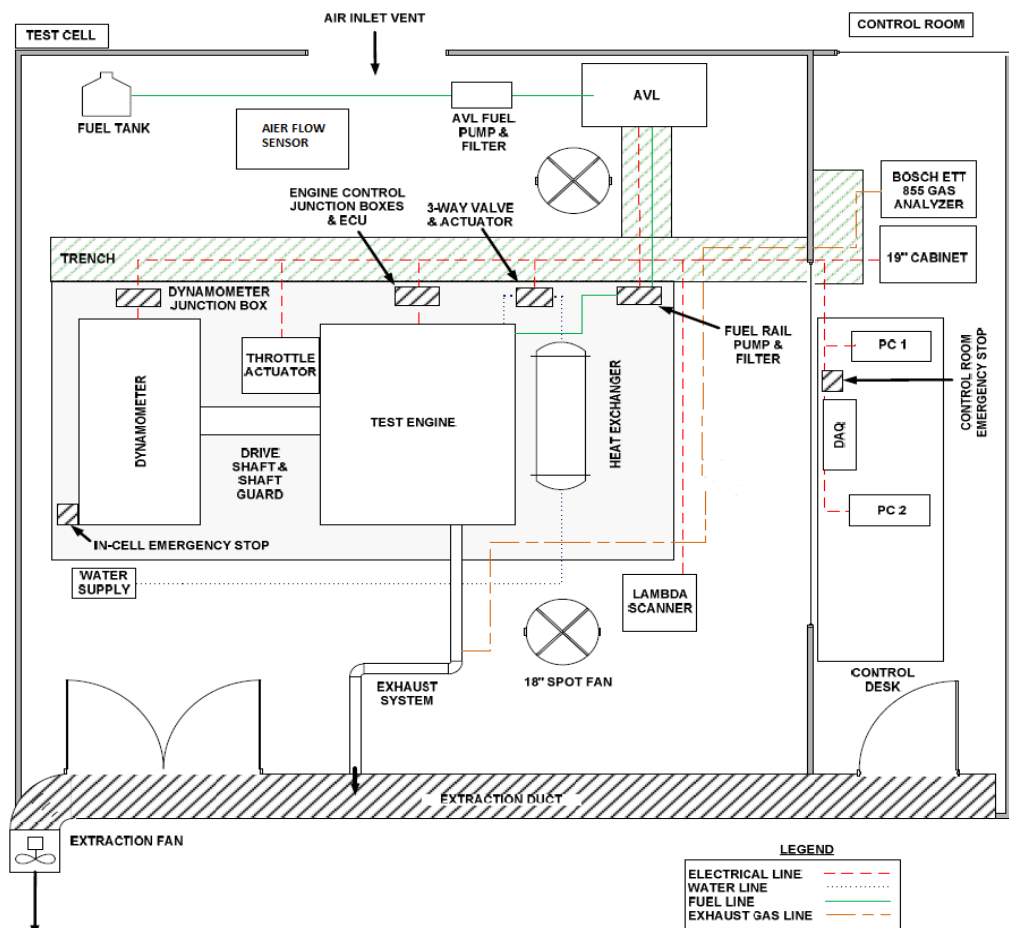

Figure 8: Test Facility Layout (After Kenny, 2013)

3.2 Test Cell Equipment

The test facility contains a ladder frame test bed, an internal combustion engine to be tested, a dynamometer, sensors and actuators, equipment to control the engine, exhaust extraction devices, as well as the required software (Kenny, 2013).

3.2.1 Spark-Ignition Engine

The internal combustion engine used was a 4-cylinder electronic fuel injected spark-ignition engine. It was a four-stroke engine with a displacement of 1.6 ℓ and was port fuel injected. It was mounted onto a ladder frame test bed using rubber engine mounts to dampen the engine vibrations. The engine was also mounted at a slight angle along the crankshaft axis, in accordance to typical engine bay installation for effective oil flow.

The plastic engine intake manifold was bolted to the intake side of the cylinder head to allow for air to flow into the intake ports. A cable-actuated throttle body was connected to the intake to control the amount of air flowing into the engine. Plastic piping was used to connect the air filter to the throttle body while a laminar flow measurement device was connected to the intake of the air filter.

A cast iron exhaust manifold was used to direct the exhaust gas through an exhaust system that was connected to an extraction system. This would draw the exhaust gas through ventilation channels, to be released outside of the building.

An OEM engine control unit was initially installed onto the engine. The engine underwent a service to ensure that it was safe to operate due to the long period of time that the engine had been left unused. A borescope inspection of the piston tops, cylinder heads, valve stems and seats, and the cylinder lining revealed no issues. An oil change was also performed.

See Appendix A-1 for more information about the test engine.

3.2.2 Instrumentation and Equipment

An empty cabinet was filled with modules for the test cell. A *Shinko* temperature controller, *Allen-Bradley MicroLogix 1200* Programmable Logic Controller, an AVL 7030 balance control module, a *Schenck LEW 2000* dynamometer controller, LES 2000 dynamometer power supply, and a throttle control actuator controller were installed.

Trunking and connector blocks were also installed to assist in the cable management within the 19 inch cabinet.

Shinko Coolant Temperature Controller

A *Shinko* temperature controller was used alongside a water-to-water heat exchanger to control the engine coolant temperature. A three-way mixing valve was used to regulate the temperature by varying the amount of warm engine coolant that flows through the heat exchanger. The *Shinko* temperature controller did this by controlling the mixing valve while using the engine coolant outlet temperature as a control set-point. Throughout testing, the coolant outlet temperature was set to hold at 85 °C.

Engine coolant outlet temperatures on production automobile engines control the temperature to approximately 90 °C. The set point of 85 °C was chosen as it provided an adequate coolant temperature to allow for effective cooling while leaving a temperature buffer that could be used to protect the engine in case of a cooling system failure.

Allen-Bradley MicroLogix 1200 PLC

A programmable logic controller (PLC) is used to control the internal combustion engine in the test cell during operation. The PLC utilized was the *Allen-Bradley MicroLogix 1200* PLC (Figure 9) along with multiple expansion slots. Refer to Appendix C.

The controller used was the *1762-L24BWA,* which has 10 relay outputs and the same number of 24 V DC digital inputs. This allowed for a digital input to be used to activate the override button mounted next to the E-stop button placed in the control room. This override is used to start the engine in conditions that would cause the safety protocols in the control software (RSLOGIX 500) to prevent engine start.

The relay connections allowed for connecting a 24 V DC power supply to either the ignition relay or the starter relay. The *1762-L24BWA* module was powered by 240 V mains power.

Analogue inputs were connected to the PLC via two expansion modules (*1762-IF4*) proving a total of eight channels of input. These channels are either voltage or current based inputs used for various readings. A combo module (*1762-IF2OF2*) was used to provide a further two analogue inputs as well as two analogue outputs. This was done to reduce the number of expansion modules as the PLC was limited to six modules.

The remaining three expansion modules were thermocouple input modules (1762-IT4) providing a total of 12 temperature inputs for the PLC. These temperatures were for monitoring various engine parameters such as exhaust or coolant temperatures.

Figure 9: MicroLogix 1200 PLC and Expansion Modules

AVL Gravimetric Fuel Flow Meter

An AVL 7030 fuel flow controller module was used to connect and control the AVL 7030-06 fuel flow meter. It received a fuel mass signal for the gravimetric flow meter that it output to the PLC as the instantaneous mass of fuel in the flow meter. This signal was used, along with time, to calculate the change in fuel mass within the flow meter.

The AVL gravimetric fuel flow meter had a built-in calibration feature, which placed a custom-made calibration weight onto the load cell. This measurement was used to adjust the signal gain and linearity along three points of measurement.

Schenck LSG2000

The *Schenck LSG2000* control module was used to control the Schenck eddy current dynamometer. It connected to the safety circuit of the dynamometer as well as to the PLC where it received a speed input for one of the PLC analogue outputs. The controller also signalled to the *Schenck LEW2000* the appropriate dynamometer coil current.

Schenck LEW2000

The *Schenck LEW2000* simply provided the necessary current to the eddy current coil in order to create the magnetic field needed. It received power from the 240 V mains and received signal input for the *Schenck LSG2000.*

Throttle Controller Module

The throttle controller module provided the signal to the actuator that controlled the throttle opening. It received an analogue input signal from one of the PLC analogue output connections. It was powered by a 3-phase power connection connected to a 3-phase power outlet.

Lambda Scanner

An ETAS LA2 lambda scanner was used to independently measure the air-fuel ratio in the engine. The sensor was mounted in the exhaust downpipe and the ETAS scanner sent a voltage signal to the ETA (Engine Test Automation) software where the data was recorded.

See appendix C for more information on the wiring of the instrumentation.

3.2.3 Dynamometer

An eddy current dynamometer was used to supply a load to the engine. It was connected to a *Schenck LEW 2000* power supply and *Schenck LSG 2000* controller to control the dynamometer speed and torque.

The dynamometer control used two different methods, speed control and torque control. In speed control mode, a speed set point was set. If the dynamometer speed input detected that the engine was rotating above this speed, the dynamometer would brake the engine, slowing it until the speed set point was again reached. The resultant toque could only depend on the throttle position set by the operator.

In torque control mode, a torque set point was set concurrently with an engine speed. The PLC would adjust the throttle position to match the torque set point at a set engine speed. When the engine was initially started, speed control was used to set the engine speed. Once completed, torque control was used to set the desired torque. This reduced the chances of the controllers behaving abnormally and damaging the engine.

See Appendix B for more information on the dynamometer.

3.2.4 Meriam Air Flow Meter

In order to measure the volumetric air flow, a laminar flow sensor was connected to the air intake. This flow sensor directs air flow through many small channels where the measured pressure drop is proportional to the volumetric flow rate.

This meter was calibrated using a wind tunnel and a ΔP pressure transducer. For calibration, a known air mass flow rate was forced through the meter and the associated pressure drop was measured. The data could be used to correlate the pressure drop measured across the meter during engine operation to the mass flow rate of air moving through the engine. See Appendix D-1 for calibration information

3.2.5 Temperature Sensors

A multitude of temperature readings were performed. The following is a list of all the temperature reading took in the test cell:

- Exhaust
- Exhaust cylinder 1-4
- Engine coolant inlet
- Engine coolant outlet
- Dynamometer water outlet front
- Dynamometer water outlet rear
- Intake air
- Ambient air
- Engine oil sump

3.2.6 Pressure Sensors

An absolute pressure sensor was installed on the intake manifold to measure the absolute manifold pressure. This sensor was connected to an analogue input of the PLC, where the pressure was recorded. This value is used to peg the pressure trace recorded by the in-cylinder pressure sensor.

Oil pressure was measured using a gauge pressure sensor connected via a braided hose to the oil channels. The voltage signal was sent to the PLC and calibrated in the Engine Test Automation (ETA) software.

A gauge pressure sensor was used to measure the fuel pressure. It was placed directly after the engine fuel pump and calibrated in ETA.

3.3. Engine Control Unit

An analysis of the OEM ECU was performed to provide a base for the aftermarket ECU.

3.3.1 Original Equipment Manufacturer ECU

The original OEM ECU was connected via a Bluetooth OBD2 (on-board diagnostics) connector. Third-party software was used in conjunction with the OBD2 connector in order to interrogate the ECU. Parameters such as spark timing, engine coolant temperature, and air-inlet temperature can all be recorded using the third-party software.

A major disadvantage when using the OEM ECU was the inability to adjust air-fuel ratio or spark-ignition timing. This necessitated the replacement of the stock ECU with an aftermarket ECU.

3.3.2 Perfect Power XMS5A/B ECU

The stock OEM ECU was replaced with a Perfect Power XMS5A/B. This allowed for wide band lambda control and could be used in engines with up to 8 cylinders.

It was chosen over other competitors due to its value for money and its ease of use. Alternate ECUs could be found from various suppliers and these possible ECUs were studied in terms of functionality and price. It was concluded that the Perfect Power XMS5A/B was the best suited to the application and also had good technical support.

The ECU was installed following the accompanying installation instructions. The Perfect Power XMS5A/B constitutes the following inputs/outputs (which were all used in this study):

- Spark-ignition
- Fuel injection
- Idle throttle control
- Crankshaft position
- Camshaft position
- Throttle position
- Intake manifold pressure
- Engine temperature (engine coolant outlet temperature)
- Air inlet temperature (intake manifold)

The spark-ignition was controlled via connectors connected to a four channel Blue Fire ignition amplifier. A wasted spark arrangement was implemented, which results in two spark plugs firing simultaneously. This simplified the circuitry needed to control the spark plugs.

The Perfect Power XMS5A/B has 2 A injector drives, which mean each driver is capable of handling 1 x 10 Ω or 2 x 20 Ω injectors. The injectors used in the engine were measured at 12 Ω and were thus deemed suitable to the study.

The manifold absolute pressure sensor used by the Perfect Power XMS5A/B comes built into the ECU. This required a simple pneumatic tube connection from the manifold to this sensor. This connection was checked for leaks as this is a major calculating parameter for spark timing and fuelling. Air temperature was connected via the intake manifold's housed pressure and temperature sensor. As stated previously, the OEM intake manifold pressure sensor was not used. Engine temperature was connected to the engine coolant outlet sensor to provide the ECU with cold start compensation. The OEM throttle, camshaft and crankshaft positions sensors were connected to the Perfect Power XMS5A/B.

The ECU was used to change the spark timing and alter the air-fuel ratio for different load and speed conditions. This was done to determine the influence of these changes on the engine performance, combustion, in-cylinder pressure, and fuel burn rates.

Figure 10 shows the *LetRipp V2* software that was used to programme the Perfect Power ECU installed onto an engine. The fuel injector map, as currently shown, can be used to fine tune the fuel injection duration. The horizontal axis is the absolute manifold pressure, while the vertical axis is the engine speed. The horizontal axis can also be set to throttle position. However, due to the non-linear sensitivity of the throttle to load, it was found to be easier to tune the engine when the load was related to the inlet manifold pressure.

Compensation tables can also be used to alter the fuelling or spark-ignition timing depending on other factors such as engine coolant temperature or inlet air temperature. Spark dwell timing as a function of engine speed can also be set (Perfect Power, 2017).
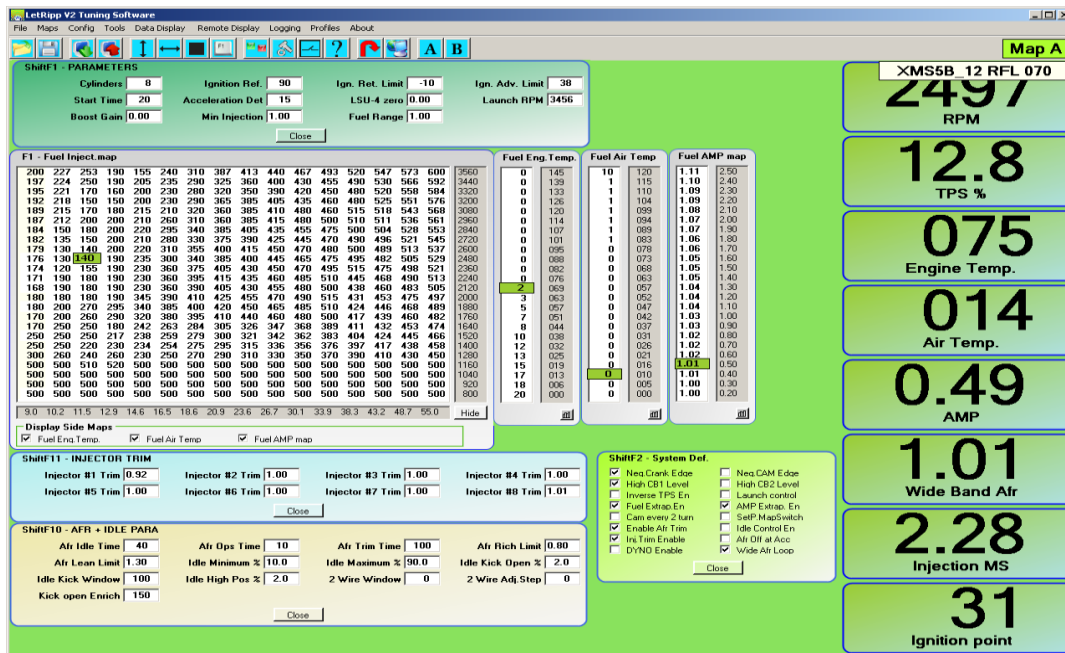
Figure 10: ECU Control Software

3.4 Engine Test Automation (ETA)

During engine operation, the operator used ETA to control and monitor the engine. The software was used to interface with the PLC and was therefore how the operator set the speed and load conditions of the engine. The majority of the engine performance data such as power output, temperatures, pressures (with the exception of in-cylinder pressure), and mass flow rates were recorded using ETA.

Figure 11 shows the ETA software custom graphic user interface set up specifically for this study. The ignition and starter relay controls were positioned at the top left, with speed and torque control mode selection placed just underneath. Recorded engine performance such as engine speed, torque, fuel flow rate, and lambda with derived engine performance (such as power and specific fuel consumption) is shown as well.

The current mass of fuel in the AVL gravimetric fuel flow meter is also shown as this provides the operator with a reasonable indication of when the meter will refill. This is important as during refilling, the measured fuel mass flow to the engine becomes inaccurate, thus the recording of engine performance must be avoided during these instances.

The temperatures shown in Figure 11 entail of the majority of the temperature readings, with additional temperature readings placed onto a new screen. A temperature graph plot through time is used to monitor current temperature trends, with atmospheric conditions also being recorded. The AutoTest feature was not used in this study.

ETA incorporates warnings and alarms that can be set in order to help an operator while the engine is running. Multiple temperature warnings were set, including those pertaining to exhaust gas, oil, and engine coolant. An oil pressure warning was also set.
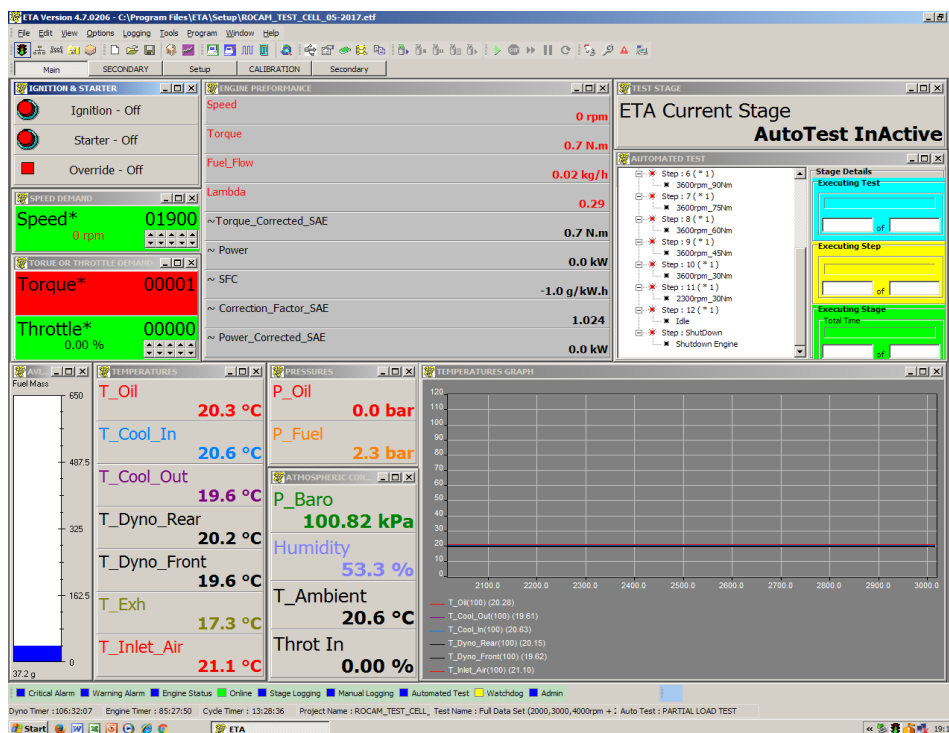
Figure 11: ETA Software Graphic User Interface

3.5 In-cylinder Pressure Measurement

Measuring the pressure within the cylinder during combustion is vital to obtain what is referred to as indicated measurements. In-cylinder pressure can be used to determine IMEP as well as the heat released by the fuel during combustion using heat-release models.

3.5.1 Equipment

The following equipment was used to determine in-cylinder pressure:

- Kistler Spark Plug Piezoelectric Pressure Transducer Model 6117B
- Modified spark-plug to house pressure transducer

38

- Kistler Type 5001 Charger Amplifier
- Kübler 5020 incremental shaft encoder
- National Instruments USB-6212 DAQ
- Variable Power Supply
- LabView 2015

3.5.2 Installation

The spark plug pressure transducer was installed into the engine via the spark plug housing. This was done by simply replacing the standard spark plug with the modified spark plug. This modified spark plug was manufactured by Kistler (see section 2.5.1).

Once installed, the charge amplifier was positioned next to the engine to allow the co-axial cable output from the transducer to reach the input of the charge amplifier. The output of the charge amplifier was a co-axial cable running from the output of the charge amplifier to the input of the USB-6212 DAQ.

The Kübler 5020 incremental shaft encoder was installed by the previous student working on this study (Kenny, 2013:47). It was mounted via a bracket holding it in-line with the crankshaft. It was connected to the crankshaft by a bellows coupling that mitigates vibration transfer from the crankshaft to the shaft encoder. The necessary outputs from the shaft encoder were connected via a cable to the DAQ. This shaft encoder has a resolution of 0.1° crankshaft angle.

The charge amplifier is power by a 240 V connection to the wall outlet, while the Kübler shaft encoder is powered by a variable power supply set to 12 V. The pressure transducer and charge amplifier were calibrated as a system (see appendix D.2).

The usability of the spark plug pressure transducer for accurate IMEP calculations is compromised due the placement and lack of water cooling implemented. For more accurate IMEP calculations, a water-cooled pressure transducer could be used.

3.5.3 Software

LabView was used to record 100 consecutive pressure cycles. This number was chosen as it provided reasonable accuracy without the need to record excessive amounts of data. The code used in LabView was written by a previous student for general usage. Small changes were made to the user interface in order to help the operator record the relevant data (see appendix E.1). A phasing parameter was included to phase the recorded data to allow an intuitive display of the pressure cycles.

4. Engine Test Results

Once the engine test cell was commissioned, engine testing was performed on the in-line 4-cylinder spark-ignition internal combustion engine. Engine test points were selected to provide data over a broad range of engine speeds and loads.

Engine characterisation was done in order to become more familiar with the engine and the behaviour that could be expected from it. The brake specific fuel consumption, exhaust gas temperature, air-fuel ratio (λ), air and fuel mass flow rates, and intake manifold pressure were recorded for five partial load points as well as one full load point at nine engine speeds, as reflected in Figure 12. This was done using the stock ECU for safety as well as to determine stock spark-ignition timing and fuelling.

The OEM ECU installed onto the engine was characterised using an OBD2 scanner and third-party software. This allowed the user to observe and recorded the inputs and outputs of the OEM ECU, such as spark-ignition timing and air-fuel ratio.

The OEM ECU was then replaced with the aftermarket Perfect Power ECU and adjustments were made to the spark-ignition timing and air-fuel ratio. The effects of these changes were recorded for in-cylinder pressure and engine operating parameters.

4.1 Methodology

Once all safety protocols were been completed, the engine was started using the ETA control software. It was left to idle until the engine coolant temperatures and oil temperature had reached adequate levels. The ETA control software was used to set the engine speed and engine output torque to desired points. All steady state data was recorded at a rate of 1 Hz for 60 seconds once the engine reached steady-state operating conditions. Appendix E shows that using a sample rate of 1 Hz for 60 seconds provides fuel mass flow rate data with minimal deviation relative to the calculated mean.

Longer recording segments could have been enforced for more accurate measurement but the changes would have been negligible. Higher power test points also posed the issue of higher oil temperatures, which were limited to 125 °C; leaving the engine running at a high-power test point would lead to this limit being broken.

4.2 OEM Engine Performance and Characterisation

Figure 12 indicates the partial and full load test points chosen. The engine was started and idled until it reached operating temperatures. The lowest engine speed test point was chosen as 2000 rpm to allow the tests to occur in standard operating conditions. The highest engine speed test point coincided with the manufacturer's engine speed limit. The equally spaced engine load points were chosen so as not to reach the peak load for any engine speed.
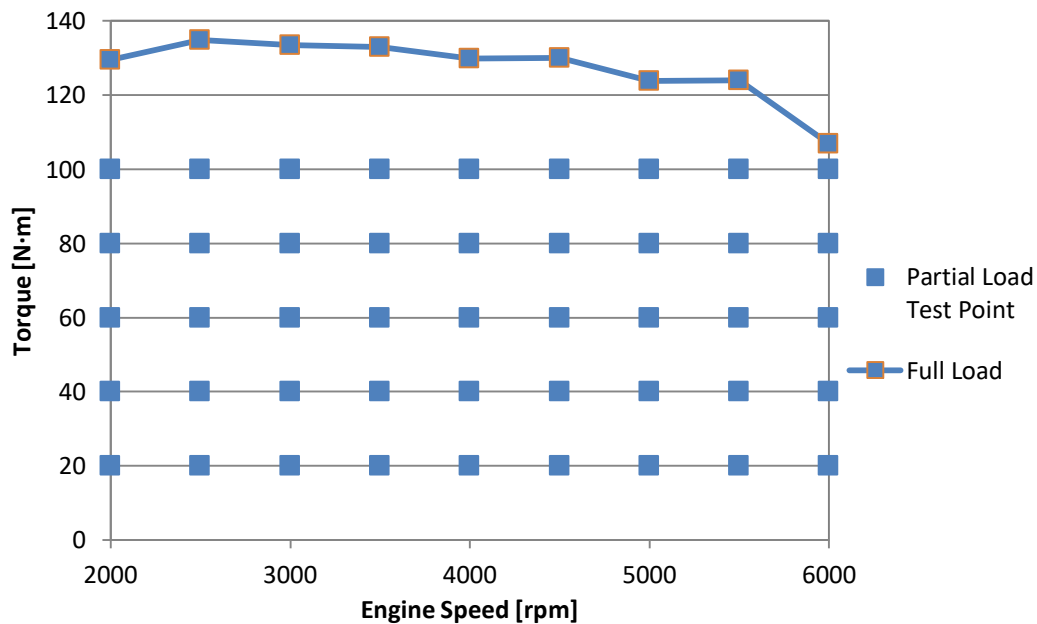

Figure 12: Partial and Full Load Test Points

4.2.1 Partial Load Test

Figure 13 shows how the brake specific fuel consumption (BSFC) changes with engine load and speed. At a set engine speed, an increase in load will yield a lower BSFC, indicating an improvement in thermal efficiency. This is due to the friction rising rapidly with an increase in engine speed, but it does not rise in direct proportion to engine load (Heisler, 1995).

At a constant load, an increase in engine speed will cause an increase in BSFC, therefore a decrease in thermal efficiency will be observed. Friction increases with engine speed, resulting in lower mechanical efficiency and thus lower thermal efficiency, leading to higher BSFC values (Heywood, 2018).

41

At 5500 rpm and 80 - 100 N·m, a rapid increase in BSFC is seen. This is due to the decrease in air-fuel ratio, as seen in Figure 14. The stock ECU (which controls the air-fuel ratio) is programmed to enrich the air-fuel ratio. Enrichment causes a decrease in exhaust gas temperatures (see section 4.6.2) to protect the exhaust downpipe and catalytic converter during higher power engine conditions (Kim, 2015).

The BSFC-curve for 6000 rpm is additionally shown as being significantly higher than the other engine speeds. Figure 14 indicates that the stock ECU, as seen for 5500 rpm and 80 - 100 N·m, is also enriching the air-fuel ratio to protect the exhaust downpipe and catalytic converter.
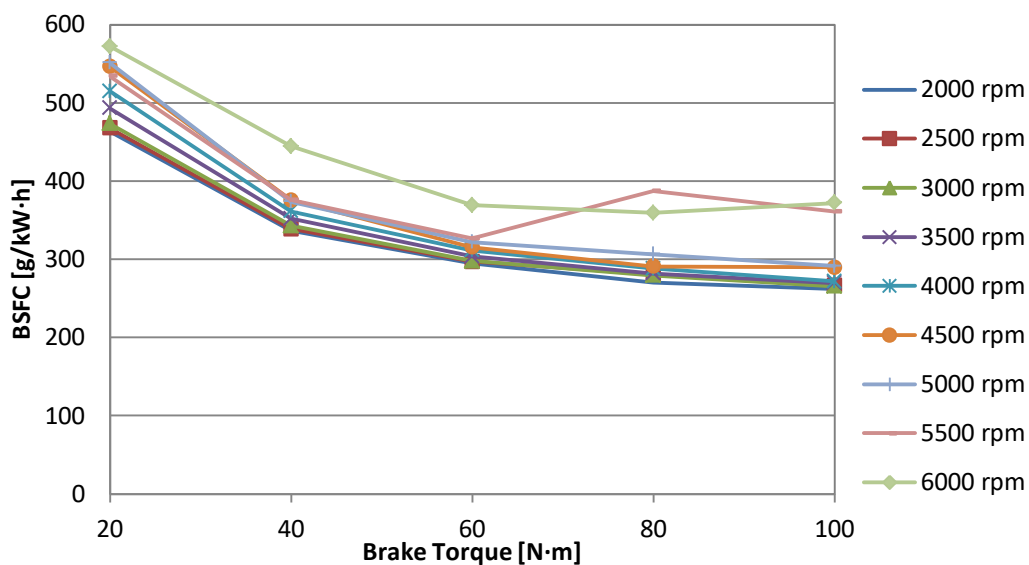
Figure 13: Brake Specific Fuel Consumption vs Brake Torque

Figure 14 further indicates the behaviour of the air-fuel ratio, as controlled by the OEM ECU, where the values of lambda remain relatively constant, apart from high-power conditions. At low to medium engine speeds, the OEM ECU adjusted the air-fuel ratio to be richer than stoichiometric. At higher engine speeds, the engine ran significantly richer than stoichiometric; the effects can be seen in Figure 13.

The value of λ at 5500 rpm and 80 N·m was checked using the air mass flow rate and fuel mass flow rate. It was found to be a value of 0.77 which corroborates the phenomenon occurring at this test point. This is a safety response by the OEM ECU to protect the exhaust down pipe and catalytic converter from excess exhaust gas temperatures.
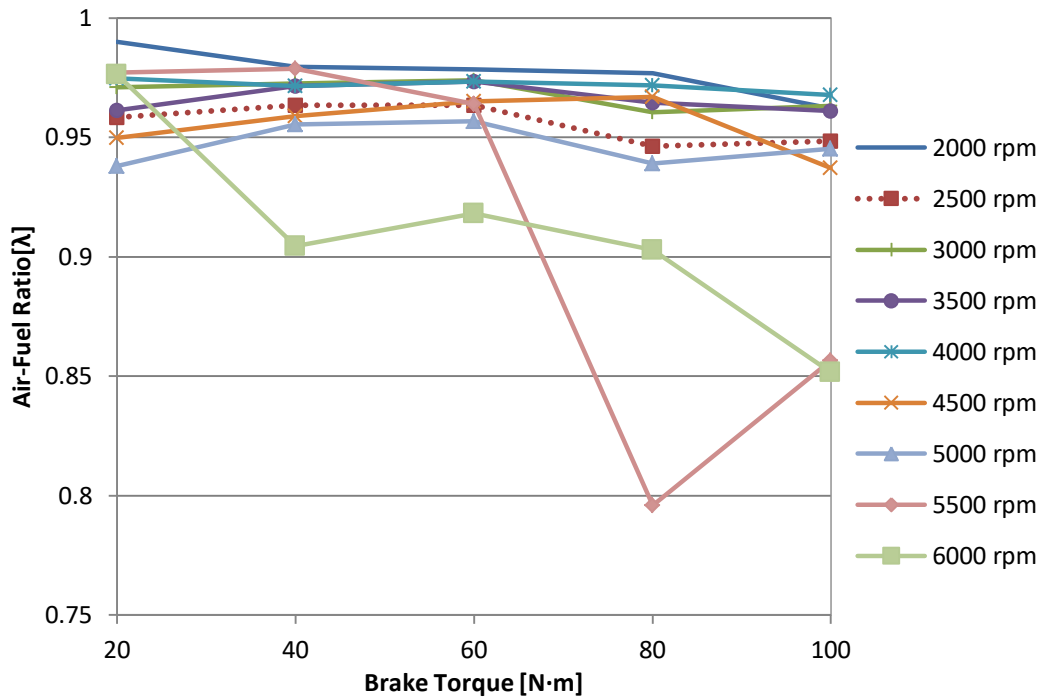
Figure 14: Air-Fuel Ratio (Lambda) vs Brake Torque

The relationship between manifold absolute pressure and the air mass flow rate for a set engine speed is shown in Figure 15. As the manifold absolute pressure is increased, the air mass flow rate increases linearly over higher manifold pressures. For a constant manifold absolute pressure, a higher engine speed will result in a higher air mass flow rate.

Figure 16 shows the variation in air flow for changing manifold pressure and engine speed. A correlation between Figures 15 and 16 in relation to air mass flow rates trends can also be observed. At lower manifold pressure, the linearity of air mass flow rate disappears. This is also seen in both Figures 15 and 16.
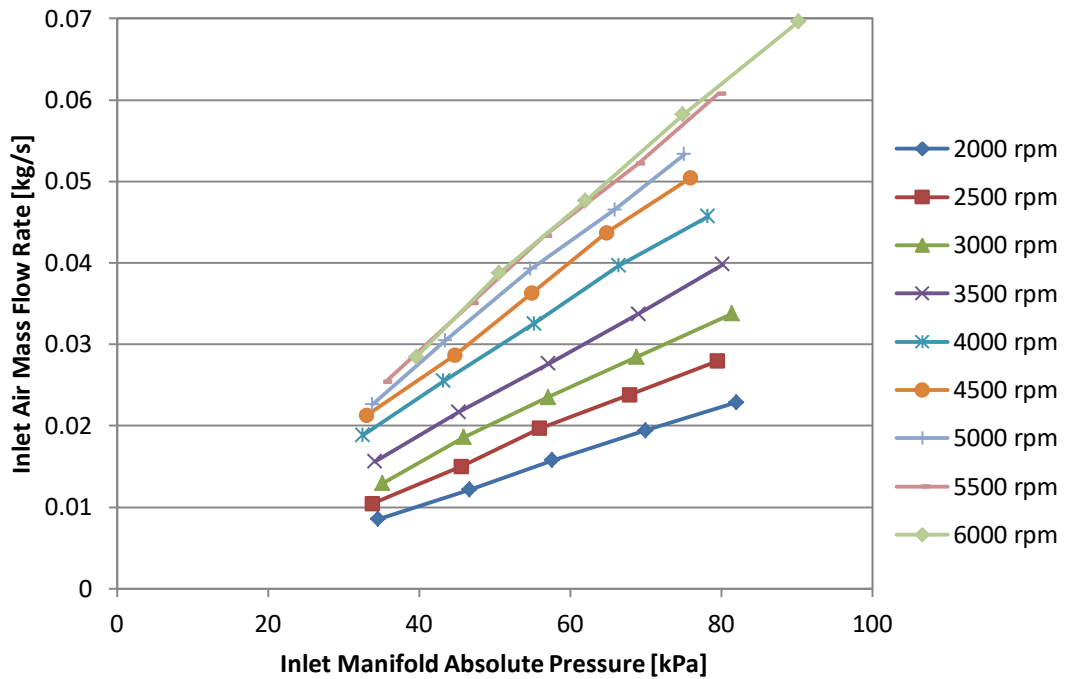
Figure 15: Inlet Air Mass Flow Rate vs Inlet Manifold Pressure
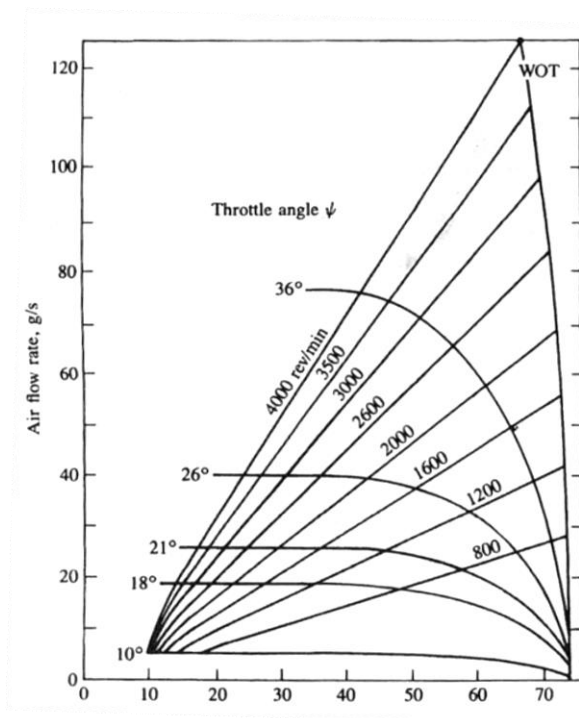
Figure 16: Variation in air flow rate past a throttle, with inlet manifold pressure, throttle angle and engine speed. 4.7-dm3 displacement eight-cylinder engine. (Heywood, 2018)

44

Engine brake torque can be linked to the manifold pressure due to the relationship between the pressure behind the inlet valve and the mass flow rate across the inlet valve. Figure 17 shows that the required manifold pressure for a given engine torque remains approximately constant. Engine speed is shown to have a small effect on the manifold pressure, save for higher engine speeds.

At engine speeds above 5000 rpm, a significant increase in manifold pressure was recorded. This is the combined effect of increased friction within the engine and reduced volumetric efficiency. When friction is increased, the pressure in the manifold must rise in order maintain the brake torque produced by the engine. As volumetric efficiency decreases a greater manifold pressure is needed to move the same mass of air into the cylinder (see figure 18).
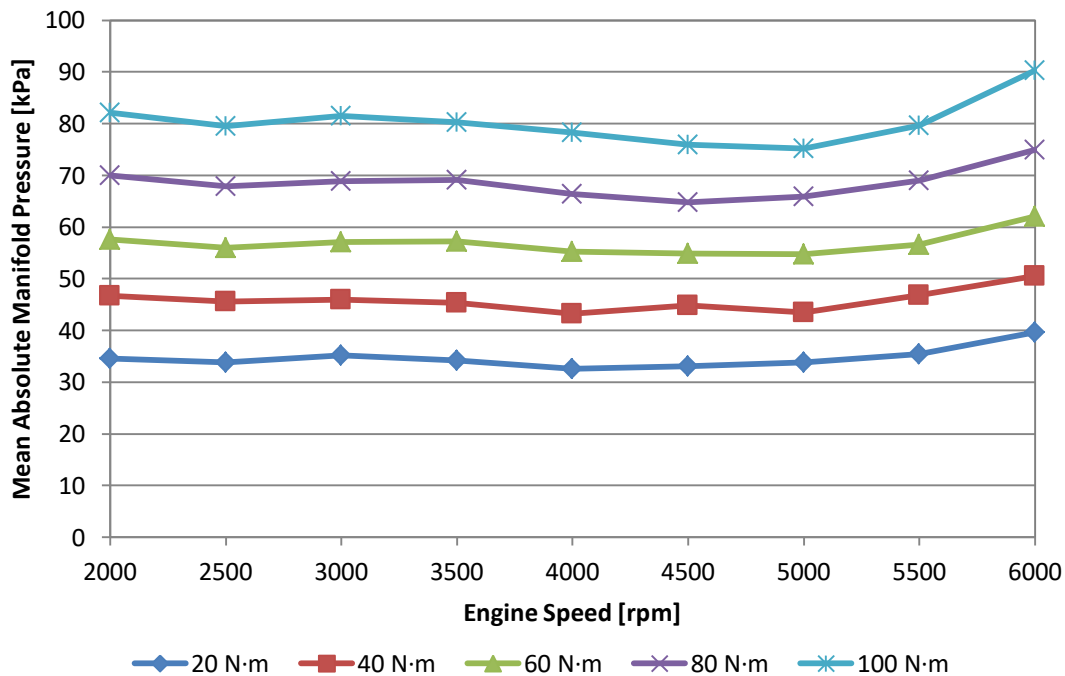
Figure 17: Mean Absolute Manifold Pressure vs Engine Speed

4.2.2 OEM ECU Characterisation

The stock OEM ECU installed on the engine was characterised for a reference of the aftermarket ECU. Using an OBD2 connector with Bluetooth connectivity, software can be used to read the ECU.

45

Third-party software was used to interrogate the ECU and determine the spark timing mapped onto the ECU. These spark timing values were used as references for the spark timing set in the aftermarket ECU. The air-fuel ratio recorded in section 4.2 is also used for the aftermarket ECU.

4.2.3 Full Load Test

A full load test was performed using the stock ECU to determine the maximum performance of the engine. Figures 18 - 21 show various parameters that were recorded for various engine speeds. The torque curve shows a peak torque of 135.0 N·m at 2500 rpm (OEM peak torque is equal to 137 N·m at 2500 rpm). An error of 2% is shown. At speeds greater than 4500rpm a reduction in torque is seen, with the lowest torque seen at 6000 rpm. The volumetric efficiency can be used to determine the mass of air in the cylinder during combustion and shows how there is a decrease in volumetric efficiency after 4500 rpm.

The large decrease in volumetric air flow at higher engine speeds can be attributed to multiple factors, including intake and exhaust system flow friction, intake and exhaust valve flow friction, and intake valve flow chocking at higher speeds (Heywood, 2018). The large drop in torque from 5500 rpm to 6000 rpm is a result of increased friction as the volumetric efficiency drop is not as significant.
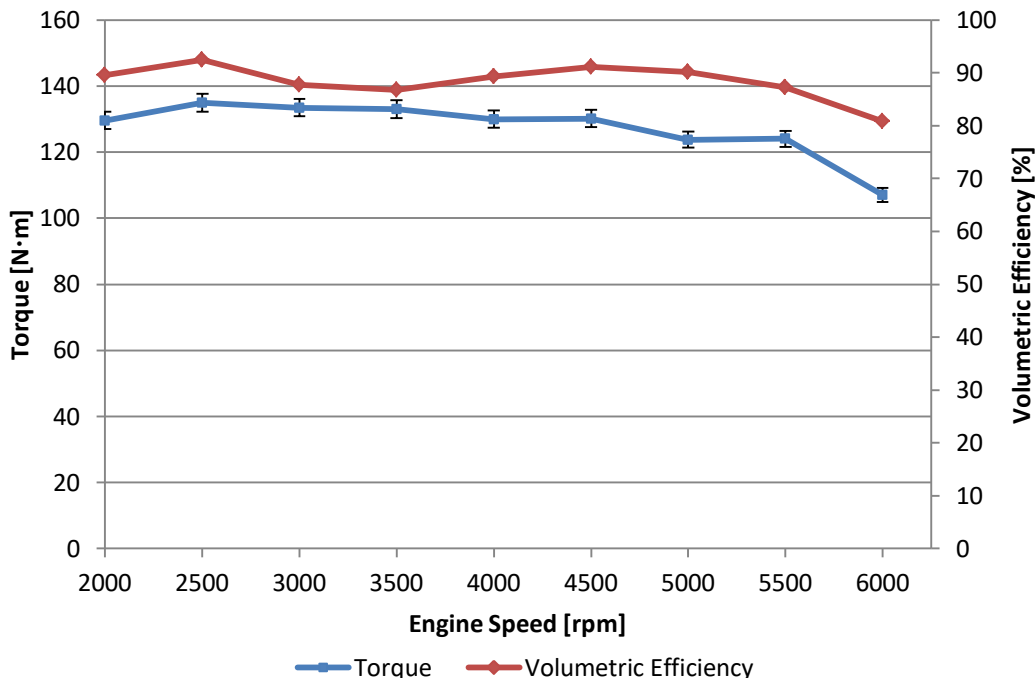
Figure 18: Torque and Volumetric Efficiency vs Engine Speed

The ECE corrected brake power output (see section 2.7.3) of the engine (Figure 19) peaks at a value of 71.5 kW at 5500 rpm (OEM peak power is equal to 70 kW at 5500 rpm). Both the peak torque and peak power measured were within a 3% margin of error. The engine speeds at which these two points occurred were identical to the OEM figures. Fuel flow rate also rises as power increases but shows the added effect of the air-fuel ratio change. This can be observed in Figure 21. The reduction in fuel flow at 5500 rpm is a result of the OEM ECU leaning out the combustion (as seen in figure 21). A check of the volumetric air flow rate and fuel mass flow rate confirmed the increase in air-fuel ratio indicated by the lambda sensor.
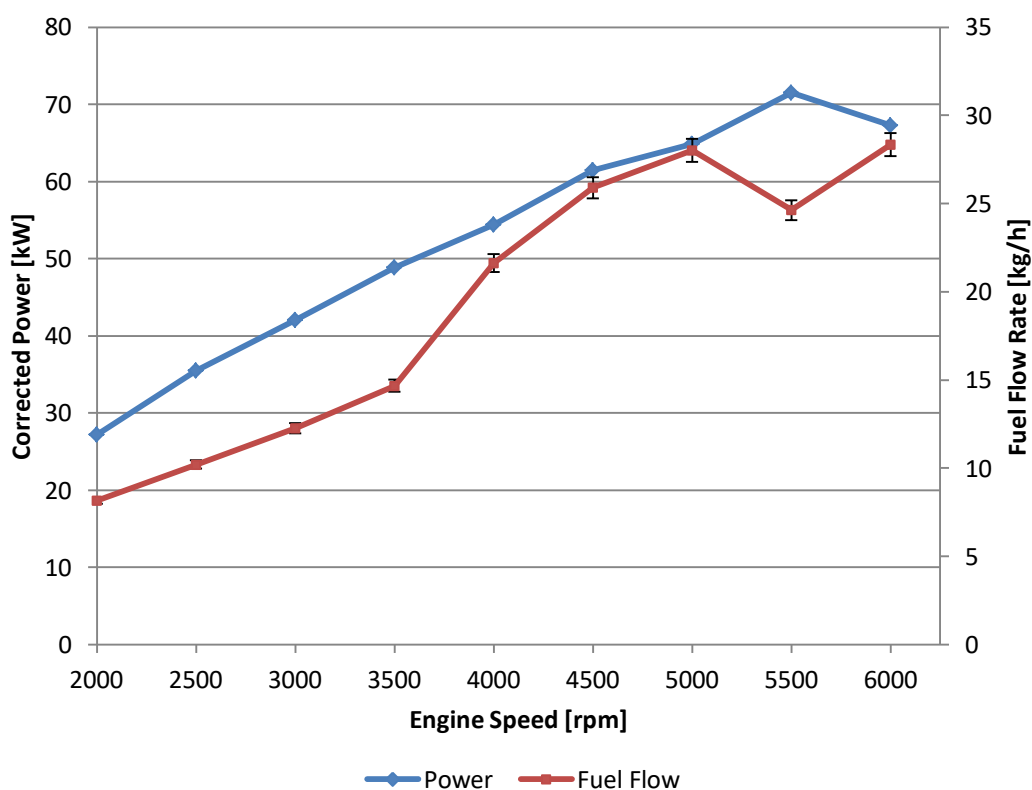
Figure 19: Corrected Power and Fuel Flow Rate vs Engine Speed

Exhaust gas temperature (Figure 20) is a crucial parameter to control in an engine running at full load. This is due to the possible damaged that may be dealt to the exhaust system as well as any exhaust treatment components (for example, a catalytic converter). The exhaust reaches a maximum temperature of 812 °C at peak power engine speed (5500 rpm). Air inlet mass flow rate shows the same

trends as the volumetric efficiency due to the inherent relation of these two parameters.

The BSFC and air-fuel ratio showed in Figure 21, show how the OEM ECU behaves at high loads and speeds. The low speed BSFC values correspond to specific fuel consumption maps for multi-point injection spark-ignition engines (Schäffer & Van Basshuyen, 2004).

The air-fuel ratio is lowered as power increases but becomes leaner once again at peak power engine speeds. The air-fuel ratio range is, however, very rich for the entire engine speed range ($\lambda = 0.7 - 0.9$). The effect on BSFC is drastic as the increase in fuel flow (as seen earlier in Figure 19) does not provide a linear increase in power, leading to a decrease in thermal efficiency.
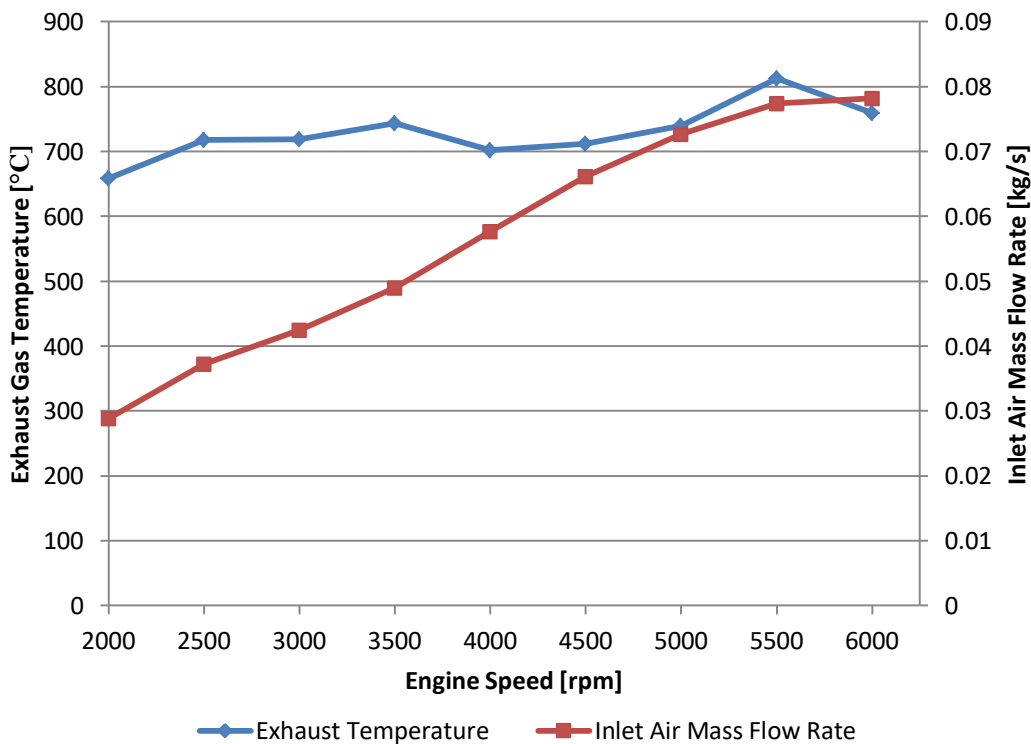
Figure 20: Exhaust Gas Temperature and Inlet Air Mass Flow Rate vs Engine Speed

48
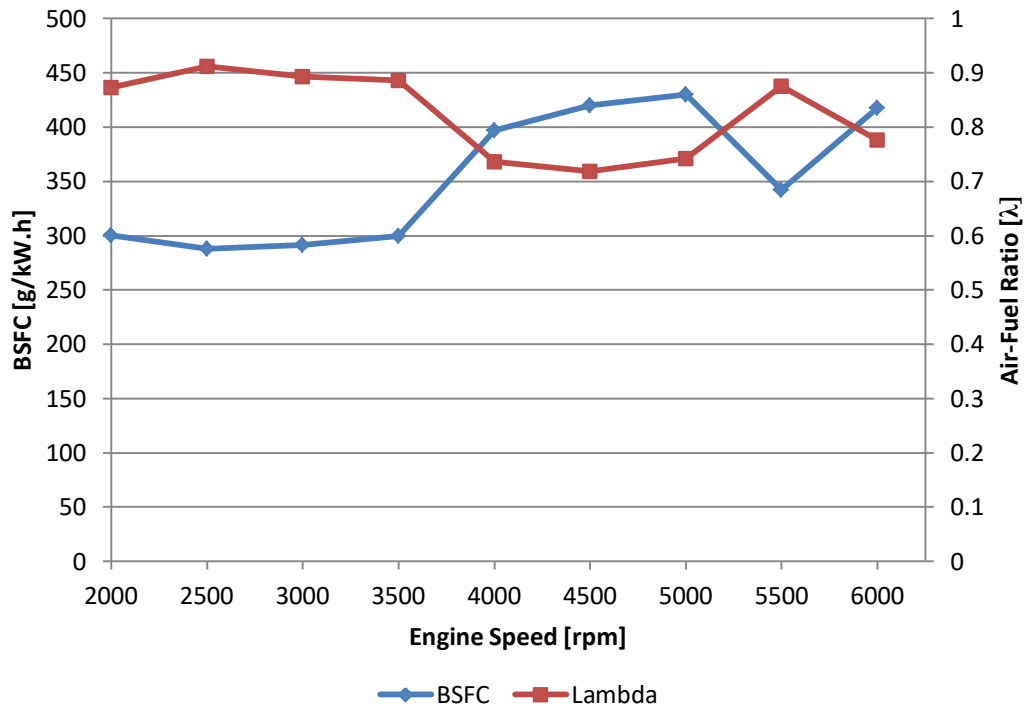
Figure 21: Brake Specific Fuel Consumption and Air-Fuel Ratio vs Engine Speed

4.3 Spark-Ignition Timing

The in-cylinder pressure was measured in the engine for various spark-ignition timing and air-fuel ratios. These parameters were changed using the aftermarket Perfect Power ECU.

For the timing swing, all engine parameters were kept constant (with the exception of the timing of the ignition spark). The air-fuel ratio was controlled by the ECU where λ = 1, while the spark timing range was decided by using the stock OEM spark timing as a reference. To prevent unwanted engine knock due to excessively advanced spark timing, the timing could only be advanced by 8° crankshaft angle relative to the OEM reference spark-ignition timing. The lower end value of the timing swing was chosen to provide a reasonable range to observe the effects of spark timing changes.

Figure 22 shows the aftermarket ECU engine test points that were used. The engine speeds chosen included 2000 rpm and 4000 rpm. A high load of 100 N·m was also used. At 2000 rpm, due to the course control of the throttle position, a low load of 25 N·m was used, while at 4000 rpm, 20 N·m was used.

49
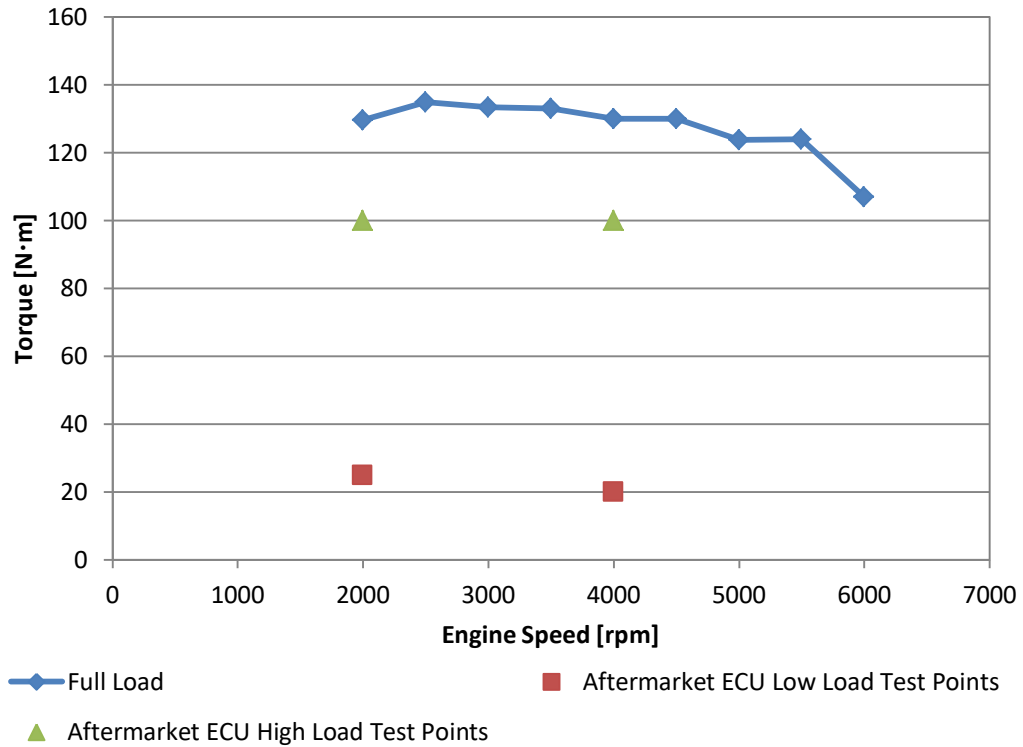
Figure 22: Aftermarket ECU Engine Test Points

4.3.1 In-Cylinder Pressure

Figure 23 shows the peak cylinder pressure for various spark timings while running the engine at various speeds and loads. The peak pressure value increases as the spark timing is advanced for all test cases that can be observed (Polcar & Tunka, 2017). The sensitivity of the peak pressure change is also increased at the higher load points.

50
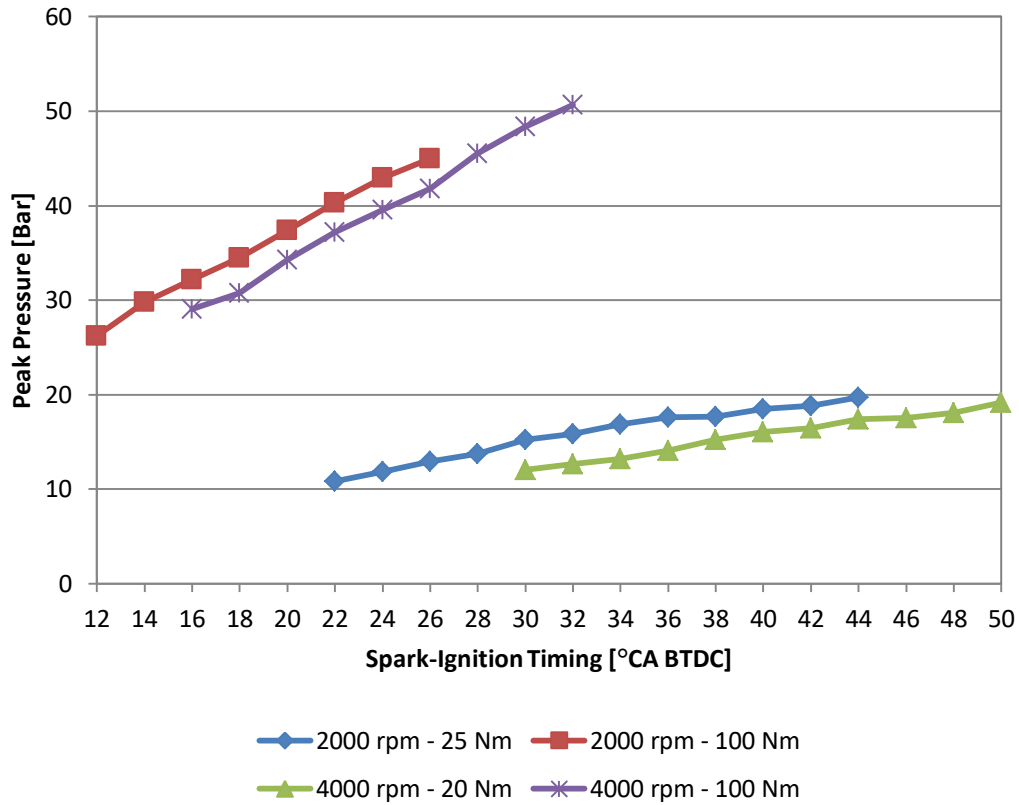
Figure 23: Timing Swing Effect on Peak Pressure

The pressure traces for the four test cases were combined into a single graph (Figure 24), showing the most advanced and most retarded timing for each test case. This allows one to observe how changing the spark timing affects the torque produced by the engine. If the ignition timing is too advanced, the compression work transfer increases as the piston does more work on the in-cylinder gases. If the ignition timing is set too delayed (retarded), the peak pressure occurs later in the expansion stroke and reduces the amount of work transfer from the in-cylinder gases to the piston. The peak engine torque (also referred to as maximum brake torque) will occur with spark-ignition timing that balances these two factors (Heywood, 2018).

Figure 25 shows the same effects of spark timing on the in-cylinder pressure, as seen in Figure 24.
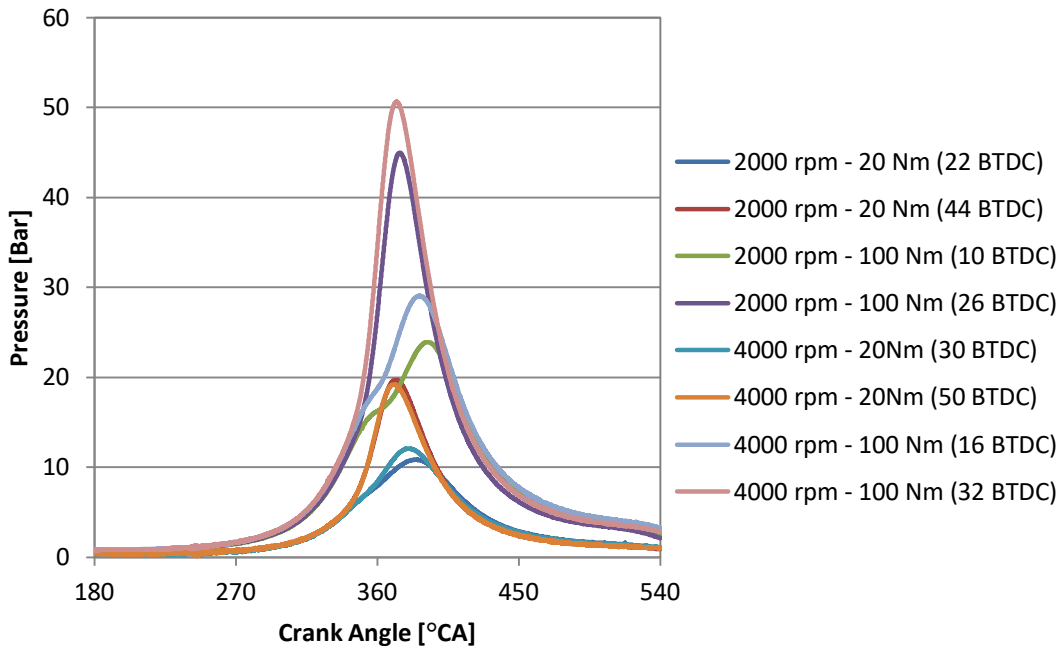
Figure 24: Combined Timing Swing (Most advanced and most retarded ignition timing)
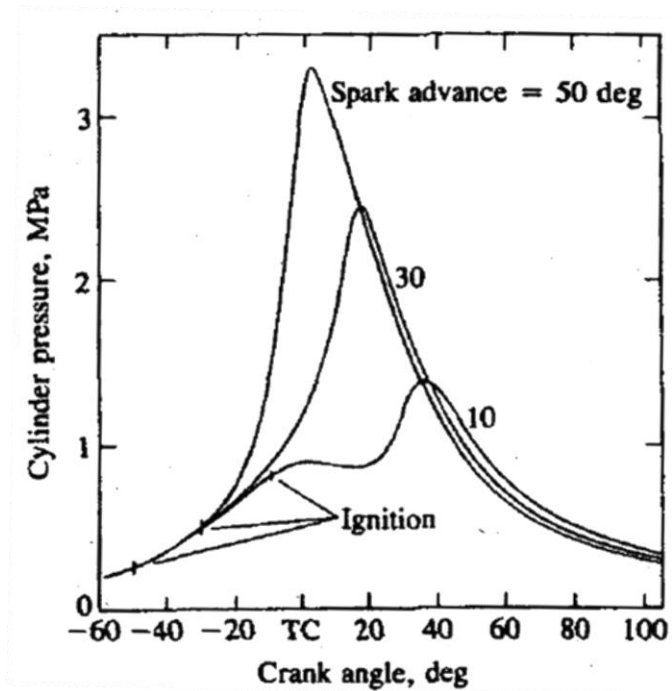
Figure 25: Cylinder Pressure versus crank angle for overadvanced spark timing (50°), MBT timing (30°), and retarded timing (10°) (Heywood, 2018)

The spread of peak pressure over the angle of peak pressure (2000 rpm and 25 N·m) is shown in Figure 26 where the spark-ignition timing has a significant effect. The 100 consecutive in-cylinder pressure cycles are shown with advanced spark-ignition timing resulting in higher peak pressure with less variation in peak pressure angle. The opposite is true for retarded timing as it lead to lower peak pressures and a greater spread in peak pressure position. This is due to greater cycle-by-cycle variation as seen in Figure 27.
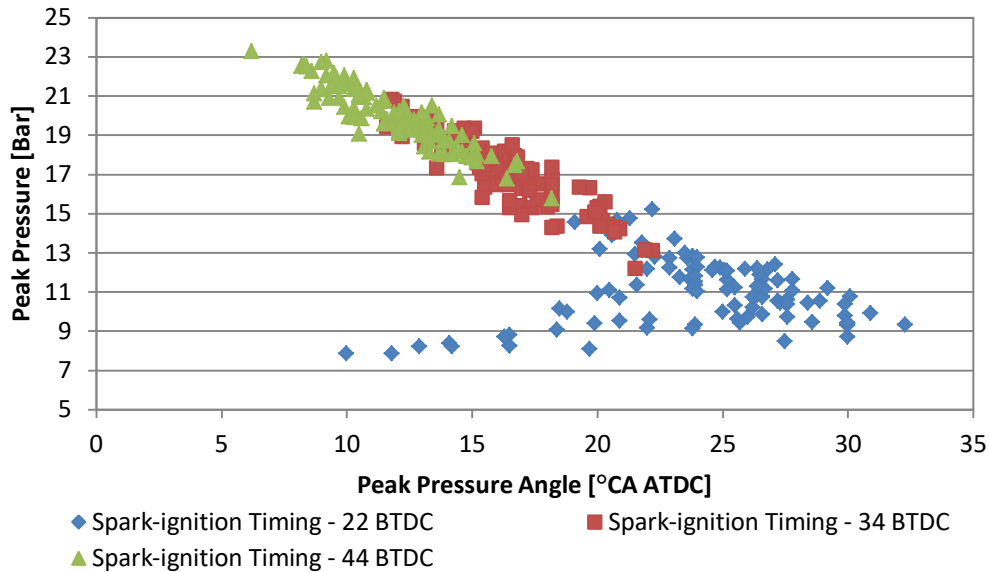
Figure 26: Peak Pressure vs Peak Pressure Angle for various spark-ignition timing
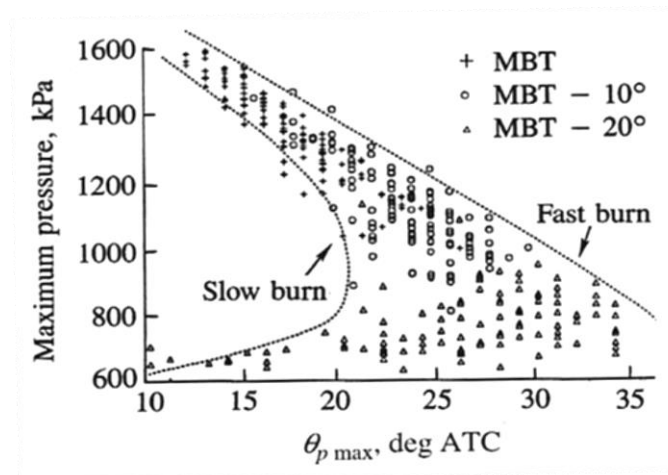
Figure 27: Individual-cycle maximum pressure vs crank angel at which P_max occurs (Heywood, 2018)

53

4.3.2 Engine Performance

The spark timing has a significant effect on the cycle by cycle variation within the cylinder. The coefficient of variation (COV) for $IMEP_{net}$ for the 100 cycles recorded was calculated over the range of spark-ignition timing (Figure 28). As the spark timing was advanced for all test conditions, the COV for $IMEP_{net}$ was reduced. It reached a minimum value where the $IMEP_{net}$ was at a maximum (see Figures 32 and 33); the effects of combustion that is too slow or too fast are minimised due to optimised combustion phasing. Engine load affects the variability of combustion due to lower pressures in the inlet manifold, which lead to greater residuals in the combustion chamber, slowing burn rates (Stone, 2012).

It is important to reduce the COV for $IMEP_{net}$ as excessive cycle by cycle variation ($COV_{IMEP} > 2$ - 5%) can lead to drivability problems (Heywood, 2018).
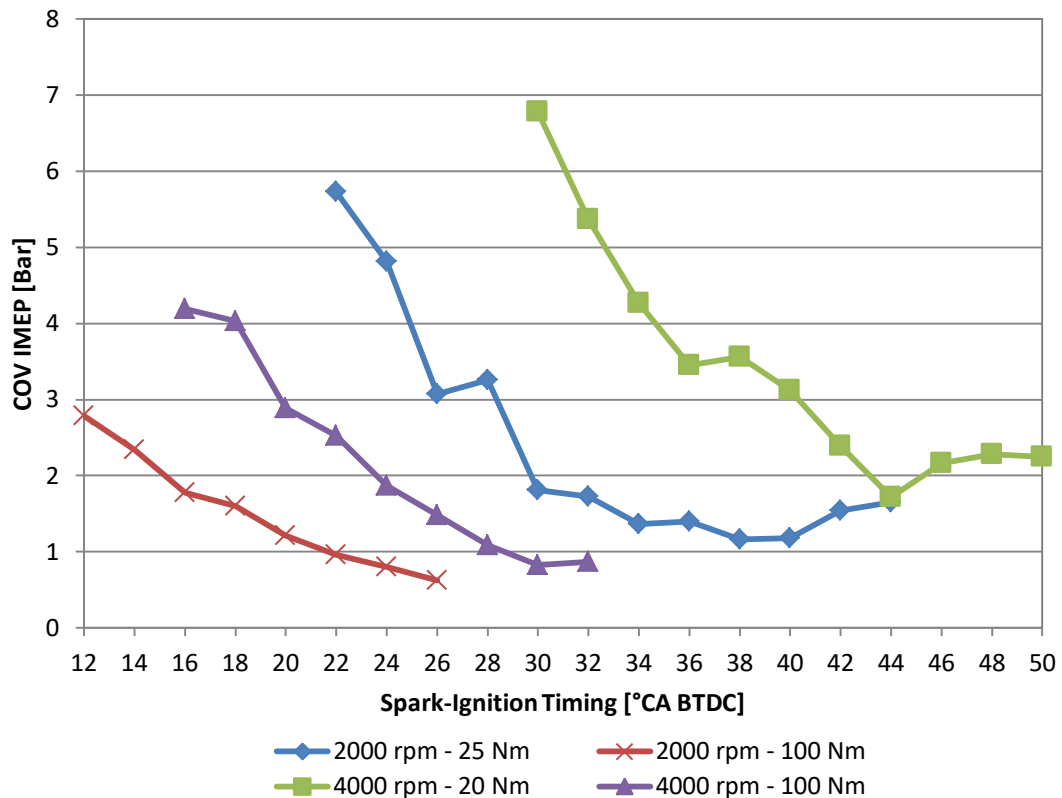
Figure 28: COV_{IMEP} vs Spark-Ignition Timing
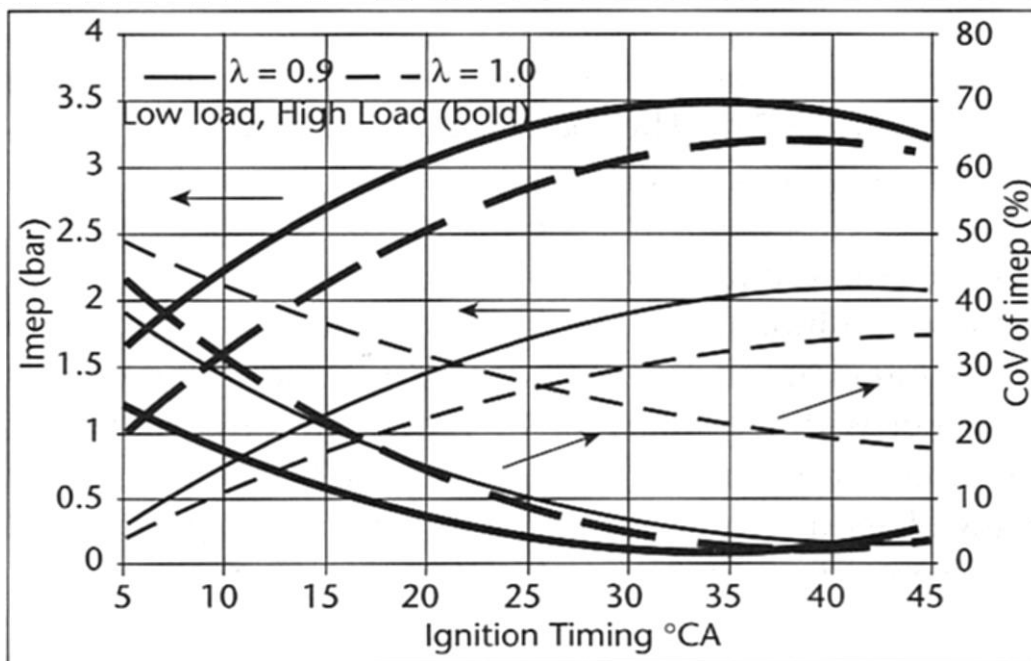
Figure 29: The effect of engine load and air-fuel ratio on the IMEP and cycle-by-cycle variation in combustion (Stone, 2012)

Figure 30 shows the effect of spark timing on exhaust gas temperature. In all test cases, the exhaust gas temperature decreased as the spark timing was advanced. Figures 32 and 33 show how the $IMEP_{net}$ of the engine increased with the advancement of spark-ignition timing. As $IMEP_{net}$ indicates how much work was done by the gases on the piston, the conservation of energy principle would result in the exhaust gas enthalpy being reduced with increased $IMEP_{net}$. If the exhaust gases are assumed to be ideal gases then a reduction in enthalpy would lead to a reduction in temperature (Kakaee, 2013).

BSFC curves (shown with an error of 3%) in Figure 31 show a drop with advanced spark-ignition timing and show a reverse trend to BMEP curves, as seen in Figure 32 and 33. This is due to the higher brake torque produced by the engine while fuel flow rates remain constant (Heywood, 2018).

Maximum brake torque curves are shown in Figures 32 and 33, where the BMEP curves reach a maximum value with spark-ignition advance, before starting to decrease. This is a compromise in terms of spark-ignition timing where advanced timing would result in work being done on the cylinder gases and retarded timing resulting in peak pressure occurring too late, relative to piston position (Heywood, 2018).

55

A standard maximum brake torque (MBT) curve can be seen in Figures 32 and 33 where the MBT spark-ignition timing is shown. A peak in brake torque is seen in the recorded data for all test cases.
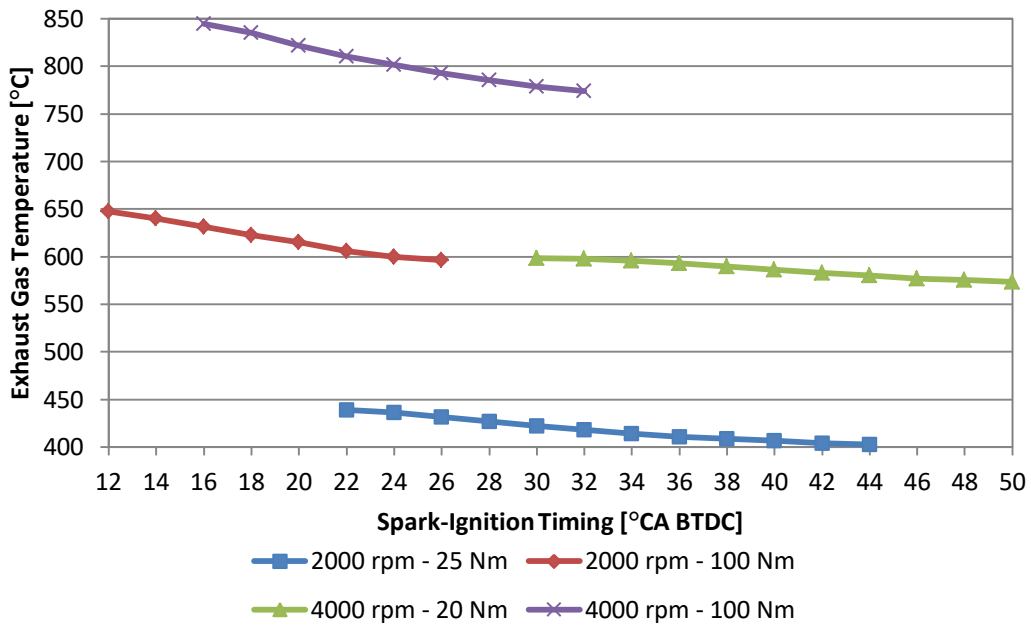

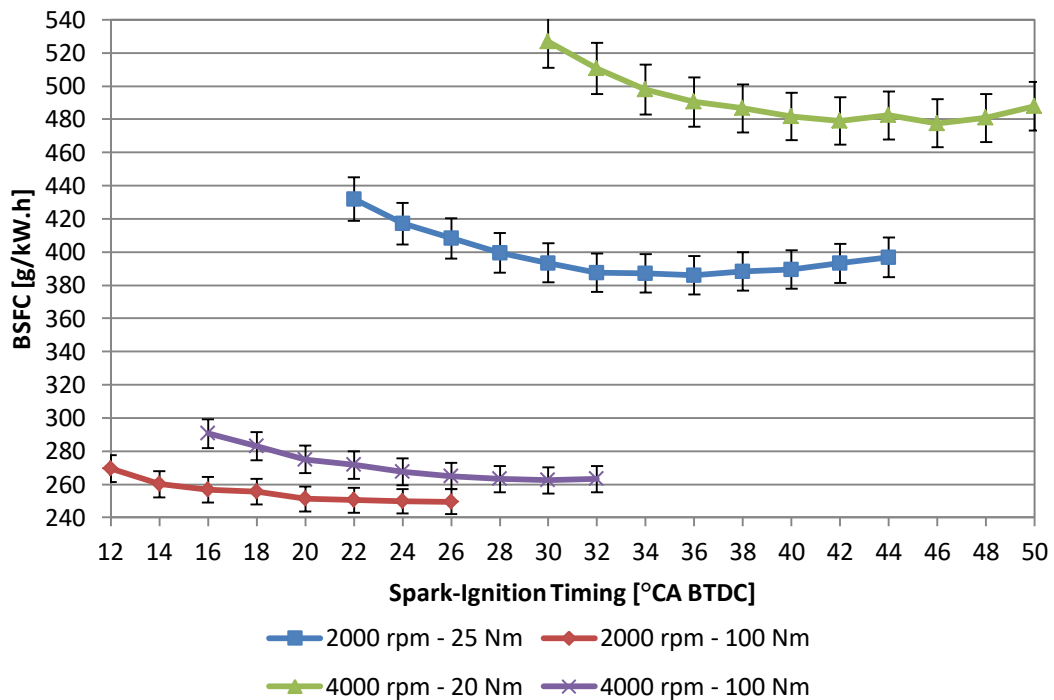**Figure 30: Exhaust Gas Temperature vs Spark-Ignition Timing**

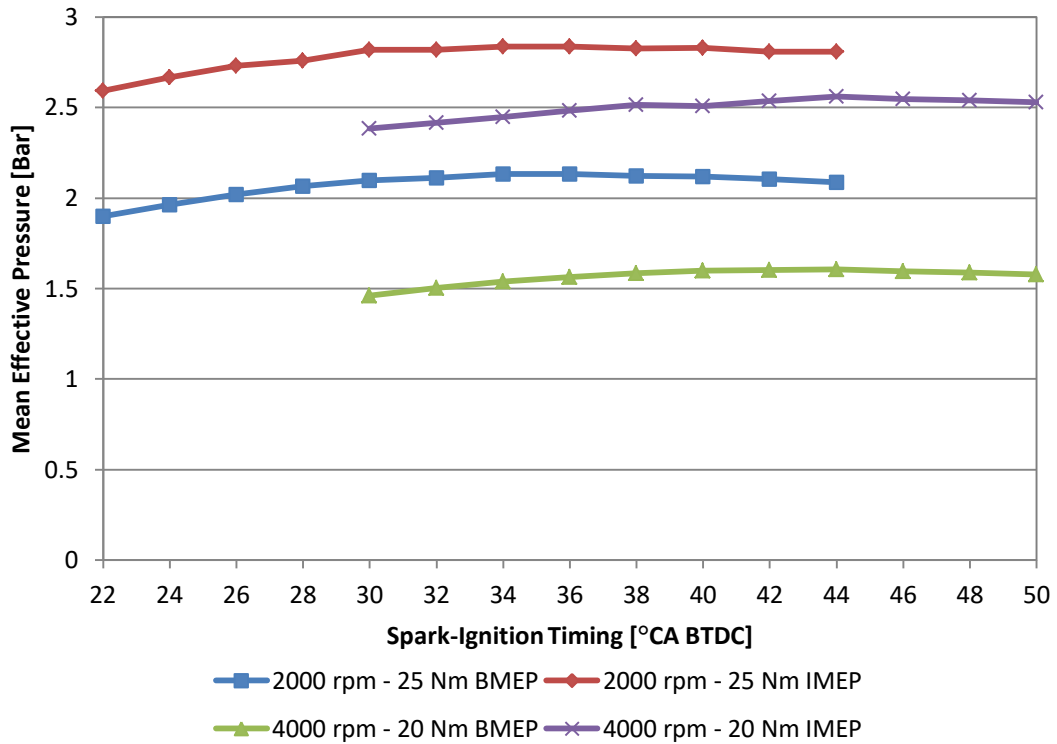**Figure 31: Brake Specific Fuel Consumption vs Spark-Ignition Timing**

56

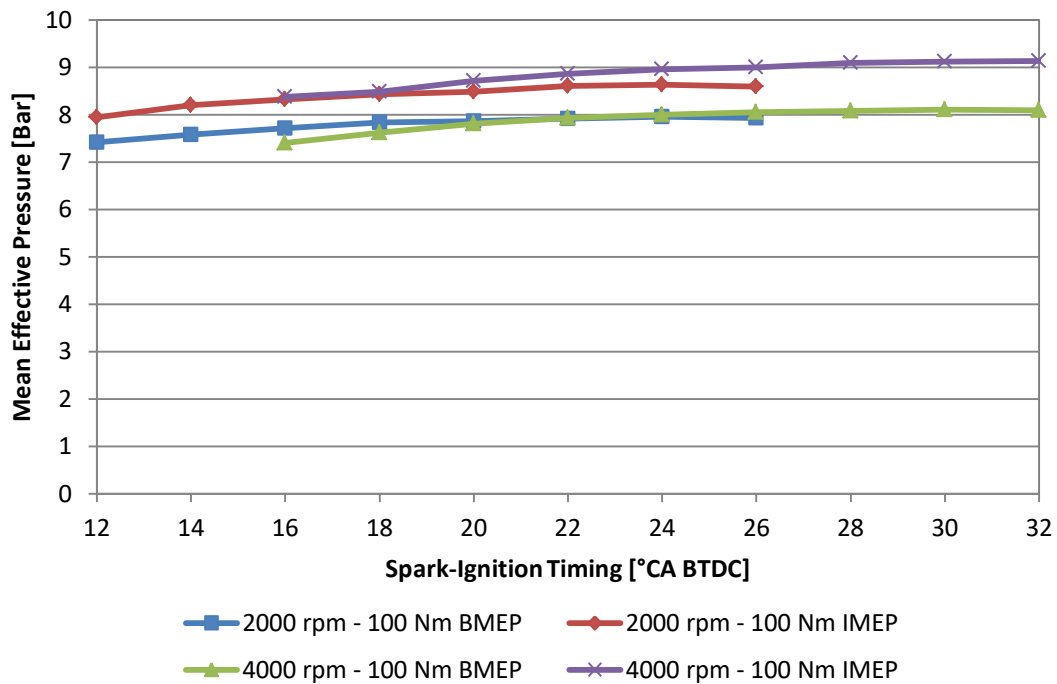**Figure 32: Mean Effective Pressure vs Spark-Ignition Timing (Low Load)**

Figure 33: Mean Effective Pressure vs Spark-Ignition Timing (High Load)

57

Figure 34 reveals the mechanical friction measured for a range of spark timing for each test case. It can be observed that the mechanical efficiency is less dependent on spark timing than on engine load or speed. An increase in engine speed shows a decrease in mechanical efficiency as mechanical friction work increases. The components of total friction are either independent of speed (boundary friction), proportional to speed (hydrodynamic friction), speed squared (turbulent dissipation), or a combination of these components (Heywood, 2018). The values obtained are corroborated in Heywood (2018).

Engine load plays an even larger factor in mechanical efficiency as seen in Figure 35. This figure shows that an increase in load for a set engine speed will increase the mechanical efficiency substantially. This is due to the relative decrease in pumping losses compared to the total friction (Heywood, 2018).
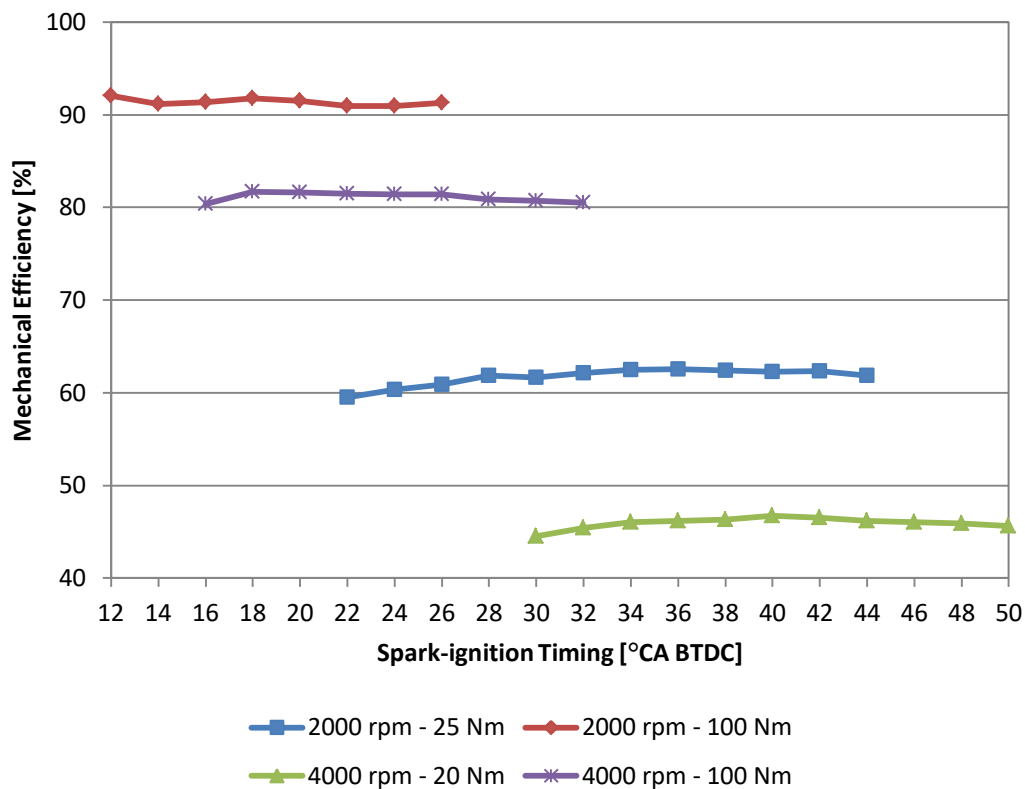
Figure 34: Mechanical Efficiency vs Spark-Ignition Timing
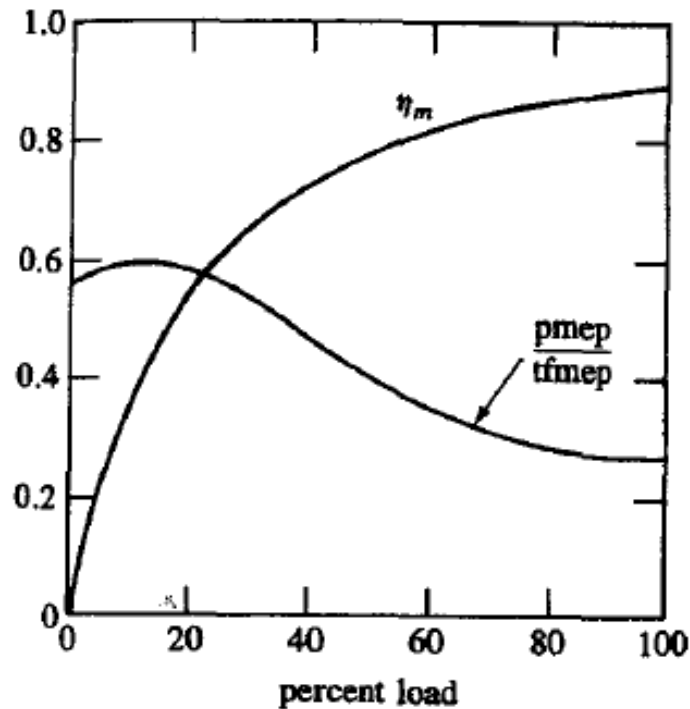
58

Figure 35: Mechanical efficiency (η_m) and the ratio of pumping MEP to total friction MEP as a function of load for a typical spark-ignition engine at fixed (mid) speed. (Heywood, 2018)

4.4 Air-Fuel Ratio

The fuelling swing followed the same methodology as the spark timing swing, where all engine parameters were kept constant with exception given to air-fuel ratio. The spark timing angle was chosen to be 2 - 3° lower than OEM reference for a margin against knock, especially for leaner combustion conditions. The air-fuel ratio range was chosen to provide a reasonable range for both typically rich and typically lean combustion. The high load, high speed test required a limit to the lean air-fuel ratio to protect the exhaust gas system.

The low speed, low load test used spark-ignition timing of 36º BTDC, the low speed, high load condition used 16º BTDC, high speed, low and high load used 42º and 22º BTDC respectively.

4.4.1 In-Cylinder Pressure

Adjusting the air-fuel ratio, while maintaining constant spark-ignition timing changes the peak pressure value as shown in Figure 36. The highest peak

pressures occur when $\lambda = 0.8 - 0.9$. Combustion mixtures leaner than stoichiometric resulted in significantly lower peak in-cylinder pressures.
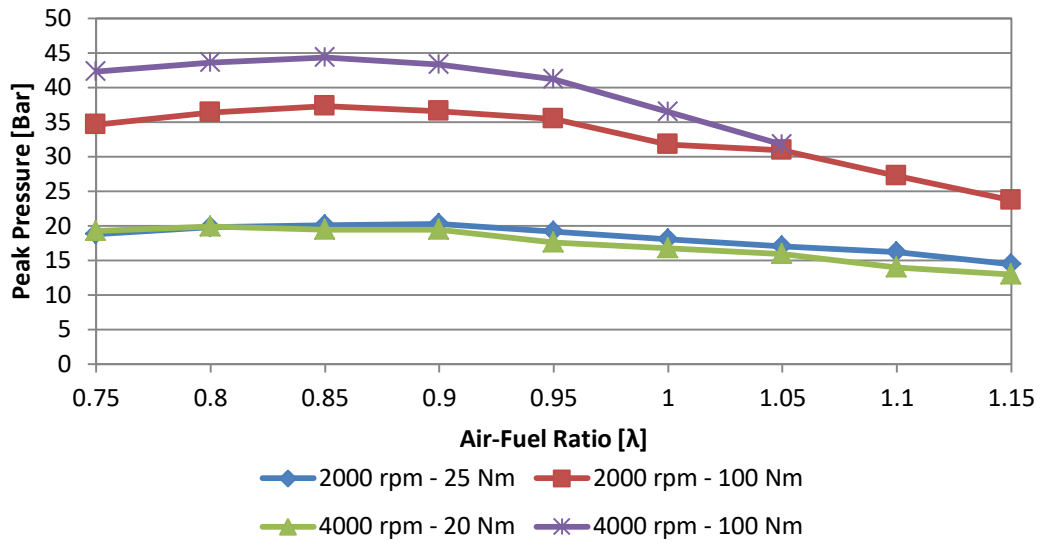

Figure 36: Air-Fuel Ratio Effect on Peak Pressure

Changing the air-fuel ratio has little to no impact on the shape of the in-cylinder pressure as seen in Figure 37.
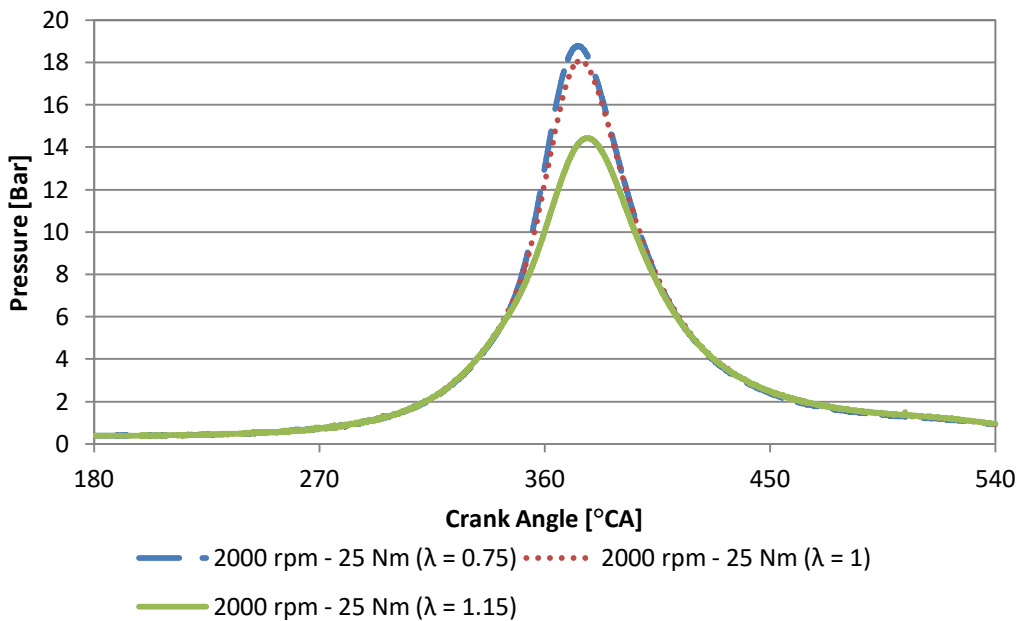

Figure 37: In-Cylinder Pressure vs Crank Angle for Various Air-Fuel Ratios

60

4.4.2 Engine Performance

The COV for IMEP$_{net}$ was calculated for various air-fuel ratios for 100 consecutive pressure cycles (Figure 38). Once the combustion started to become leaner than stoichiometric, the cycle by cycle variation started to increase. This is due to the more rich mixture burning faster and having a higher IMEP$_{net}$ and lower variations in combustion (Stone, 2012). The increase of COV for low speed, low load at $\lambda = 1$ is likely due to anomaly with combustion during that test period.
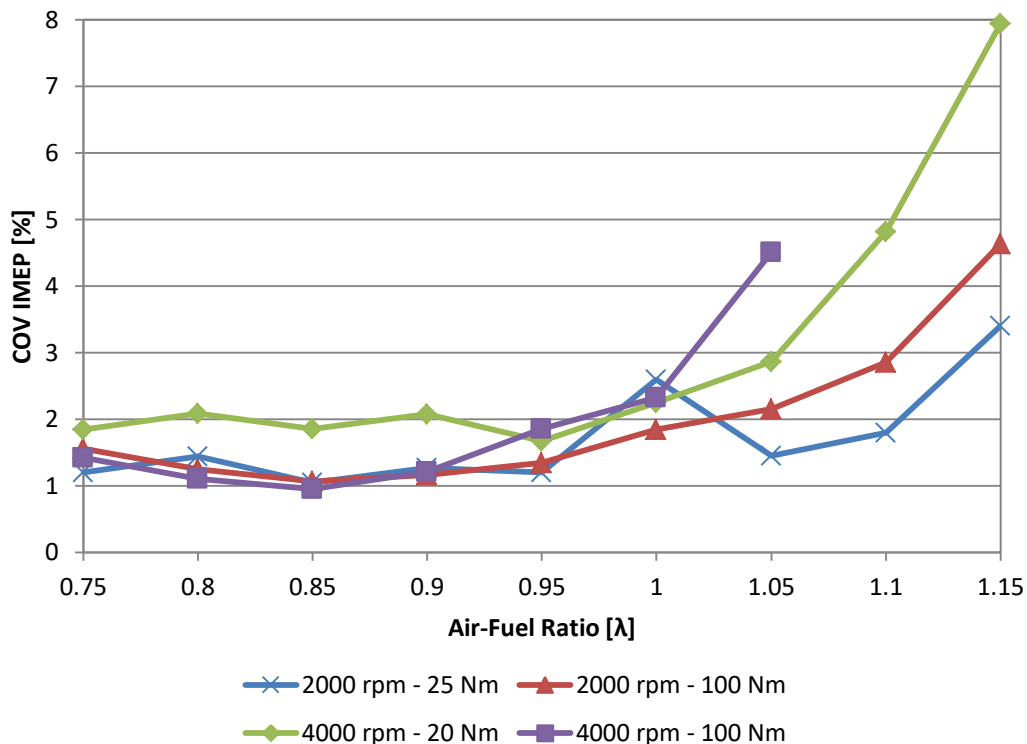
Figure 38: COV$_{IMEP}$ vs Air-Fuel Ratio

Figure 39 shows an initial increase in exhaust gas temperature as the air-fuel ratio was leaned out from a very rich mixture. The temperature peaked at $\lambda = 1.05$ for all tests conditions and then reduced after the air-fuel ratio was leaned out. Figure 39 also shows that running a combustion mixture that is too rich or too lean will drop exhaust gas temperature. As a rich combustion is leaned out, it becomes more efficient, releasing more energy. However, if the mixture becomes too lean, burn rates decrease, leading to lower total energy release and lower exhaust gas temperatures.
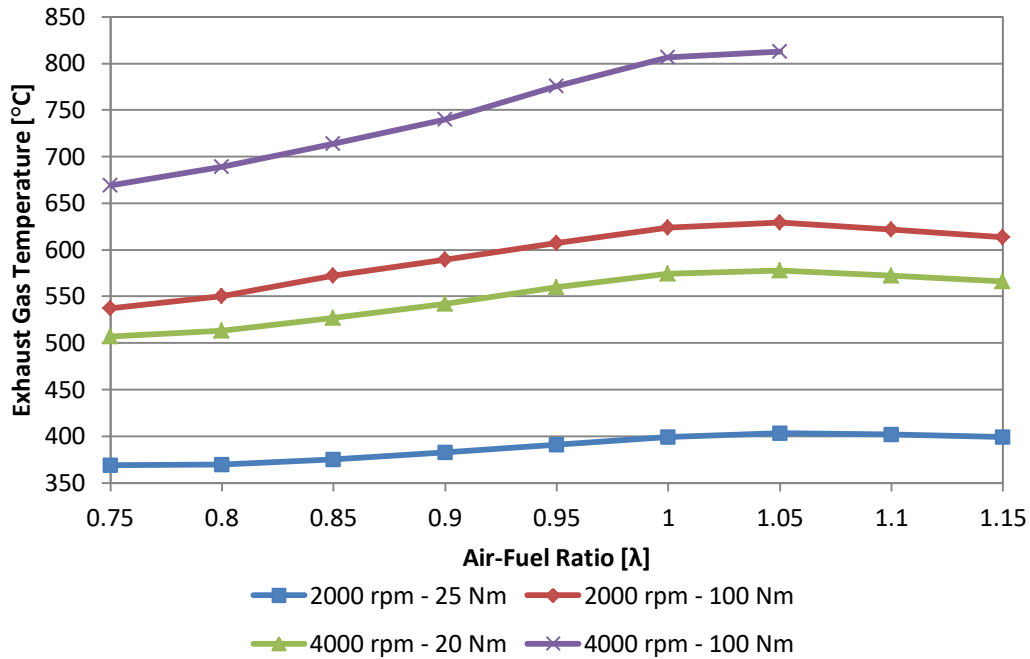
Figure 39: Exhaust Gas Temperature vs Air-Fuel Ratio

BSFC (shown with an error of 3%) will decrease as a rich combustion mixture is leaned out in the range of λ = 0.75 - 1.05 (Figure 40). This is as a result of the reduction in the mass of fuel per combustion cycle being greater than the reduction of brake torque in the air-fuel ratio range of λ = 0.95 - 1.05 (Figures 42 and 43). These aforementioned figures are shown separately to highlight the scale of the effect of air-fuel ratio on the mean effective pressures.

Combustion leaner than λ = 1.05 saw a significant drop in brake torque and therefore the BSFC values saw an increase (Blair, 1999). Figure 41 shows the effect of air-fuel ratio on specific fuel consumption and a decreasing trend in BSFC is seen as the combustion is adjusted to be leaner.
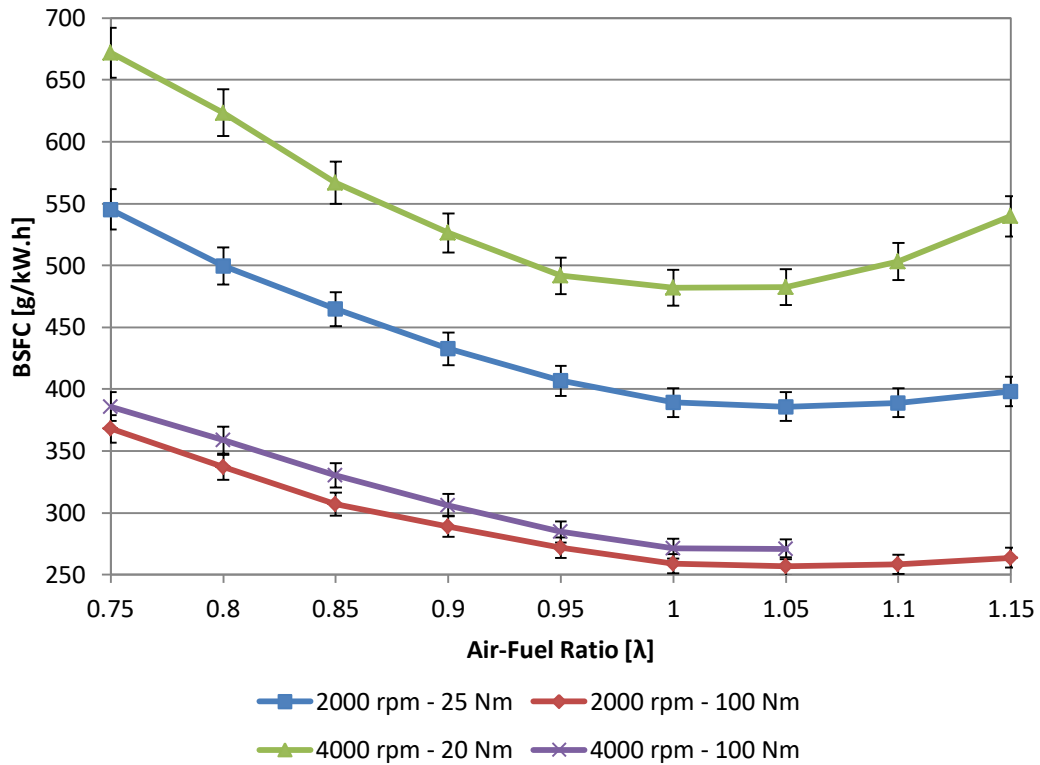
62

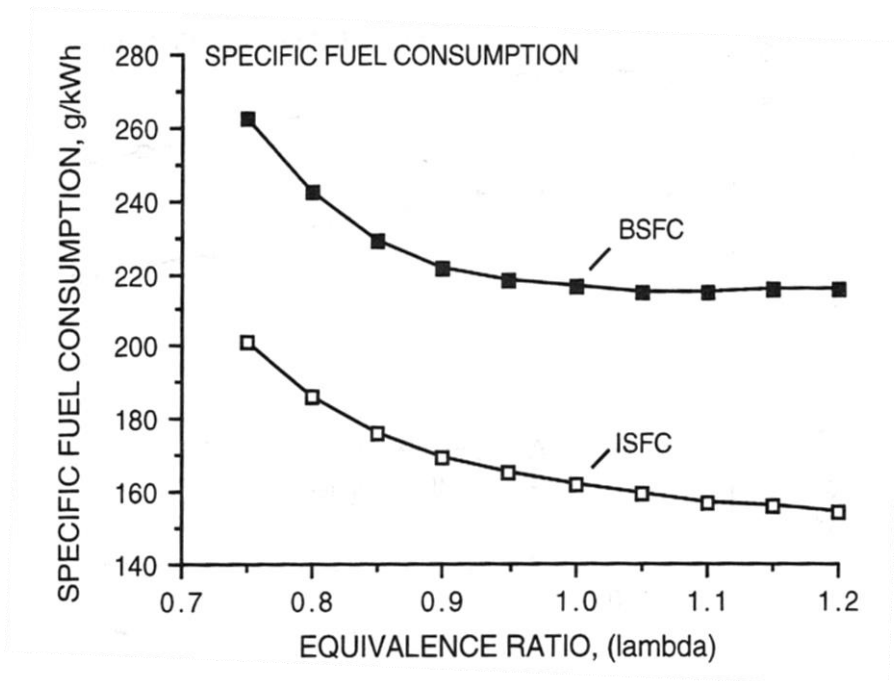**Figure 40: Brake Specific Fuel Consumption vs Air-Fuel Ratio**

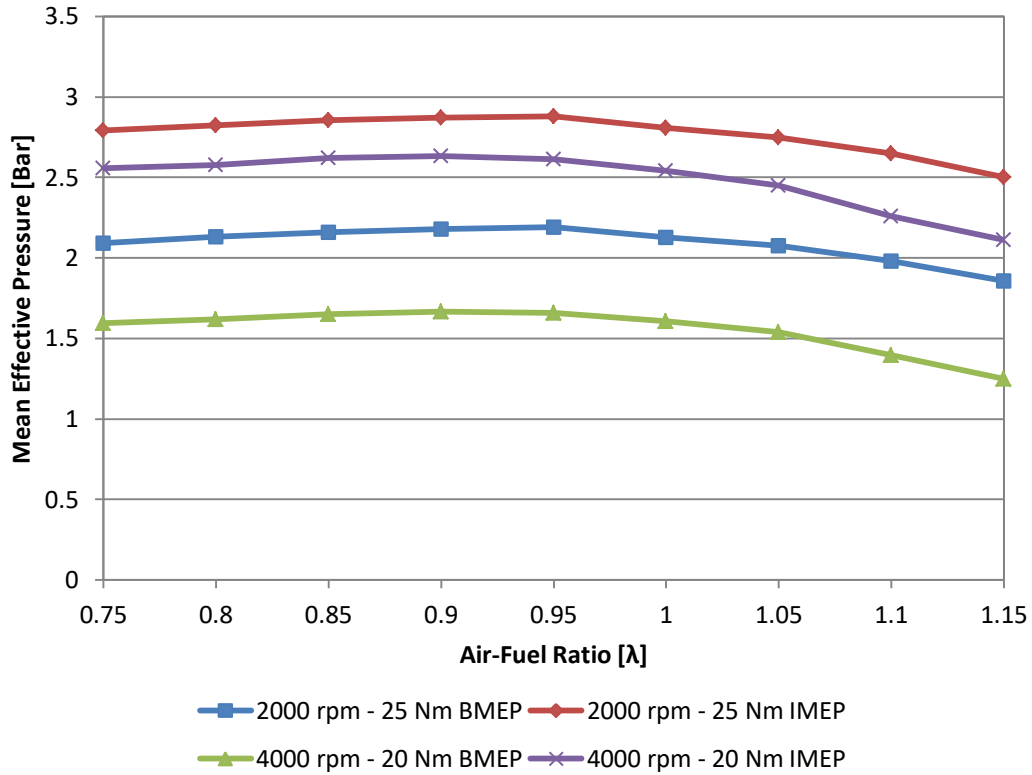**Figure 41: Effect of air-fuel ratio on specific fuel consumption (Blair, 1999)**

63

Figure 42: Mean Effective Pressure vs Air-Fuel Ratio (Low Load)
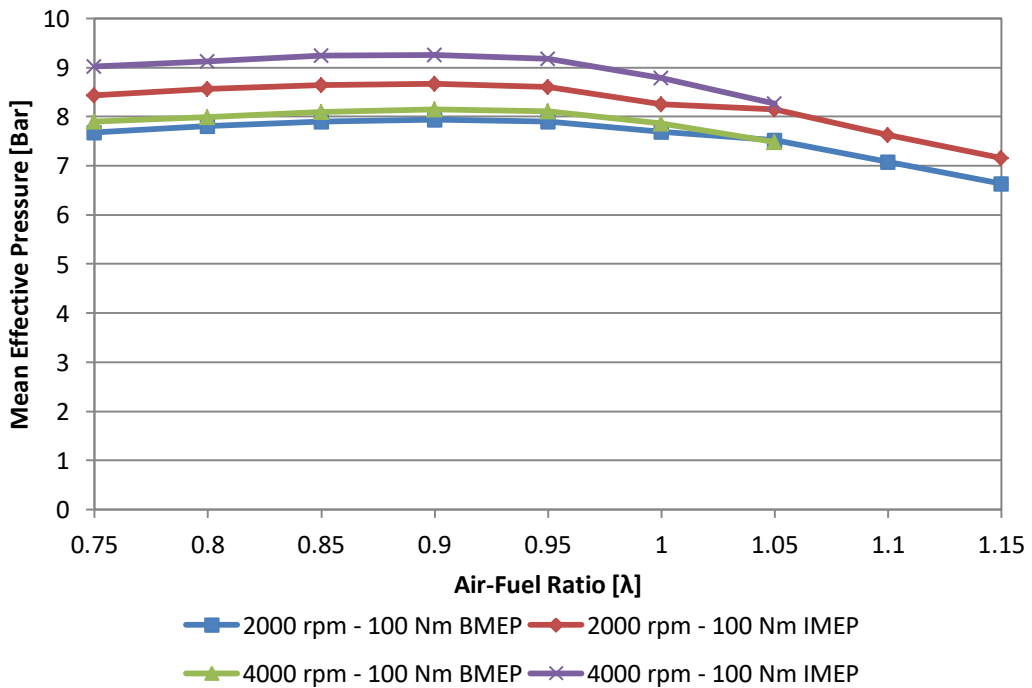

Figure 43: Mean Effective Pressure vs Air-Fuel Ratio (High Load)

64

Figure 44 (Blair, 1999) indicates a similar pattern to Figures 42 and 43, where excessive brake torque reduction occurs during lean combustion. The friction within the engine is estimated to remain constant; this is seen in Figure 45 where mechanical efficiency show little change with respect to air-fuel ratio. See section 4.3.2 for more information on mechanical efficiency.
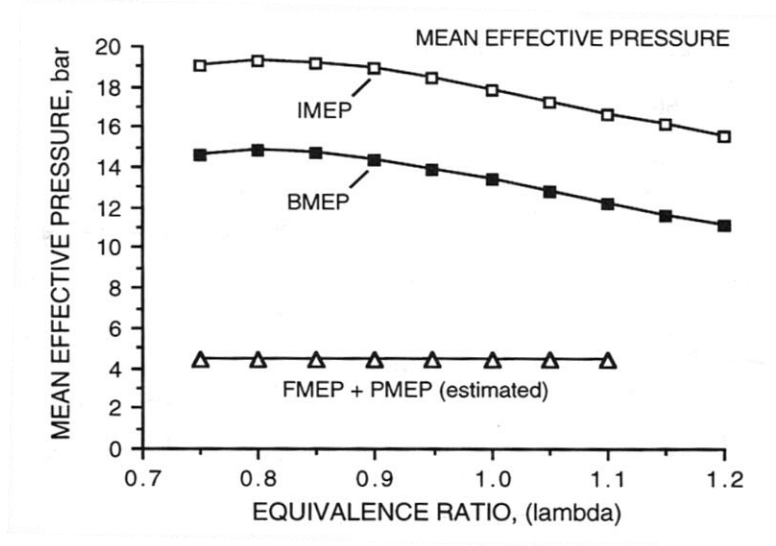

Figure 44: Effect of air-fuel ratio on mean effective pressure (Blair, 1999)
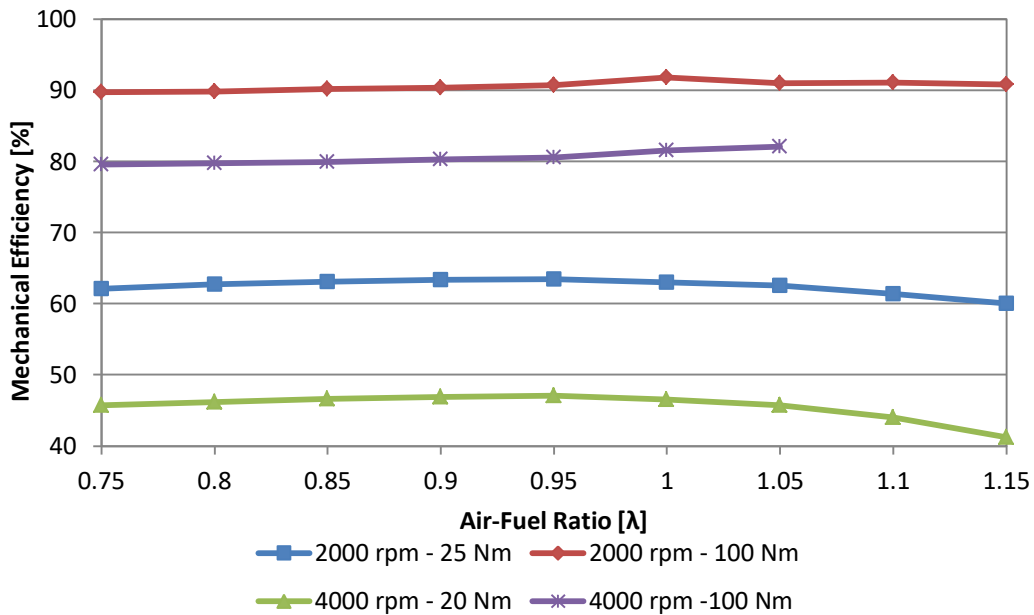

Figure 45: Mechanical Efficiency vs Air-Fuel Ratio

5. Modelling Results

The in-cylinder pressure data was used to model the heat-release within the combustion chamber, using both a single-zone and a two-zone model. Engine performance was further modelled using Lotus Engine Simulation in order to ascertain whether the software package could be used to predict engine parameters such as efficiency and exhaust gas temperature.

5.1 Single-Zone Heat-Release

The timing and fuelling swings performed (sections 4.3 and 4.4) were modelled for heat-release using a MATLAB written code as a means to see the effect of spark timing and air-fuel ratio on combustion. Engine speed was also varied to see the effect on combustion. The single-zone heat-release model assumes a control volume within the cylinder while the combustion is set to be a simple heat addition process. Pressure and temperature are assumed uniform within the cylinder (see section 2.6.1).

All single-zone heat-release curves were normalised at the end of combustion, estimated to be when the cumulative heat-release rate becomes negative after combustion (Stone, 2012). The heat-release is derived using the average in-cylinder pressure measurement for the recorded 100 consecutive cycles.

5.1.1 Spark-Ignition Timing Effects

With the engine running at 2000 rpm and 100 N·m, the effect of adjusting spark-ignition timing was observed in Figure 46 (air-fuel ratio kept constant at $\lambda = 1$). The most delayed spark-ignition timing (12° BTDC) leads to the slowest normalised heat-release curve due to lower burn rates. The 20° and 26° spark-ignition timing heat-release curves show the highest burn rates; these are similar to one another. This indicates that the effect of spark timing on the shape of the heat-release diminishes as the timing is advanced.

A Wiebe function (see section 2.6.4) was fitted to each curve, using simultaneous equations, and the values of a, m, and burn duration are shown in table 4. The advancement of spark-ignition timing increases the value of both the a and m constant, with burn duration remaining relatively constant.

Table 4: Wiebe function constants for single-zone heat-release curves (spark-ignition timing change)

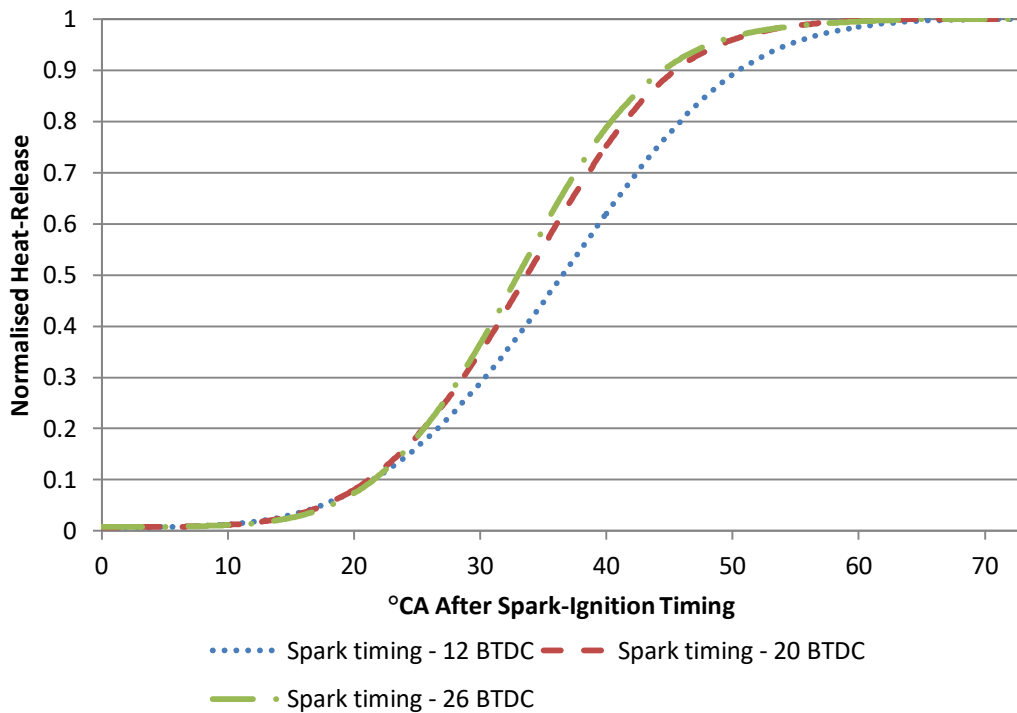| Spark Timing [°CA BTDC]	a	m	Burn Duration [°CA]
12	8.7	2.65	73
20	10.5	2.95	67
26	14.5	3.1	70

Figure 46: Effect of Spark-Ignition Timing on Normalised Heat-Release for Low Speed, High Load Conditions

The relationship between the cycle by cycle variations (shown as the coefficient of variation for $IMEP_{net}$) of combustion and the crankshaft angle, at which 50% of heat energy is released, can be seen in Figure 47. All test points were tested using a constant air-fuel ratio ($\lambda = 1$) with the spark-ignition timing being the only parameter changed. Each data point is an individual test with a different spark-ignition timing set for that test.

This can be seen that as the position of 50% heat-release is moved towards 5 - 10° ATDC, the COV for $IMEP_{gross}$ decreases. This indicates that more consistent combustion occurs as the average heat-release curve is advanced using spark-ignition timing.

As seen in section 4.3 the spark-ignition timing that resulted in the lowest COV for $IMEP_{gross}$ also resulted in the highest brake torque. The position of 50% heat-release that leads to maximum break torque occurs between 5 - 7° ATDC (Heywood, 2018).
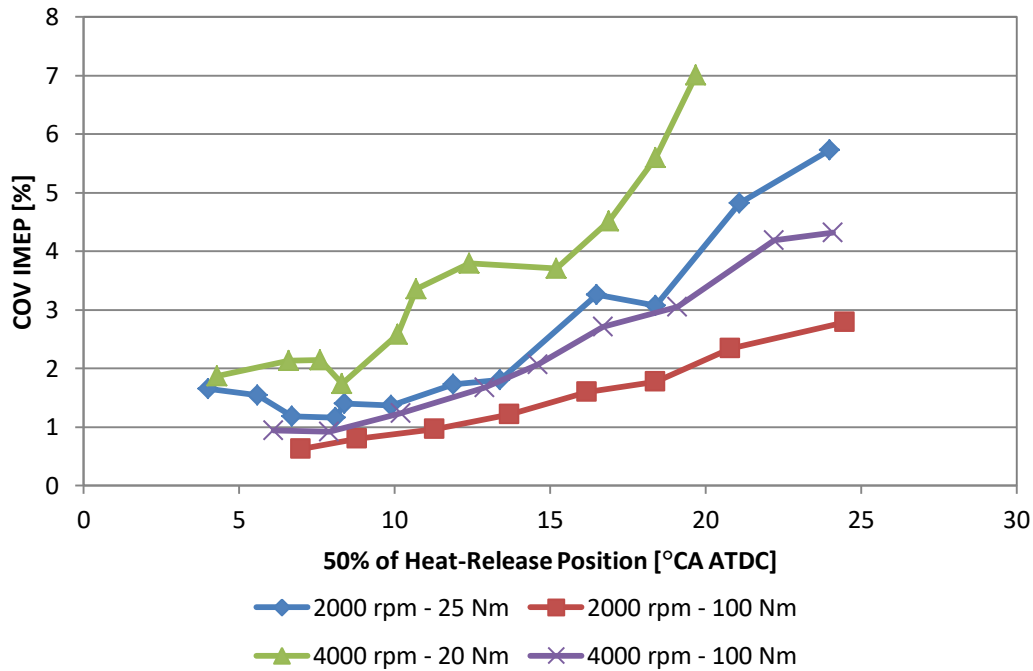
Figure 47: IMEP$_{COV}$ vs 50% of Heat-Release

Figures 48 and 49 show the gross IMEP$_{gross}$ as it relates to the 50% heat-release crankshaft angle position. Each data point represents a test point with its own spark-ignition timing.

Figures 48 and 49 corroborate Figure 47 by showing that the peak gross IMEP$_{gross}$ is found at 5 - 10° ATDC for the 50% heat-release position for all test conditions. This supports Figure 47 as the maximum brake torque coincides with the minimum COV for IMEP$_{gross}$, as seen in section 4.3.

These two figures are shown separately to highlight the scale, allowing the reader to see the effect of the 50% heat-release crankshaft angle position on the performance of the engine. It can also be seen that if the heat-release curve is advanced too far, where the 50% heat-release position occurs before 5 - 10° ATDC, the IMEP$_{gross}$ will start to decrease. This is seen in section 4.3 where over advanced spark-ignition timing increases the work done on the piston during compression, thus decreasing the work done on the piston during expansion.
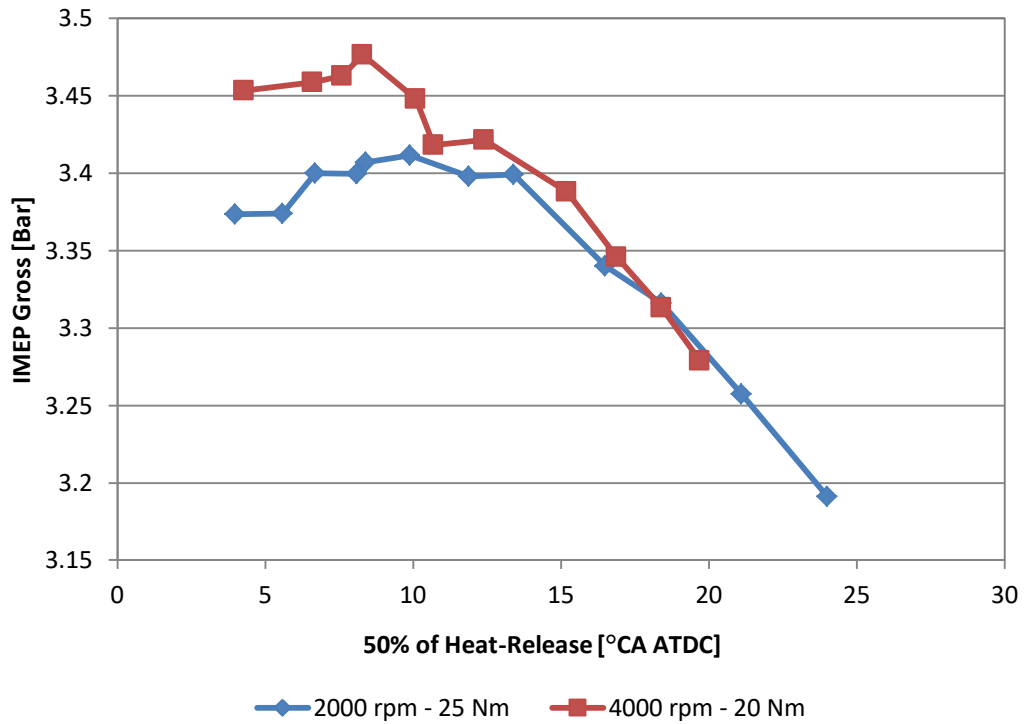
68

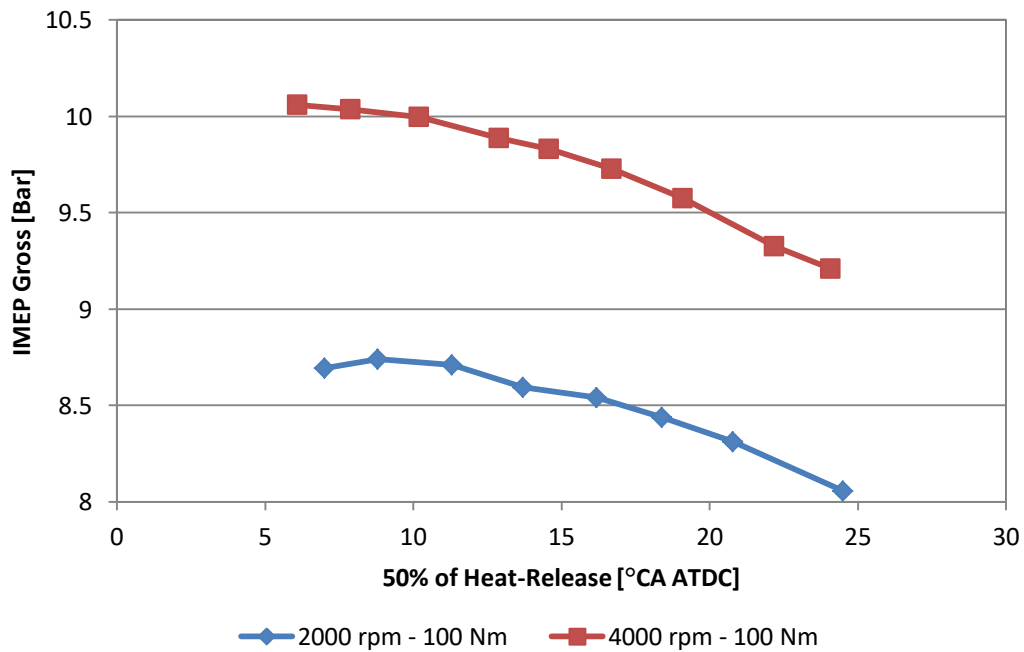**Figure 48: IMEP$_{gross}$ vs 50% of Heat-Release (Low load)**

Figure 49: IMEP$_{gross}$ vs 50% of Heat-Release (High load)

5.1.2 Air-Fuel Ratio Effects

The effect of changing the air-fuel ratio on the heat-release curve was investigated for an engine test condition of 2000 rpm and 100 N·m. The spark-ignition timing was kept constant at 16° BTDC. Figure 50 indicates that combustion leaner than stoichiometric results in a slower rate of heat-release as compared to stoichiometric or richer than stoichiometric combustion.

Figure 51 shows the same trends as Figure 50 where leaner combustion lead to slower heat-release, especially with regard to flame development (0 - 10% heat-release). The indolene fuel can be compared to petrol (gasoline) with regards to heat-release rates.

The laminar flame speed of a burning air-fuel mixture is directly proportional to the rate of burnt fuel mass and is therefore proportional to the rate of heat-release (Heywood, 2018:431). Higher temperatures also increase the reaction rate. As seen in Figure 52, the highest laminar flame speed for petrol (gasoline) occurs at a mixture slightly richer than stoichiometric. Figure 50 corroborates this by showing the highest burn rates for combustion mixtures richer than stoichiometric.

Table 5 shows the Wiebe function constants for the curves fitted to the heat-release, using simultaneous equations. The *a* and burn duration constants show an increase with air-fuel ratio while the *m* constant shows a decrease.

Table 5: Wiebe function constants for single-zone heat-release curves (air-fuel ratio change)

Air-Fuel Ratio [λ]	a	m	Burn Duration [°CA]
0.75	7.2	3	59
1	9.1	2.8	68
1.15	8.8	2.6	84

Figure 53 shows the relationship between the crankshaft angle position of 50% heat-release and IMEP$_{gross}$ (as seen in section 5.1.1) for two low load engine test conditions. Each test point indicates a different air-fuel ratio, with the highest air-fuel ratios resulting in lowest IMEP$_{gross}$ values (see section 4.4). As the air-fuel ratio is increased, IMEP$_{gross}$ increases until the 50% heat-release crankshaft position reaches a value of 5 - 10° ATDC. Further enrichment will then reduce the IMEP$_{gross}$ as well as delay the 50% heat-release crankshaft position. This is due to the excess fuel not burning completely and slowing the reaction rates (Figure 52). Slower heat-release will delay the heat-release curve, shifting the 50% heat-release position away from top dead centre.
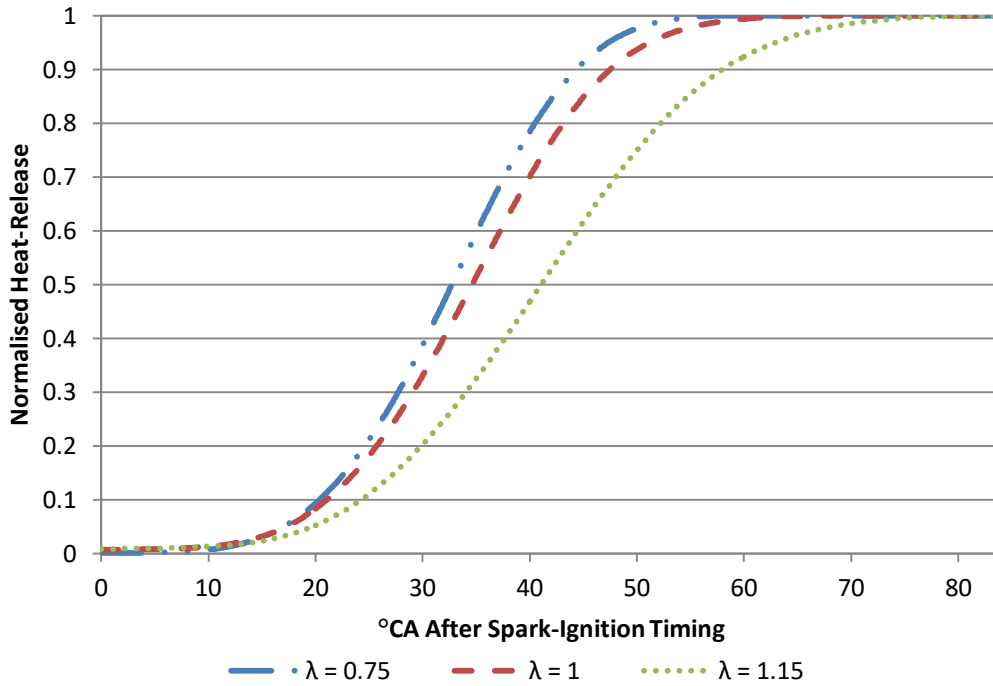
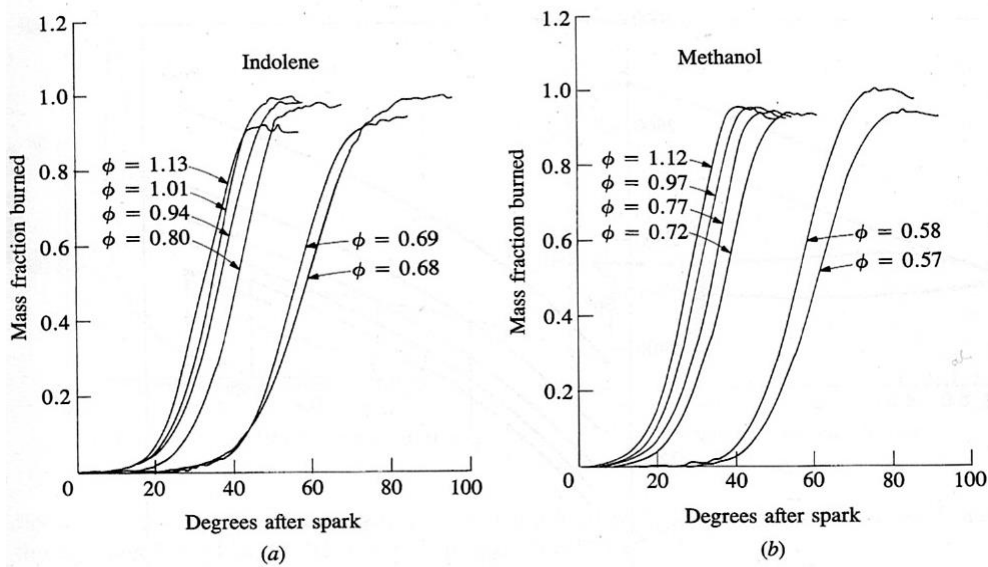**Figure 50: Effect of Air-Fuel Ratio on Normalised Heat-Release**

Figure 51: Mass fraction burned curves determined from measured cylinder pressure data using two-zone combustion model: (a) gasoline; (b) methanol. Φ = fuel/air equivalence ratio (Heywood, 2018)
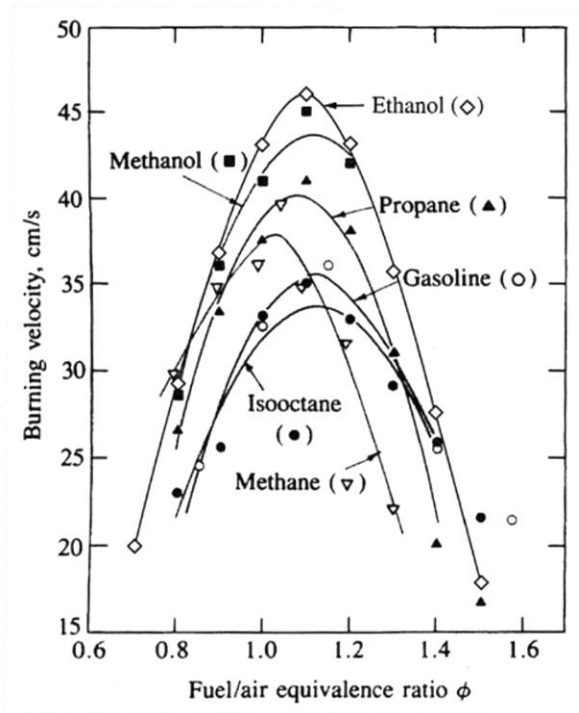
Figure 52: Laminar burning velocity for several fuels as a function of fuel/air equivalence ratio, at 1 atm and 300 K. Lines are least-squares polynomial fits to data. (Heywood, 2018)
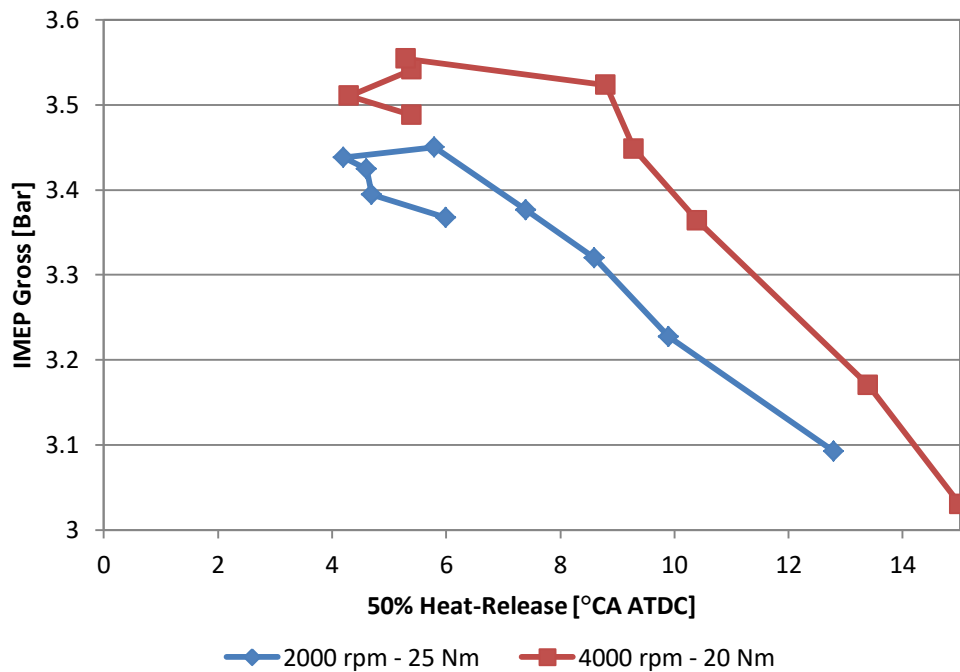

Figure 53: IMEP$_{gross}$ vs 50% of Heat-Release (Low Load)

72

5.1.3 Engine Speed Effects

Figure 54 shows the combustion duration of the heat-release for various engine speeds. All tests were performed at 100 N·m with OEM spark-ignition timing.

As engine speed increases, the time period during which combustion can occur decreases. If combustion rates remain constant, an increase in engine speed would result in a proportional increase in crankshaft angle degrees for combustion duration. Figure 54, however, shows only slight increases in crankshaft angle combustion durations with engine speed increases. A 2.25 factor increase in the value of engine speed only resulted in 1.27 factor increase in crankshaft angle burn duration for 0 - 10% heat-release. This is due to the turbulence of the air-fuel mixture increasing with engine speed.

Turbulence is generated as a result of induction and compression processes (Stone, 2012) alongside combustion chamber design. Figure 55 (Heywood, 2018) shows the gradual increase in combustion duration with engine speed.
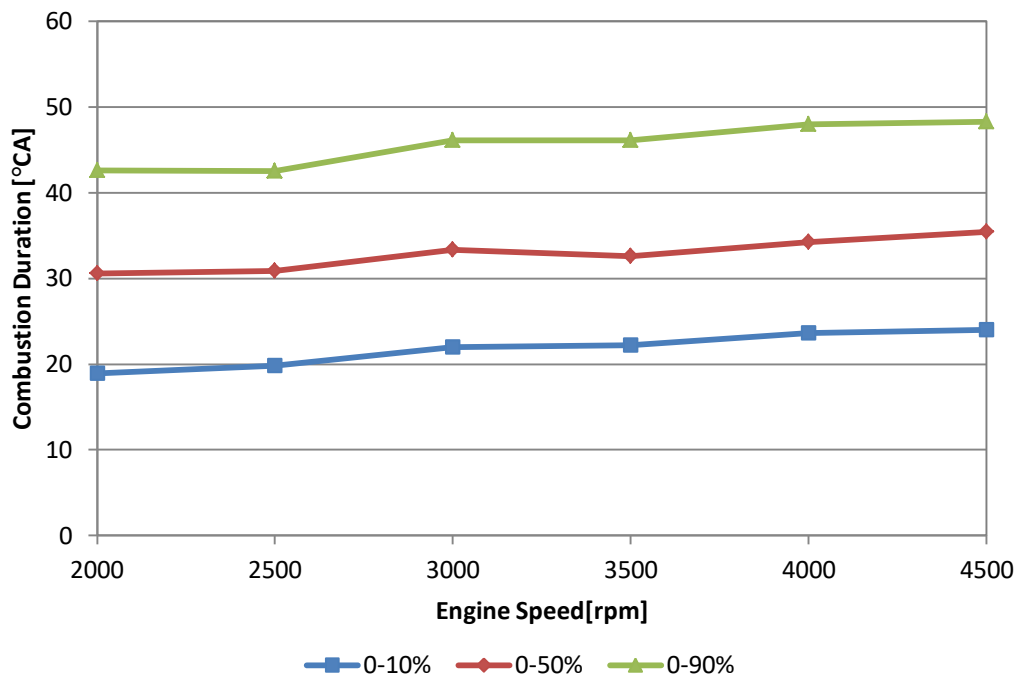

Figure 54: Combustion Duration vs Engine Speed for 100 Nm at Various Engine Speeds
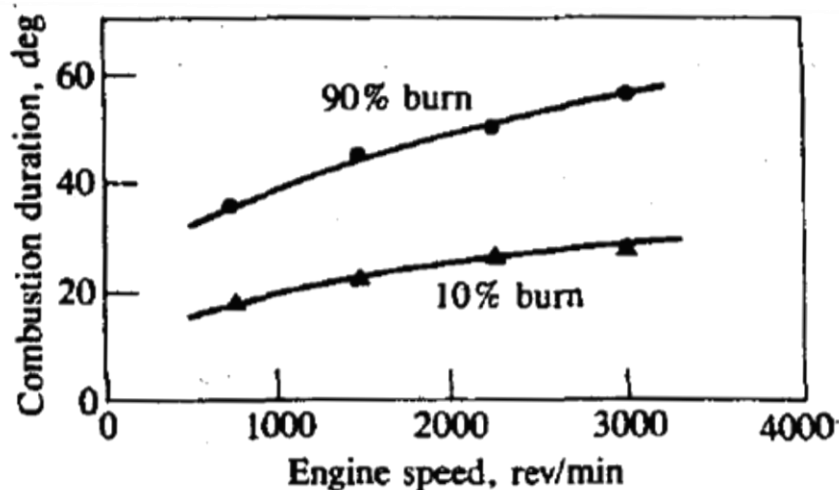
Figure 55: Effect of engine speed on flame development angle (0 to 10% burned) and overall burning angle (0 to 90% burned), φ = 1.0, intake pressure = 0.54 atm, spark - 30° BTC (Heywood, 2018)

5.2 Two-Zone Model Comparison

The two-zone mass fraction burnt model discussed in section 2.6.2 was used alongside the single-zone heat-release model discussed in section 2.6.1. Both heat release models were written in MATLAB code. Figure 56 shows a comparison between the single-zone heat-release model and the two-zone mass fraction burnt model for an engine test condition of 2000 rpm and 100 N·m.

The single-zone cumulative heat-release (which is in units of energy) was converted to a fuel mass equivalent using the lower heating value of petrol. This allowed for a direct comparison.

The two-zone model shows a higher equivalent energy release compared to the single-zone model as it specifically shows the mass of fuel being burnt. Unreleased fuel chemical energy in the form of carbon monoxide and diatomic hydrogen makes up the difference as compared to the heat-release model. It is also the result of combustion inefficiency (Chun & Heywood, 1987).

Appendix G shows the numerical differences in crankshaft angle degrees of different combustion durations for the single-zone and two-zone models. The largest differences start to show later in combustion as this is the period of combustion where the most carbon monoxide and hydrogen by-products form. Figure 57 shows the difference between the mass-fraction burnt and the normalised heat-release (Chun & Heywood, 1987).
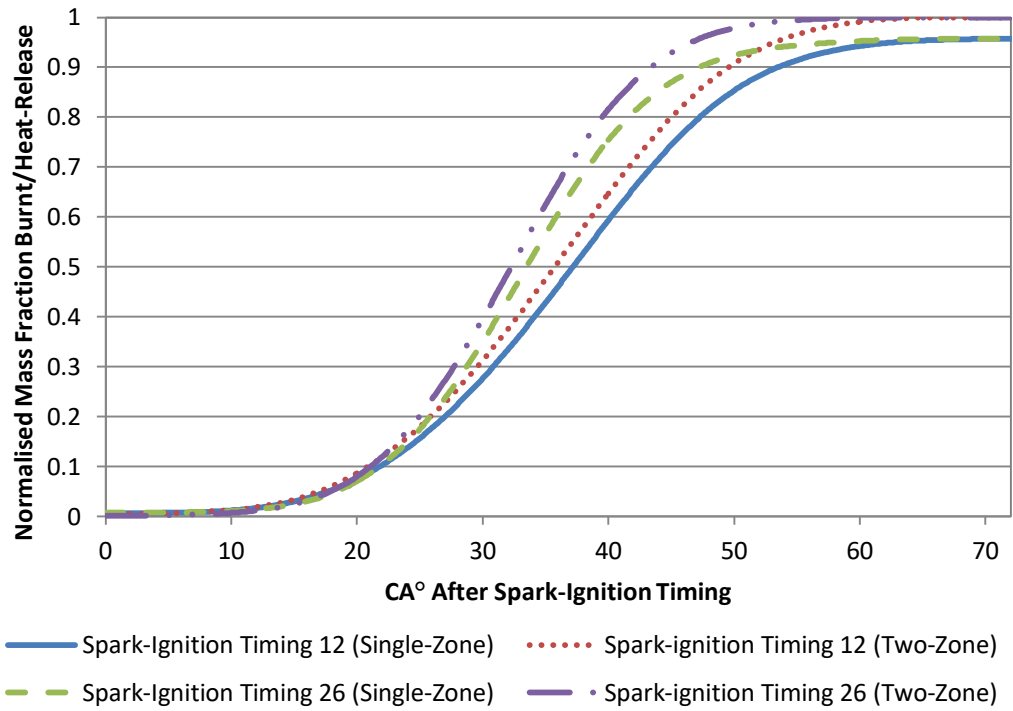
Figure 56: Single-Zone and Two-Zone Model Comparison (Low speed, high load)
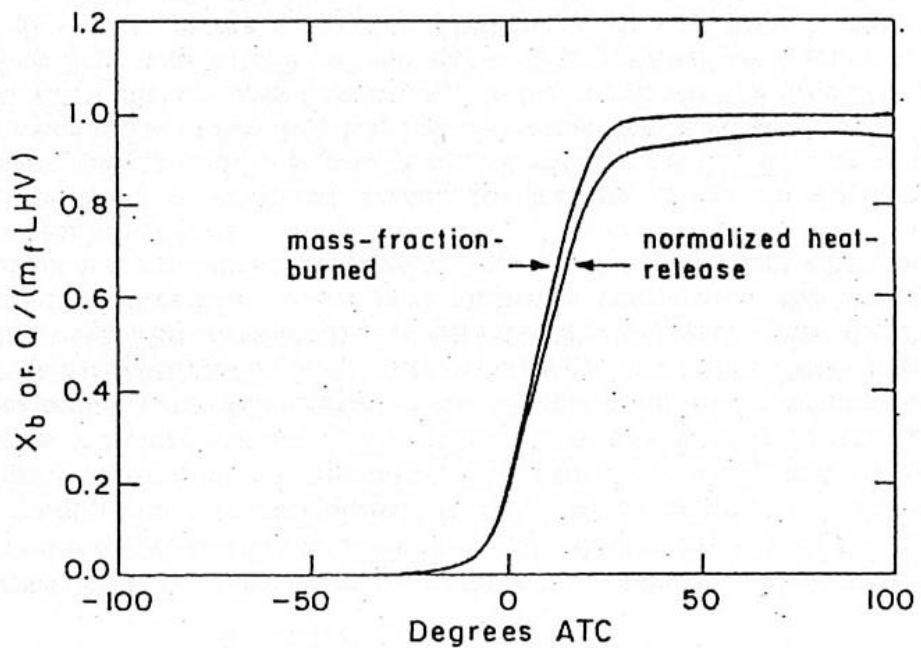

Figure 57: The mass-fraction-burned and normalized heat-release for a cycle with φ=1.0 (λ = 1) at 1500 rev/min, calculated from one-zone analysis with appropriate ratio of specific heats values. (Chun & Heywood, 1987)

5.3 Lotus Engine Simulation

Lotus Engine Simulation (LES) was used to simulate engine performance parameters. This commercial package software requires heat release as an input for accurate engine performance modelling. The single-zone heat release curves obtained in section 5.1 were used as inputs along with other engine parameters. The software uses a single-zone, zero-dimensional heat-release model for combustion alongside a one-dimensional, pipe flow model. The single-zone heat-release Wiebe function parameters obtained in section 5.1 were used as an input alongside other parameters such as engine speed, brake torque, mechanical efficiency, and atmospheric conditions.

Other more general parameters such as physical geometries and fuel properties are used as inputs as well. Intake and exhaust pipe properties are specified by length, diameter, material, and wall thickness. The Woschni heat loss model was chosen as this was used in the single-zone heat-release.

5.3.1 Full Load

The experimental full load results (section 4.2.3) were modelled in LES and the BSFC and exhaust gas temperatures were recorded. Figure 58 shows how the same trends that were seen in the experimental results are seen in the simulation results. The modelled exhaust gas temperatures were higher than the experimental temperatures while the modelled BSFC was slightly lower than the experimental results.
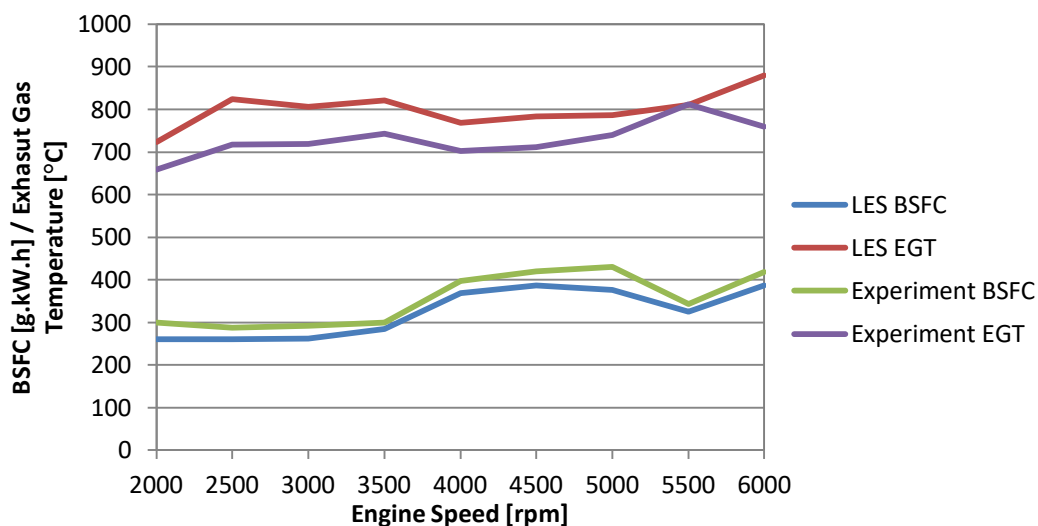

Figure 58: Brake Specific Fuel Consumption and Exhaust Gas Temperature vs Engine Speed (Lotus Engine Simulation vs Experimental)

76

The lower BSFC values for the LES software indicate a lower fuel mass flow rate than the experiment as power output was equal. The difference could be a result of the friction model used in LES. The experimentally measured IMEP and BMEP values were used to calculate FMEP. This value was used in the LES friction model. Errors in IMEP measurement could lead to errors in the FMEP values which would manifest as a more or less efficient engine (affecting BSFC values).

5.3.2 Spark-Ignition Timing Adjustment

The timing swings (Table 6) modelled in LES correspond to the experimental results, with exception only for the exhaust gas temperatures at low speed, low load conditions. All other results were within 10%.

Table 6: LES vs Experimental (Timing Swing)

Engine Speed [rpm]	Torque [N.m]	Spark Timing [°CA]	LES		Experiment		Difference [%]	
			BSFC [g/kW.h]	EGT [°C]	BSFC [g/kW.h]	EGT [°C]	BSFC [g/kW.h]	EGT [°C]
2000	25	22	409.47	695.23	431.92	438.84	5.20	-58.42
		44	367.05	617.32	396.79	402.45	7.50	-53.39
	100	12	266.87	702.78	269.38	647.76	0.93	-8.49
		26	241.56	624.28	249.62	596.15	3.23	-4.72
4000	20	30	507.93	613.86	526.88	598.60	3.60	-2.55
		50	466.06	576.43	488.05	573.32	4.51	-0.54
	100	16	296.79	835.34	290.57	844.59	-2.14	1.10
		32	261.08	732.87	263.19	773.95	0.80	5.31

5.3.3 Air-Fuel Ratio Adjustment

Table 7 shows the LES modelled fuelling swing results as compared to the experimental results. With regard to BSFC, the results compare favourably as they are within 12%. The exhaust gas temperatures, however, vary considerably with low speed, low load conditions (as with the timing swing) being up to 59% than the measured value.

The difference between the low speed, low load exhaust gas temperatures could be attributed to the exhaust pipe heat loss model selected in LES. The heat loss was modelled as a simple air-cooled iron thin-walled pipe with only convective heat transfer to the environment. At the high temperatures that the exhaust gas

reaches, the heat loss through radiation becomes very significant. This heat loss was not modelled in LES and would thus result in lower than expected heat transfer and higher than expected exhaust gas temperatures.

At low speed, low load test conditions, exhaust gas velocities are at their lowest. This reduces the Reynolds number of the flow and can reduce the convective heat transfer used in the one-dimensional pipe flow model used in LES.

Table 7 LES vs Experimental (Fuelling Swing)

Engine Speed [rpm]	Torque [N.m]	Air-Fuel Ratio [λ]	LES		Experiment		Difference [%]	
			BSFC [g/kW.h]	EGT [°C]	BSFC [g/kW.h]	EGT [°C]	BSFC [g/kW.h]	EGT [°C]
2000	20	0.75	480.19	586.50	545.31	369.10	11.94	-58.90
		1	357.98	629.92	389.20	399.47	8.02	-57.69
		1.15	377.28	599.13	398.20	398.90	5.25	-50.20
	100	0.75	348.42	620.87	368.02	537.45	5.33	-15.52
		1	256.61	650.19	258.64	624.11	0.78	-4.18
		1.15	266.38	690.76	263.66	613.24	-1.03	-12.64
4000	20	0.75	637.02	432.36	672.02	507.35	5.21	14.78
		1	462.03	581.64	481.80	574.30	4.10	-1.28
		1.15	530.82	579.85	539.82	566.20	1.67	-2.41
	100	0.75	402.93	609.15	385.91	669.04	-4.41	8.95
		1	271.86	783.82	271.10	806.28	-0.28	2.79

6. Conclusions

The engine test facility was refurbished and upgraded with new equipment, including a new personal computer for control software, a new PLC for engine test control, and additional measurement equipment such as thermocouples and an air-mass flow meter. The engine pistons and valves were inspected, the clutch was replaced, and an oil change was performed to re-commission the engine test bench to working order.

In-cylinder pressure indicating equipment in the form of a spark plug pressure transducer produced by Kistler was installed along with a charge amplifier and Labview software. This allowed for in-cylinder pressure measurement used for combustion modelling.

Engine testing was then performed using the OEM ECU in order to characterise the engine performance and to record baseline spark-ignition timing and baseline air-fuel ratio programmed onto the OEM ECU. The engine was found to be running within design specifications with the OEM air-fuel ratio control, protecting the engine at high power conditions with fuel enrichment.

The OEM ECU was then replaced with an aftermarket ECU in order to allow for spark-ignition adjustment and air-fuel ratio adjustment. The baseline data recorded from the OEM ECU was used to program the aftermarket ECU safely.

The engine was tested using the aftermarket ECU by adjusting the spark-ignition timing and air-fuel ratio. The influences of these changes on peak in-cylinder pressure, coefficient of variation for IMEP, mean effective pressures, exhaust gas temperatures, and brake specific fuel consumption were also tested. It was found that peak engine performance was reached at maximum brake torque spark-ignition timing. Highest total engine efficiency was reached with a slightly lean air-fuel ratio mixture. The cycle by cycle variations for IMEP were reduced when a more rich combustion or advanced spark-ignition timing was used.

The effect of spark-ignition timing and air-fuel ratio on the combustion was also modelled using the in-cylinder pressure and a single-zone heat-release model. It was found that when the crankshaft angle position of 50% heat-release occurs at 5 - 10° ATDC, peak IMEP and minimal COV for IMEP was reached. A two-zone model was also implemented in order to compare to the single-zone model. It was found that the largest variation in heat-release / mass fraction burnt occurred later in combustion. The two-zone model was deemed unnecessary for the combustion modelling.

Engine test data recorded with the aftermarket ECU as well as the heat-release data modelled in MATLAB was then used as inputs for Lotus Engine Simulation (LES) software. It was found that the software provided brake specific fuel

consumption values within 12% of the measured experimental data. Exhaust gas temperature values provided LES were found to be up to 58% too high relative to the experimental data for low speed, low load conditions. This was due to the one-dimensional heat loss modelling selected in the software. Higher engine speeds and engine load provide exhaust gas temperatures within 16% of experimental data.

LES was determined to be useful for simulating engine with confidence, with exception of the exhaust gas temperatures at low power operating conditions.

Future work that can be done in this engine test facility may include:

- An increased range of spark-ignition timing and air-fuel ratio adjustments to investigate excessively rich/lean combustion or excessively advanced/retarded spark-ignition timing.
- The installation of an external oil cooler to reduce oil sump temperatures during high power test conditions.
- Combustion modelling of different fuel blends.
- The installation of emissions analysis equipment and the investigation of spark-ignition timing and air-fuel ratio on exhaust emissions.
- An investigation into the sensitivity of LES to changing physical parameters of the engine.

APPENDIX A: Internal Combustion Engine

A.1: Engine Specifications

The internal combustion engine used in the project had to be defined within numerous parameters for the engine modelling. Cylinder volumes and distances were needed for modelling the physical motion of the piston as cylinder volume changes as a function of the engine rotation.

Table A. 1: Engine Specifications

Engine Parameter	Value
Bore	82.07 mm
Stroke	75.48 mm
Connecting Rod Length	128.2 mm
Inlet Valve Throat Diameter	37 mm
Outlet Valve Throat Diameter	30 mm
Displaced Volume	0.001597 m^3
Clearance Volume	0.00004647 m^3
Compression Ratio	9.5
Intake Valve Opening	12° BTDC
Intake Valve Closing	24° ABDC
Exhaust Valve Opening	24° BBDC
Exhaust Valve Closing	12° ATDC
Intake/Exhaust Valve Lift	9.74 mm
Maximum Torque	137 N·m @ 2500 rpm
Maximum Power	70 kW @ 5500 rpm

A.2: Engine Service

The clutch in the engine was replaced due to the original clutch having a loose centre spline connection to the friction plate. The driveshaft was first disconnected before the gearbox housing removed in order to access the flywheel. Once replaced, the new clutch was aligned to prevent the same issue from recurring. The pressure plate was replaced as well due to the clutch disc and pressure plate being bought as a set.

APPENDIX B: Dynamometer

The eddy current dynamometer used in the project is a *Schenck* W150.
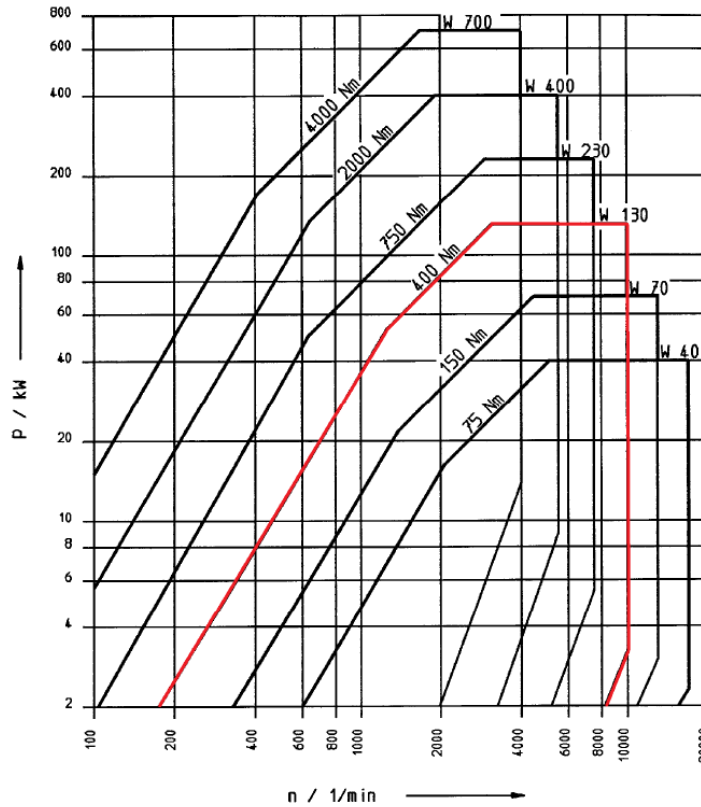
Figure B. 1: Speed vs Torque Curve for Eddy Current Dynamometer (Schenck Pegasus GmbH, 1997)

Table B. 1: Schenck W150 Eddy Current Dynamometer Specifications (Schenck Pegasus GmbH, 1997)

Torque	400 N·m
Max Speed	10000 rpm
Nominal power	130 kW
Weight	270 Kg

83

An original dynamometer was installed in the test cell at the beginning of this study. It was discovered that the rotor spinning in this dynamometer had bearing seats that were not properly aligned with one another. This led to excessive bearing noise and possible bearing wear that prevented the rotor from being spun faster than 3000 rpm. This dynamometer was disassembled, the bearings replaced, and the rotor rebalanced.

An eddy current dynamometer was also rebuilt with its rotor rebalanced and new bearings installed. It was found that this dynamometer performed better that the original dynamometer and a swap was done to install the second eddy current dynamometer.

APPENDIX C: Wiring Diagram

The figures shown in this appendix relate to the installation and setup of the PLC, 24 V power supply, control modules used in the 19 inch cabinet and the DAQ used for pressure indicating.
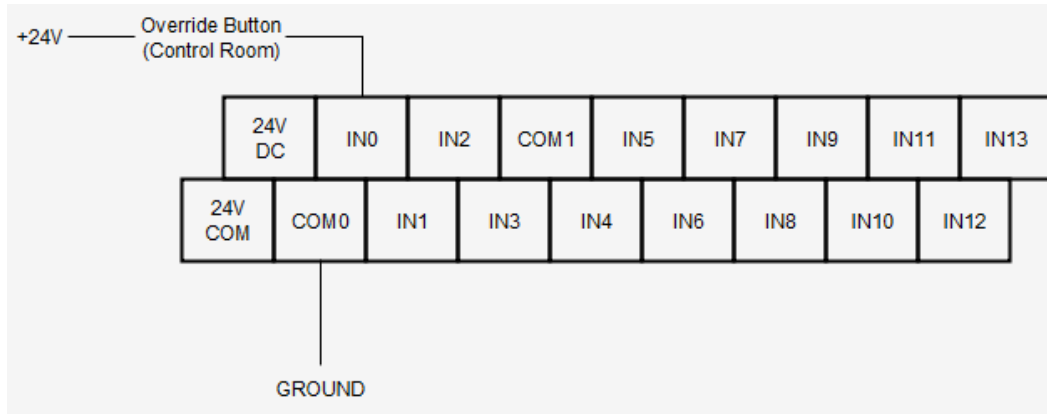
Figure C. 1: PLC Digital Inputs
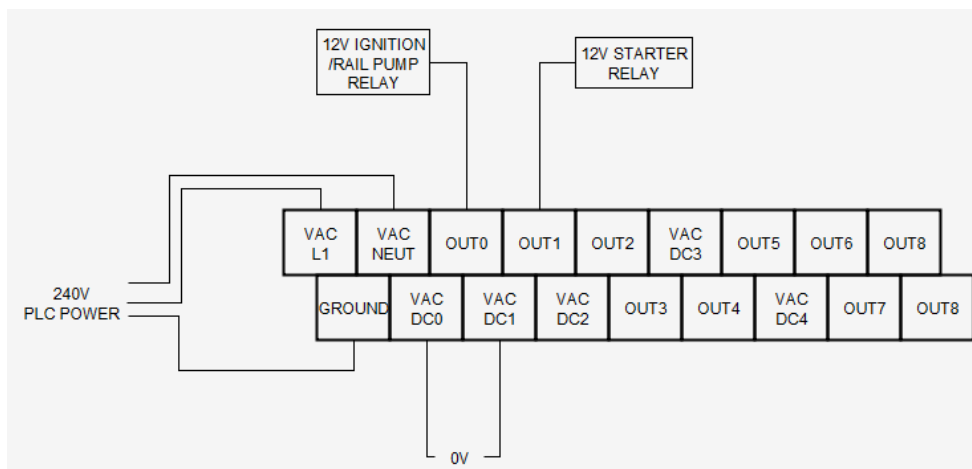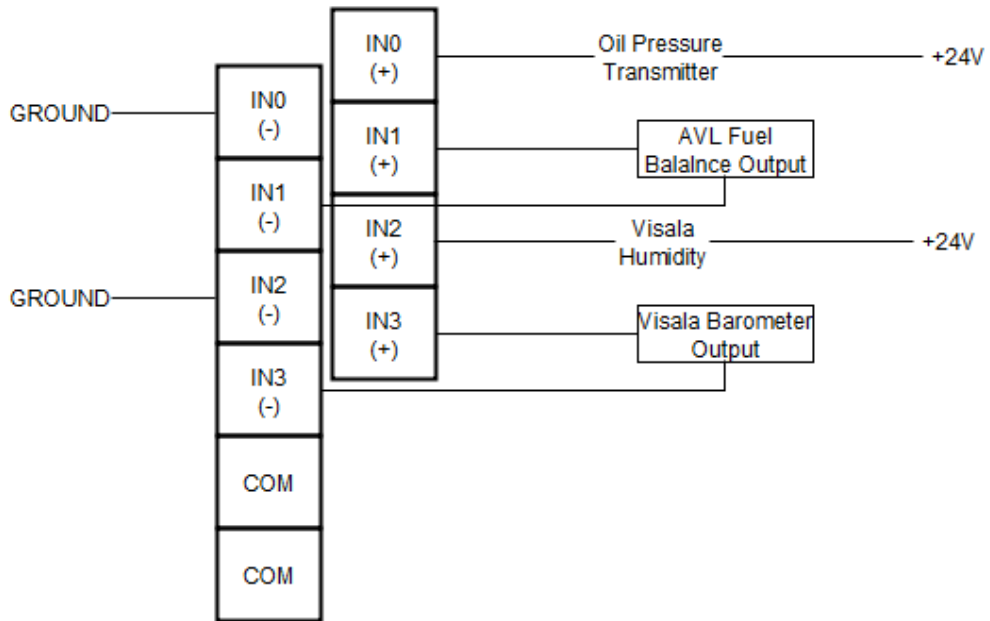
Figure C. 2: PLC Relays
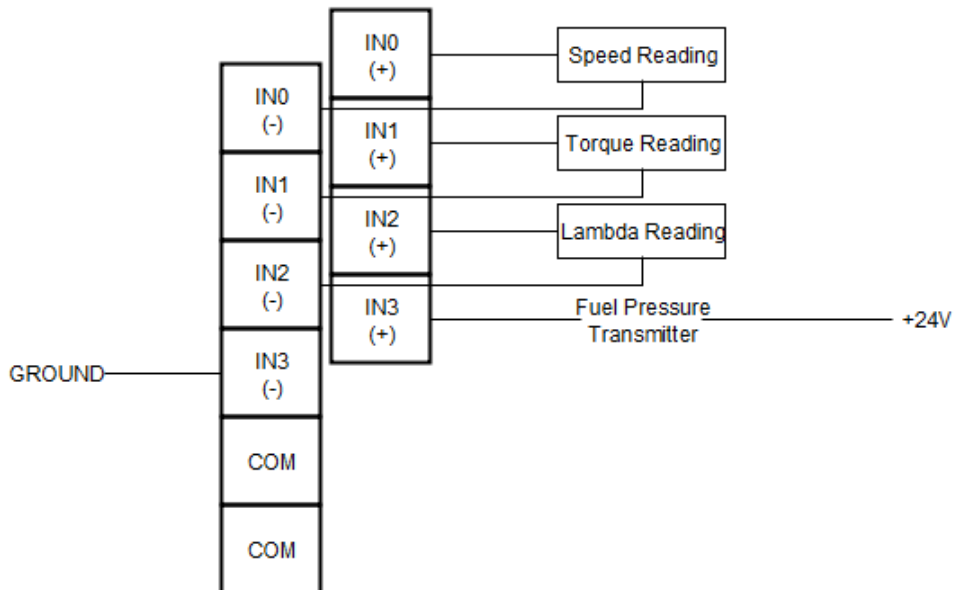
Figure C. 3: Analogue Input 1
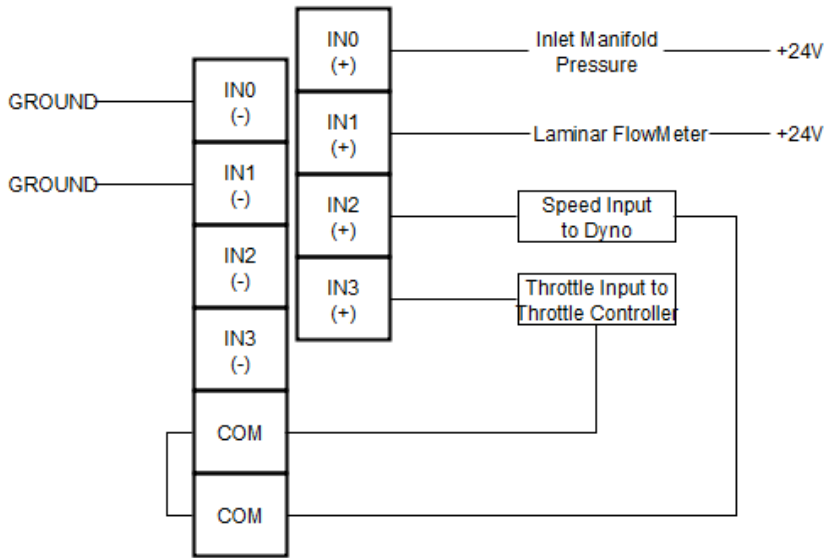

Figure C. 4: Analogue Input 2

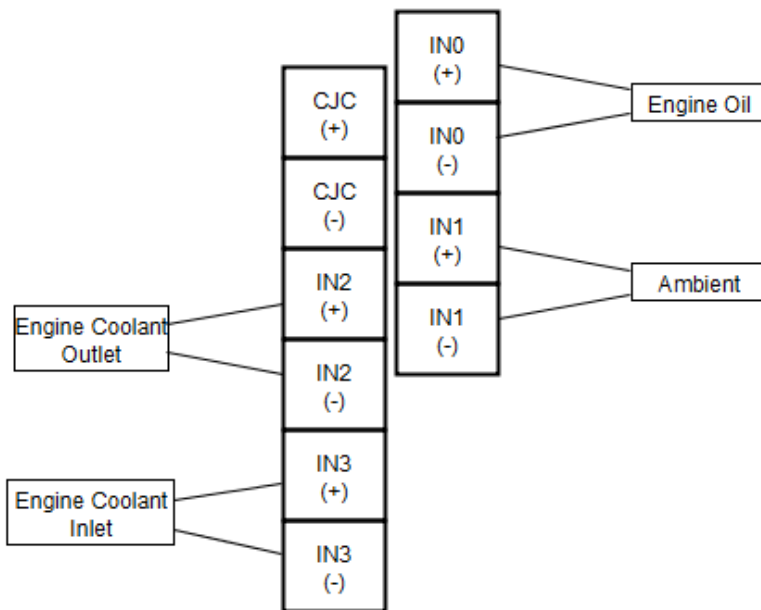**Figure C. 5: Combo Module (Analogue Input/Output)**
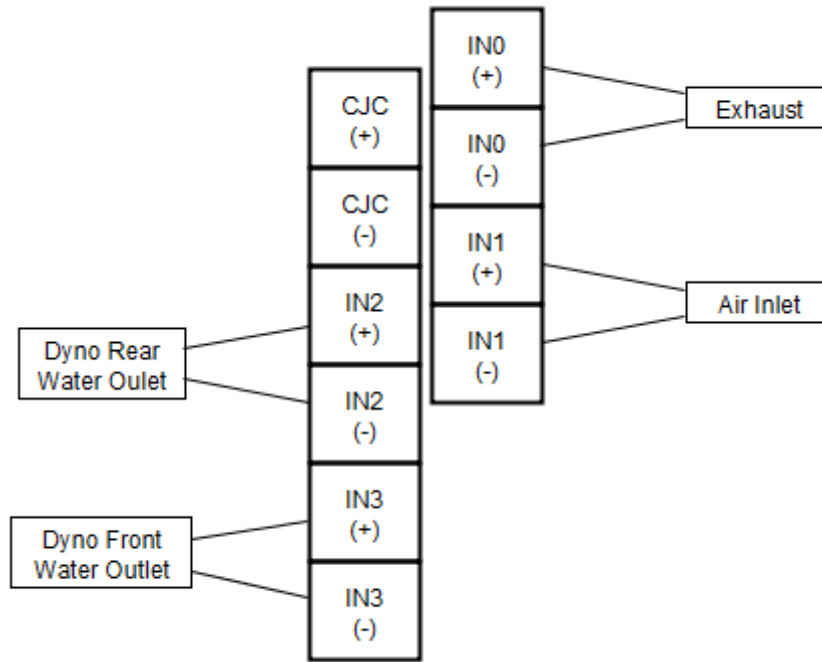
Figure C. 6: Thermocouple Input 1

87

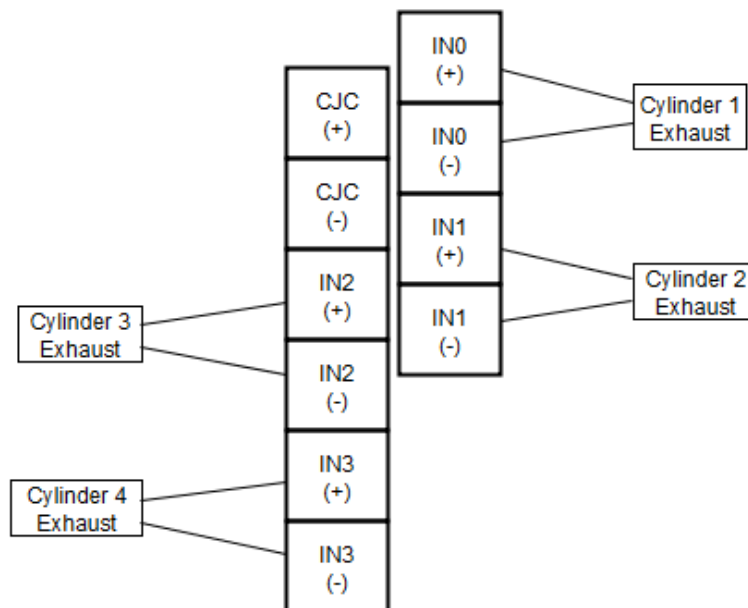**Figure C. 7: Thermocouple Input 2**

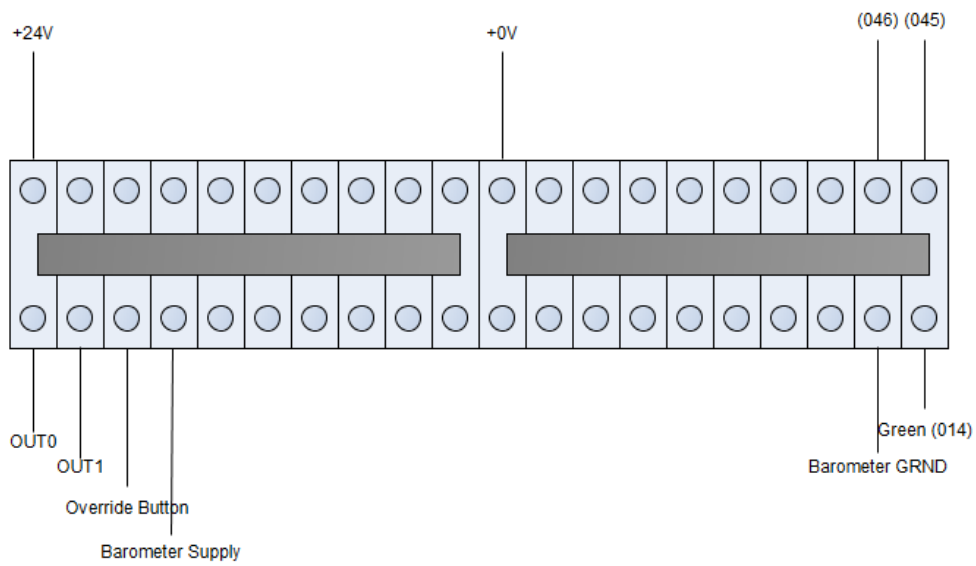**Figure C. 8: Thermocouple Input 3**

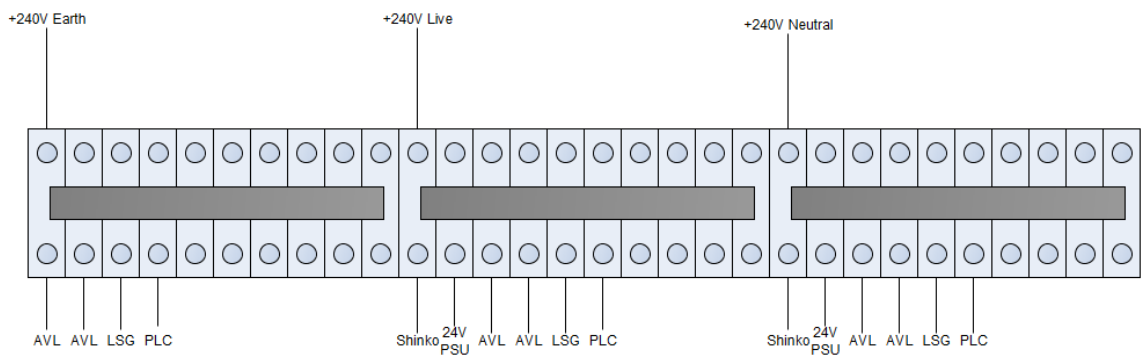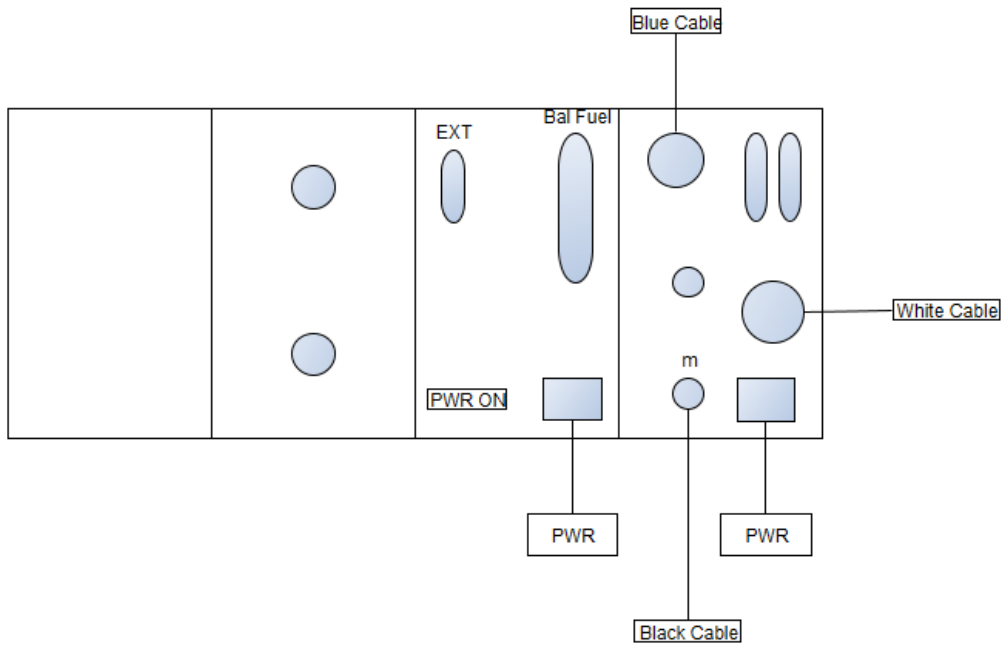**Figure C. 9: 24 V Rail**

Figure C. 10: 240 V Rail

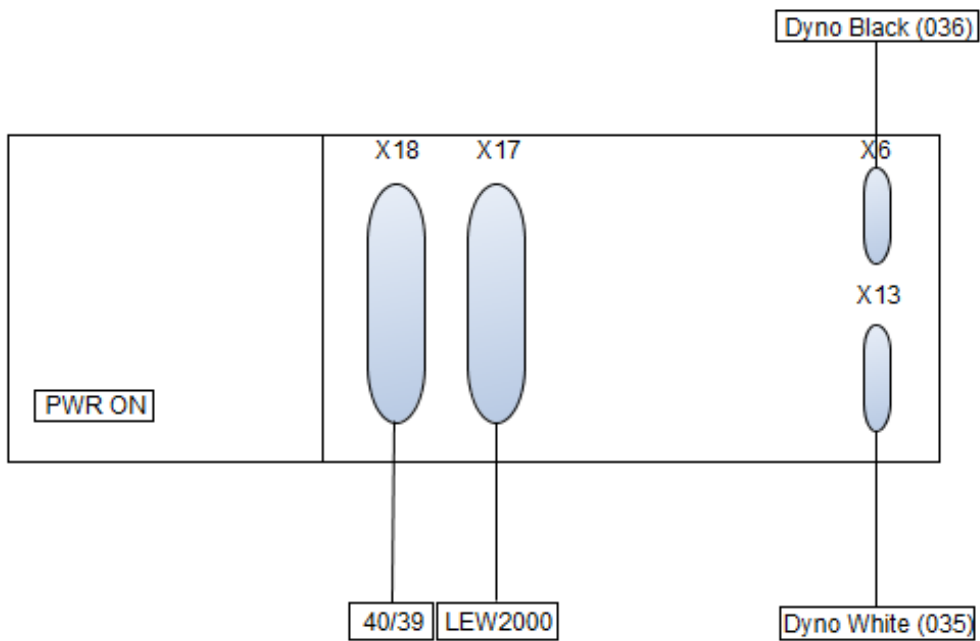**Figure C. 11: AVL Control Module**

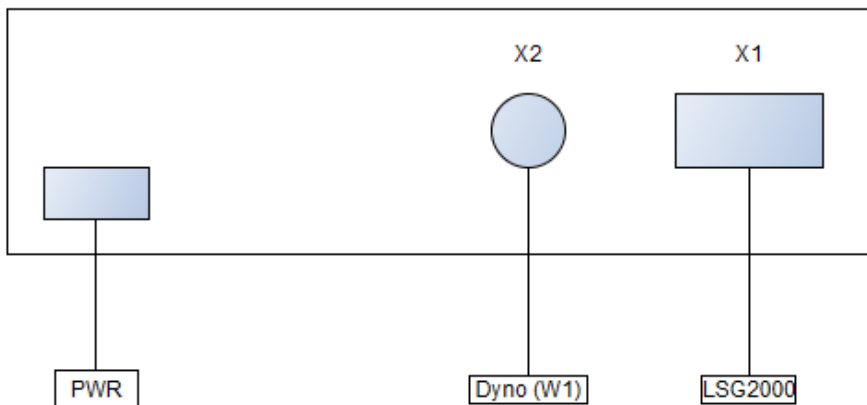**Figure C. 12: Schenck LSG2000**
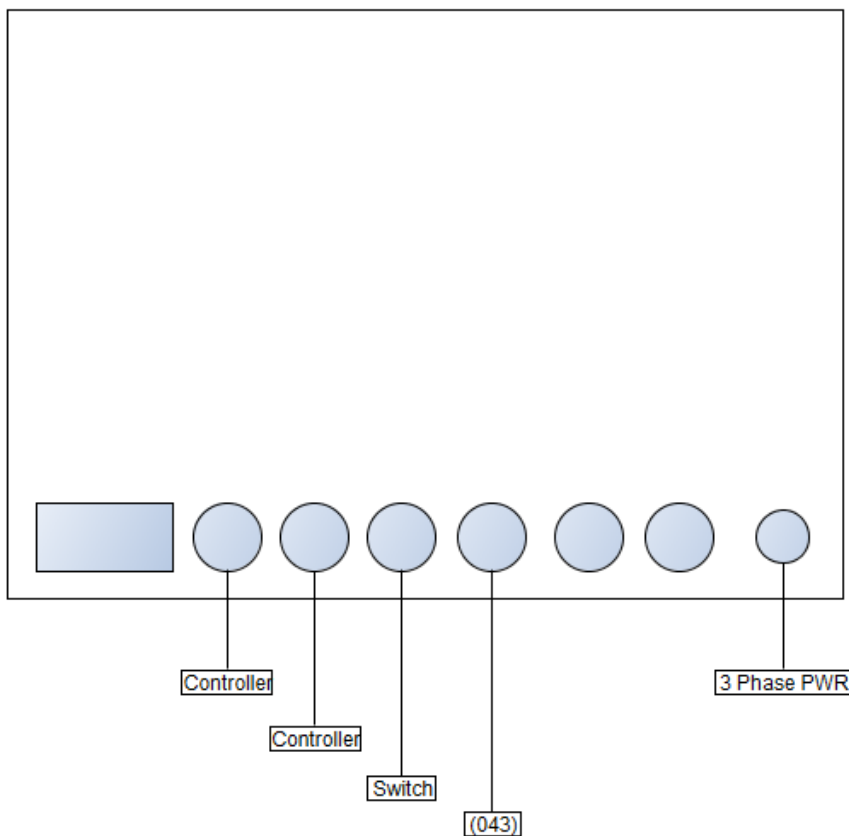
Figure C. 13: Schenck LEW2000

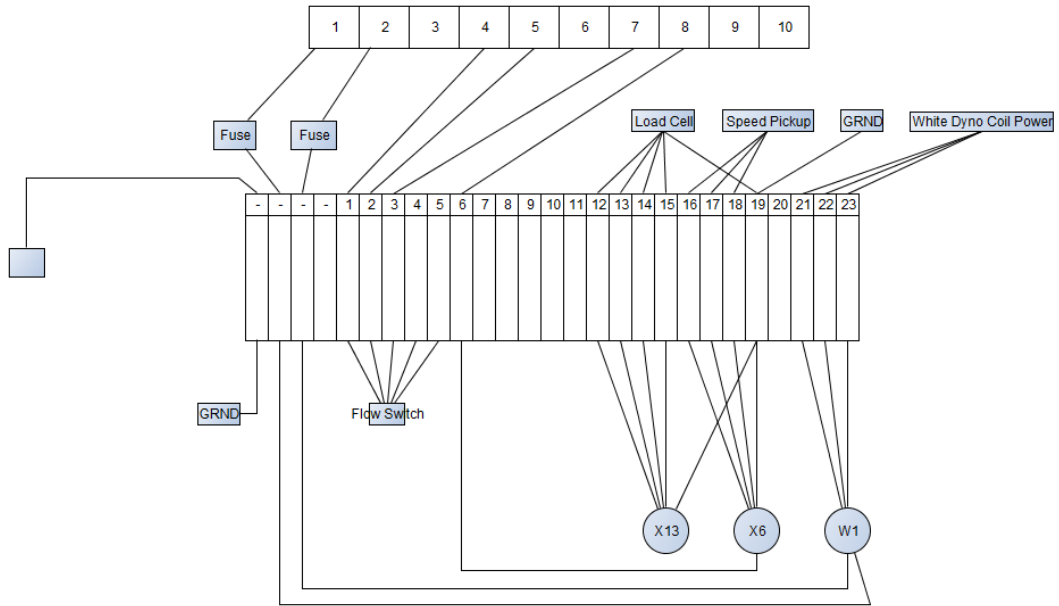**Figure C. 14: Throttle Actuator Controller**

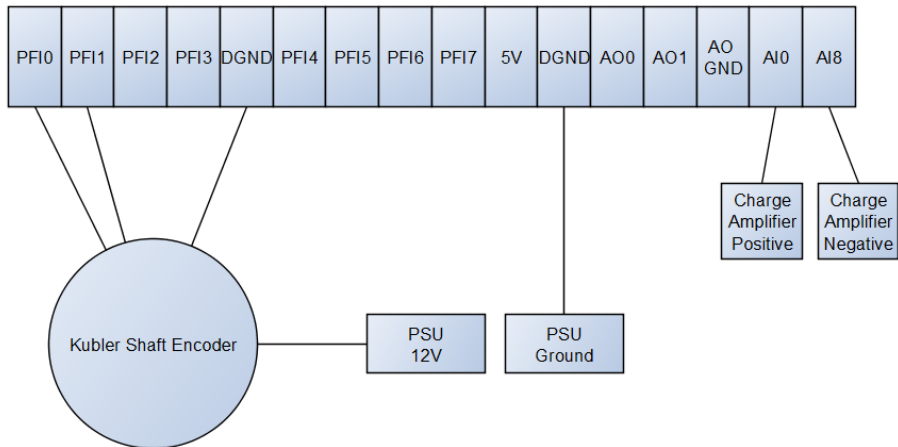**Figure C. 15: Dynamometer Safety Circuit**

Figure C. 16: Pressure Indicating Wiring for DAQ

APPENDIX D: Calibration

In this appendix the calibration of the equipment will be discussed. The equipment includes thermocouples, in-cylinder pressure measurement, and air volumetric flow measurement.

D.1: Meriam Laminar Air Flow Meter

The Meriam laminar air flow meter was used to measure the air flow through the internal combustion engine. It relies on the Hagen-Poiseuille law which states that:

$$\Delta P = \frac{8\mu L Q}{\pi R^4} \qquad \qquad \text{(D1)}$$

Equation D1 shows that there should be a linear relationship between the pressure drop across the laminar channels ΔP and the volumetric flow rate Q (Pfitzner, 1976).

The air flow sensor was calibrated by connecting the intake to a wind tunnel of known mass flow calibrations. A pressure differential meter was used to measure the pressure drop across the laminar flow elements. The fan that sucked air through the wind tunnel was operated at set speeds and the appropriate pressure drops were recorded to later be converted to the mass flow through the wind tunnel. The voltage readings produced by the pressure differential meter were recorded along with the mass flow. This allowed the voltage drop across the pressure differential meter to be correlated to the mass flow through the air flow sensor.

The wind tunnel used to calibrate the air flow sensor was located in the laboratory of Mechanical and Mechatronic Engineering, Stellenbosch University. The pressure drops across various bell mouth channels of known sizes could be correlated to a mass flow through the wind tunnel (Kröger, 2004).

An initial calibration was done on the flow sensor, but it was found to be inaccurate due to leakage during the calibration process. A leak test was done by blocking the intake of the air flow sensor. This would result in only leaked air moving through the wind tunnel. These mass flow rates were calculated and later subtracted from the calibration mass flow rates in order to get the real air flow through the air flow sensor.

Figure D.1 illustrates the relationship between the volumetric air flow rate and the voltage produced by the ΔP transducer. The analogue input expansion modules connected to the *MicroLogix 1200* PLC digitize a DC voltage ranging from 0 V to 10.5 V into a RAW value ranging from 0 to 32760 (Allen-Bradley, 2015).
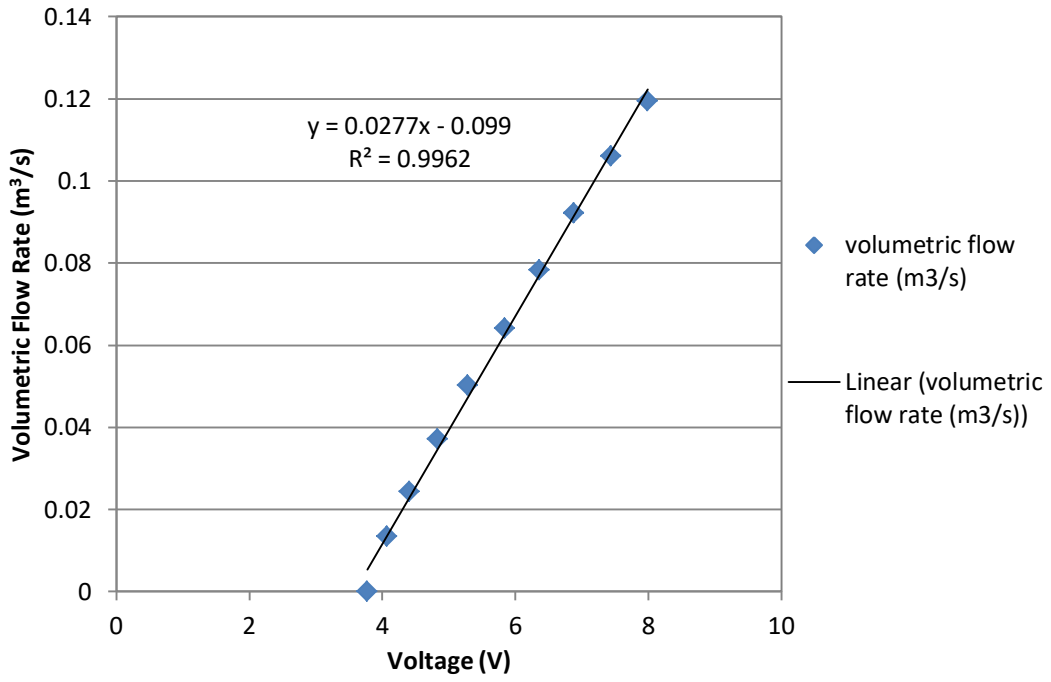
Figure D. 1: Volumetric Flow Rate Measured through the Meriam Laminar Flow Sensor vs Voltage Read from ΔP Transducer

D.2: Kistler Spark Plug Pressure Transducer

In-cylinder pressure measurement was measured using a Kistler Spark Plug Pressure Transducer. The transducer was housed in a modified spark plug head, allowing the in-cylinder gases to press against the sensor without the need to modify the cylinder head.

The following equipment was used to calibrate the pressure transducer:

- Fluke Pressure Pump Model No. P5514-70M (serial no. 71343)
- Fluke Reference Gauge Model 2700G (serial no. 296 5022)
- Kistler Type 5001 Charger Amplifier (serial no. 33228)
- Tektronix TDS 1002B 399811 NR4 Oscilloscope (serial no. TDS1002B CO53526)

The sensitivity, hysteresis error, and curve fitting errors of the transducer were checked by subjecting the transducer to a known pressure and recording the voltage output on the oscilloscope. The charger amplifier was left on for 3 hours before use to warm up and the pressure range was moved through consecutively 3 times. This was repeated on two other days to check for long term variation.

Figure D.2 indicates that there is a linear relationship between the pressure applied to the transducer and the voltage output. This is expected from a piezo-electric transducer.

Table D. 1: Kistler Pressure Transducer Calibration Results

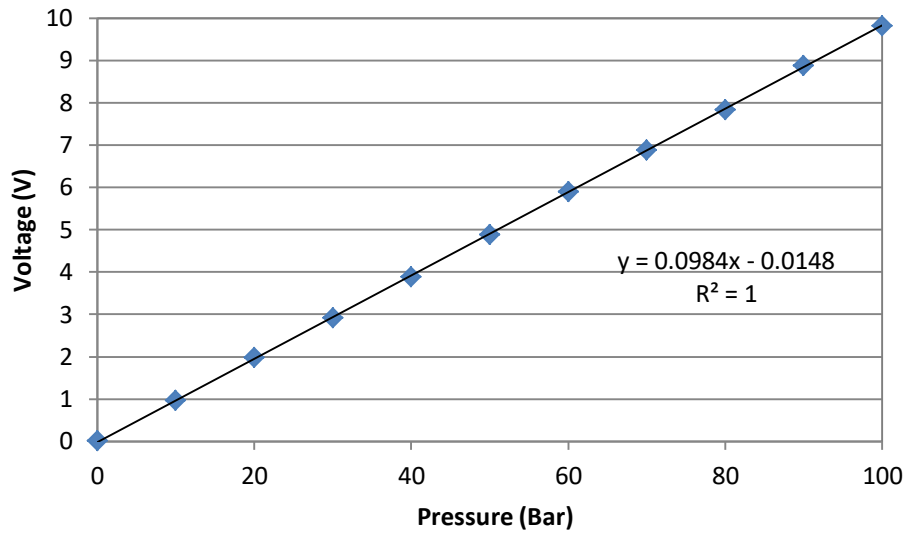| Error	Value
Hysteresis [%]	0.32
Curve Fitting [%]	0.38
Sensitivity [V/Bar]	0.09

Figure D. 2: Kistler Spark Plug Pressure Calibration

D.3: Low and High Temperature Thermocouple Calibration

Thermocouples were used to measure various temperatures in and around the engine test cell. These include both K- and J-type thermocouples that were connected to the thermocouple expansion modules of the PLC.

Low temperature thermocouple measurement includes all temperatures not expected to go above 150 °C and includes coolant temperatures and air temperatures. The following equipment was used to calibrate the low temperature thermocouples.

- Fluke 9142 Field Metrology Well (serial no. B29291)
- MicroLogix 1200 PLC Thermocouple Expansion Module

A reference thermistor probe was used by the field metrology well to read a calibrated temperature that was assumed to be the same for all probes inserted into the well. This reading was output as a resistance which was converted to a temperature as seen in figure D.3.

$$y = -6E\text{-}05x^2 + 0.3916x + 100.06$$
$$R^2 = 1$$
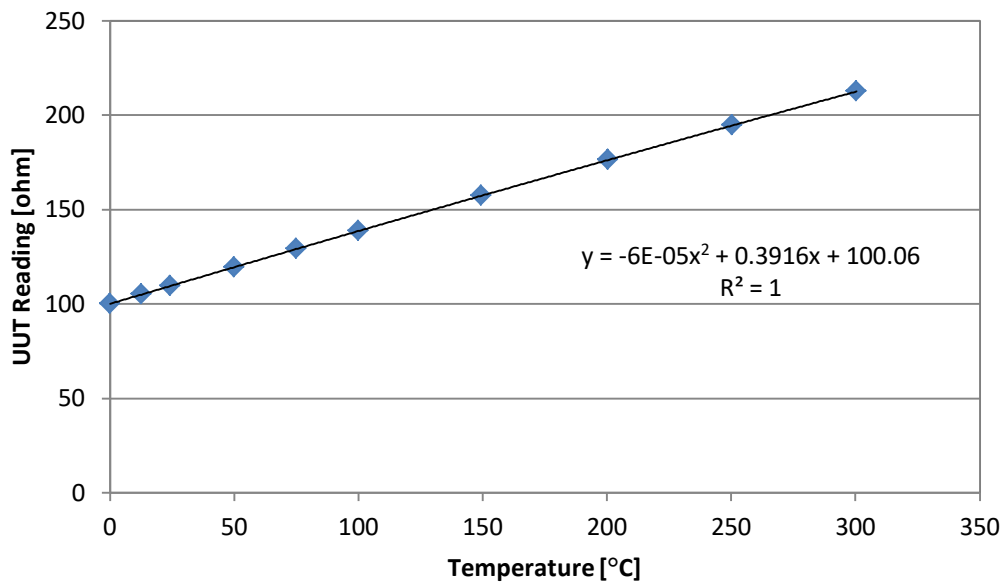
Figure D. 3: Field Metrology Well Thermistor Calibration

97

High temperature thermocouples fall into a category of thermocouples that measure temperatures up to 1000 °C. Exhaust temperatures fall into this category. The following equipment was used to calibrate the thermocouples:

- Fluke Portable Furnace Model 9150 (serial no. B53479)
- MicroLogix 1200 PLC Thermocouple Expansion Module

Figure D.4 shows the relationship between the temperature reading of the thermocouples and the true temperature.

Figure D. 4: High Temperature Thermocouple Calibration

Table D. 2: Low temperature Thermocouple Calibration

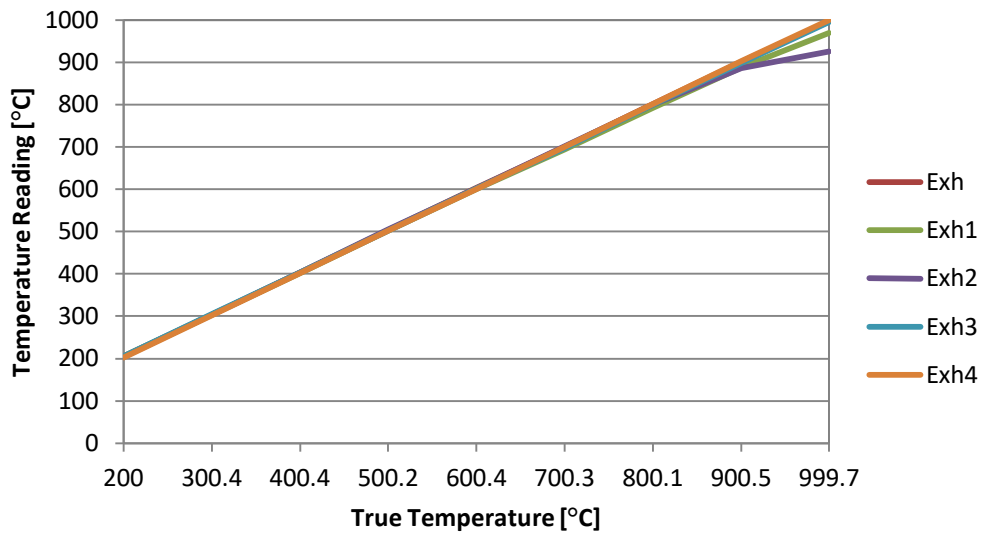| First UUT Reading [Ω]	First Converted Actual Temp [°C]	T cool out [°C]	T cool in [°C]	Shinko [°C]	T oil[°C]	T ambient[°C]	T dyno front[°C]	T dyno rear[°C]	Second UUT Reading[°C]	Second Converted Actual Temp[°C]
103.915	9.97	9.8	8.8	10	10.5	10.0	9.2	9.1	103.916	9.97
107.795	19.91	19.5	18.4	20	20.2	19.7	19.1	19.0	107.795	19.91
111.672	29.88	29.5	28.2	30	30.0	29.5	29.2	28.9	111.67	29.88
115.537	39.85	39.5	38.1	40	39.8	39.3	39.3	38.8	115.535	39.84
119.394	49.83	49.3	48.1	50	49.7	49.1	49.2	48.7	119.391	49.82
123.238	59.81	59.2	58.2	60	59.4	58.9	59.2	58.7	123.232	59.79
127.075	69.80	68.9	68.5	70	69.4	68.8	69.0	68.6	127.069	69.79
130.895	79.79	78.5	78.6	80	79.2	78.6	78.9	78.5	130.892	79.78
134.711	89.79	88.4	88.8	90	89.1	88.5	88.7	88.5	134.705	89.77
138.511	99.78	98.5	99.0	100	99.0	98.5	98.7	98.6	138.507	99.77

Table D. 3: High Temperature Thermocouple Calibration

Temperature [°C]	Exhaust [°C]	Exhaust Cylinder 1 [°C]	Exhaust Cylinder 2 [°C]	Exhaust Cylinder 3 [°C]	Exhaust Cylinder 4 [°C]
200	205.2	204.1	204.6	205.3	202.9
300	304.4	303.5	304.7	304.8	302.6
400	403.1	402.3	403.8	403.9	402.2
500	503.0	501.3	503.0	502.6	501.6
600	602.7	600.3	602.6	601.8	600.8
700	700.8	698.2	700.8	696.5	699.5
800	801.8	795.4	798.7	799.5	801.8
900	901.5	894.8	896.9	898.9	903.1
1000	996.1	992.7	994.4	994.5	1000.1

APPENDIX E: Fuel Mass Flow Statistical Analysis

The AVL 7030-06 fuel mass flow meter can provide the mass of fuel within the fuel container. Due to this measurement occurring over a time period, variations in the mass flow rate can be observed.

Figures E.1 and E.2 show the fuel mass flow rate and average fuel mass flow rate for two engine test conditions. Each data point was recorded at a frequency of 1Hz. The two test conditions which are shown are the lowest and highest fuel flow rates measured in all testing. This was done to show the effect of the fuel flow rate on the variation of the measurement.

Figure E.1 has a calculated coefficient of variation for the data of 2.85% while figure E.2 has a calculated coefficient of variation for the data of 2.33%.
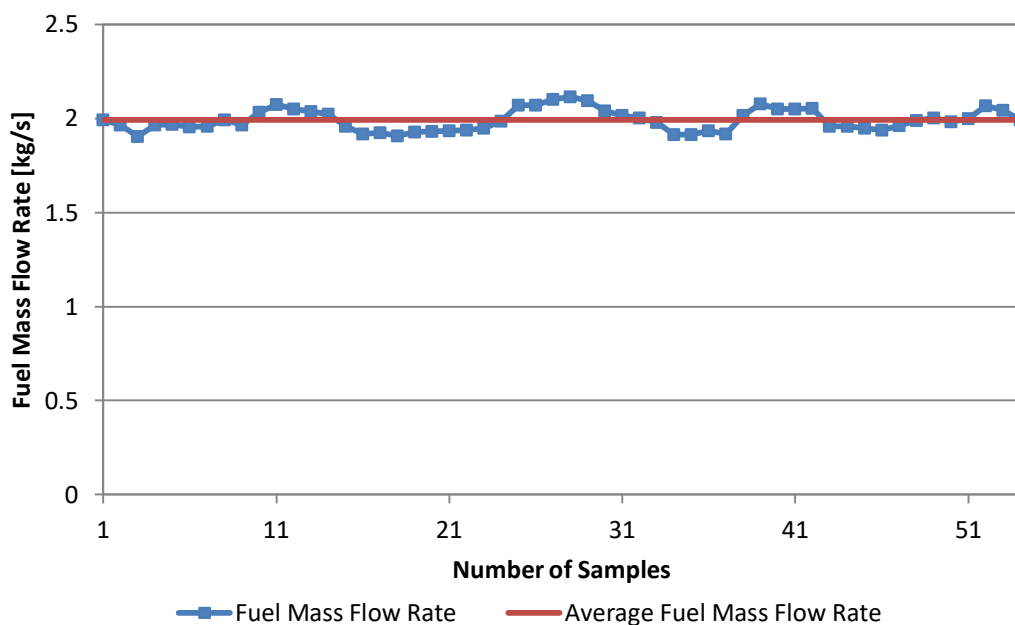

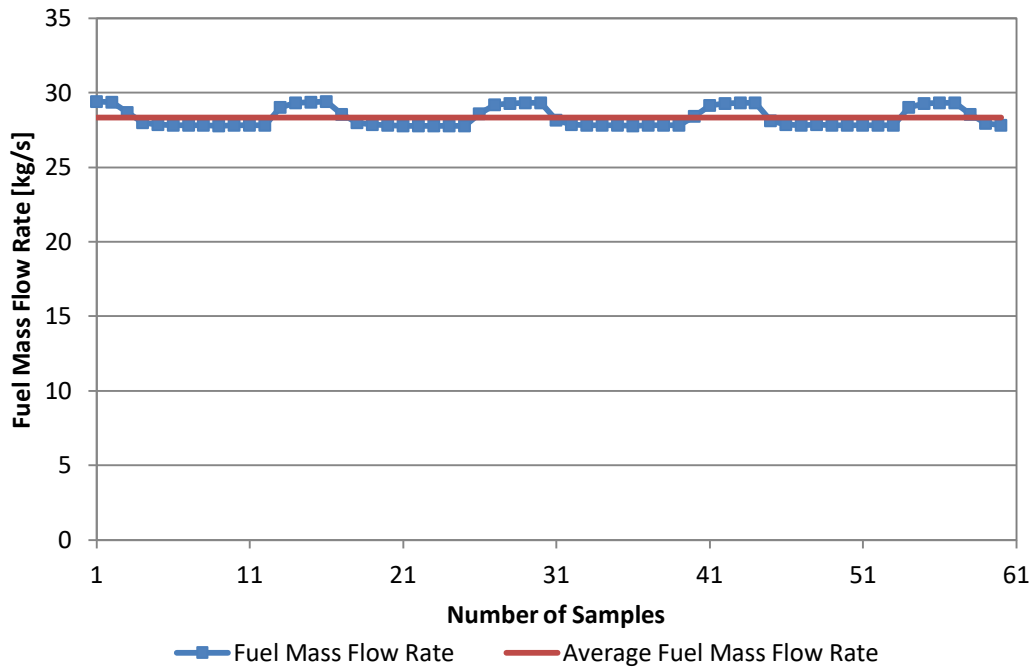**Figure E. 1: Fuel Mass Flow Rate Variation for Numerous Samples (Low Flow Rate)**

Figure E. 2: Fuel Mass Flow Rate Variation for Numerous Samples (High Flow Rate)
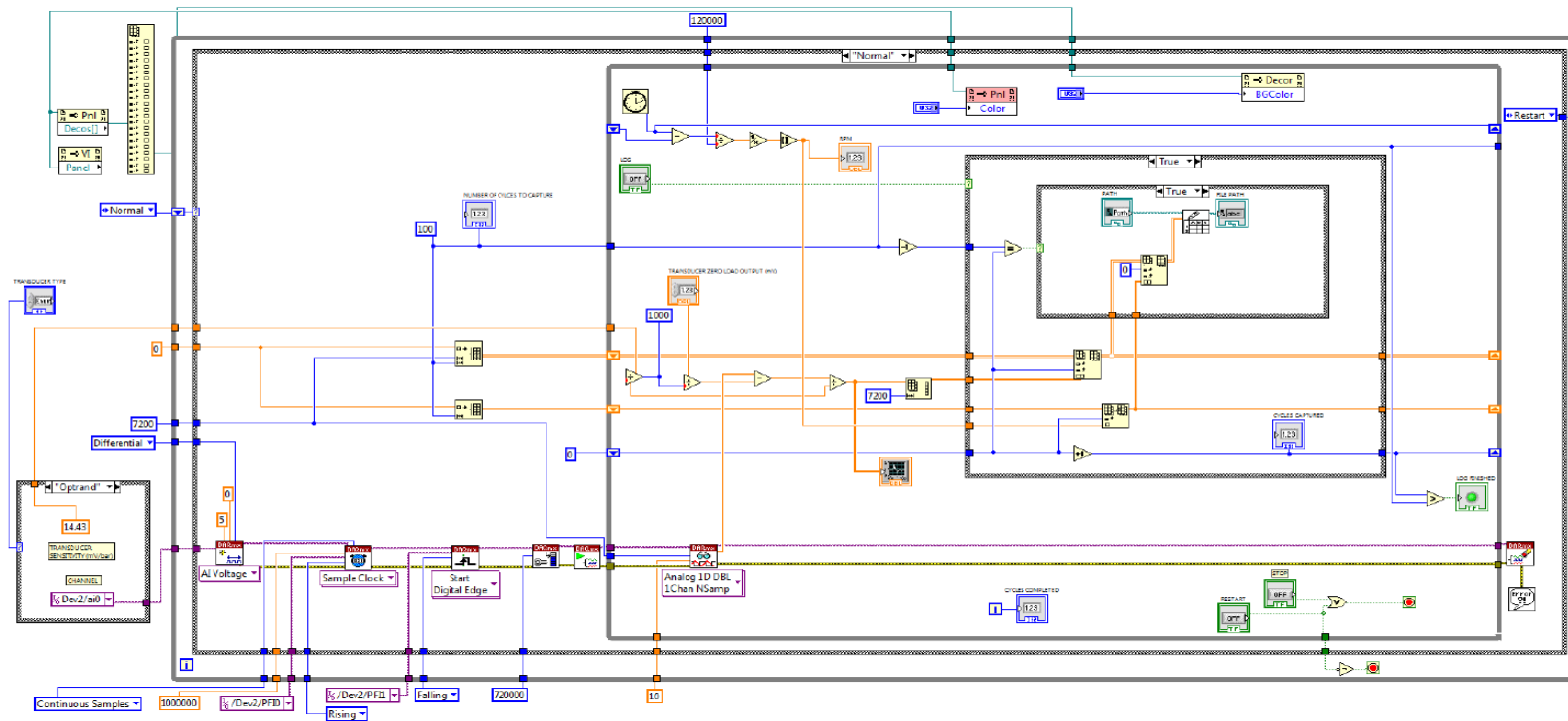
APPENDIX F: Software

F.1: LabView Block Diagram

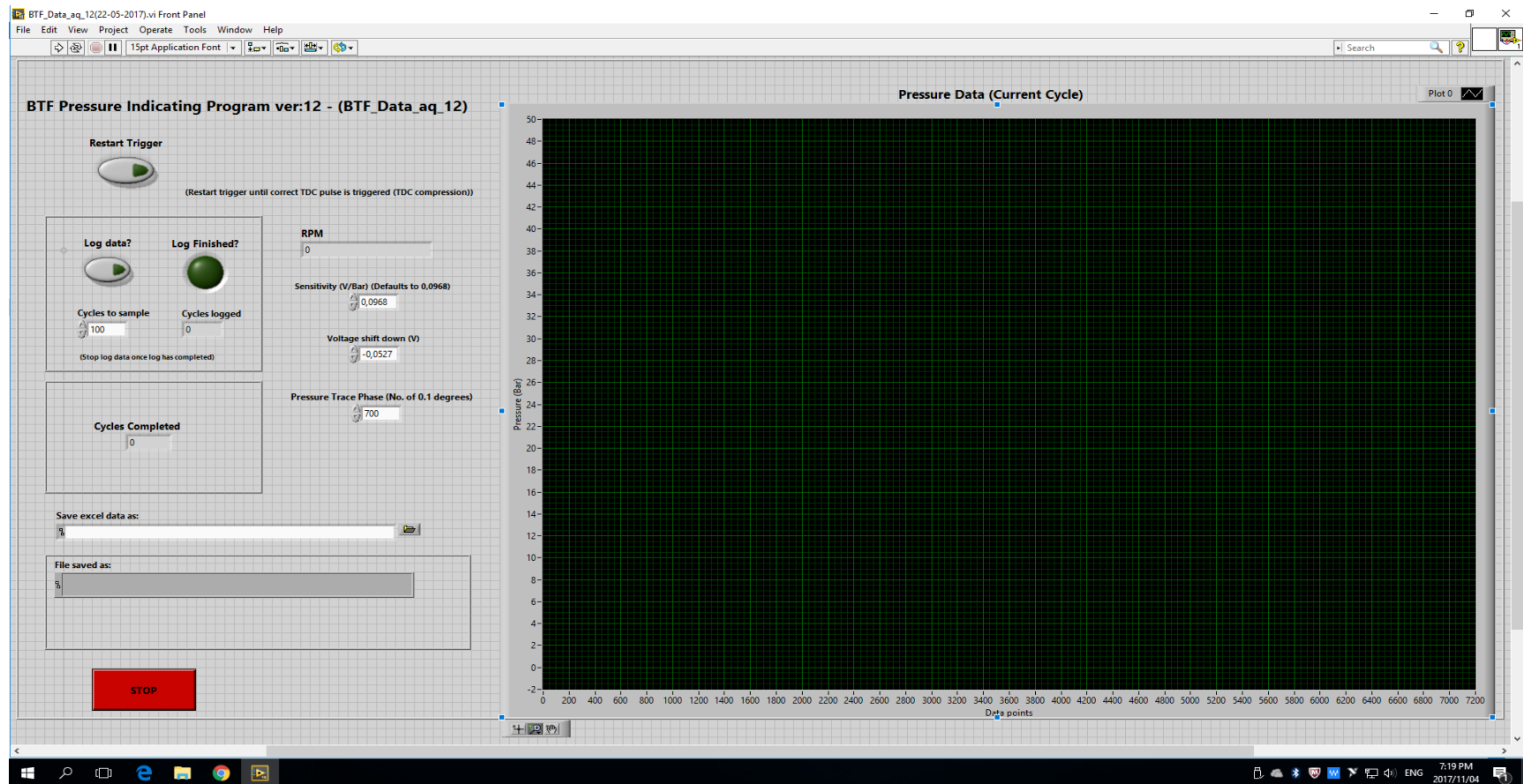**Figure F. 1: LabView Block Diagram**

F.2: LabView Program

Figure F. 2: LabView Graphics User Interface

APPENDIX G: Two-Zone Model Data

Table G. 1: Single-Zone Heat-Release and Two-Zone Model Comparison

Engine Test Condition	Spark-Ignition Timing [°CA BTDC]	Model	Normalised Heat-Release/Mass Fraction Burnt Duration [°CA]					
			0-10%	Difference [%]	0-50%	Difference [%]	0-90%	Difference [%]
2000 rpm - 25 Nm		Single-Zone	28.5		46.8		68.5	
	22	Two-Zone	27.2	4.56	44.8	4.27	62.8	8.32
		Single-Zone	35.2		48.5		64.1	
	44	Two-Zone	34.0	3.41	47.0	3.09	59.7	6.86
2000 rpm - 100 Nm		Single-Zone	21.7		37.1		53.4	
	12	Two-Zone	20.8	4.15	35.7	3.77	49.5	7.30
		Single-Zone	21.7		33.4		47.2	
	26	Two-Zone	21.0	3.23	32.2	3.59	43.3	8.26
4000 rpm - 20 Nm		Single-Zone	33.6		50.5		73.5	
	30	Two-Zone	32.2	4.17	48.6	3.76	67.5	8.16
		Single-Zone	42.3		54.8		72.3	
	50	Two-Zone	41.1	2.84	53.4	2.55	67.2	7.05
4000 rpm - 100 Nm		Single-Zone	24.8		40.8		58.9	
	16	Two-Zone	23.6	4.84	39.2	3.92	54.8	6.96
		Single-Zone	26.9		38.6		54.9	
	32	Two-Zone	25.9	3.72	37.4	3.11	50.3	8.38

REFERENCES

Alkidas, A C, *Combustion advancements in gasoline engines*, Energy Conversion and Management, 48 (2007), 2751-2761.

Allen-Bradley, 2015, *MicroLogix 1200 Programmable Controllers, Bulletin 1762 Controllers and Expansion I/O User Manual*.

Anand, T N C, Deshmukh, M A, Madan, & R V, Ravikrishna 2009 Laser-based spatio-temporal characterization of port fuel injection (PFI) sprays, *International Journal of Spray and Combustion Dynamics*, 2 (2010), 125-150.

Annand, W J D, 1963, *Heat Transfer in the Cylinder of Reciprocating Internal Combustion Engines Journal*: (Proc.I.Mech.E 177.973 (1963)).

ANSI and IEC Colour Codes, OMEGA, www.omega.com, 15 June 2017.

AVL, 2002. *Engine Indicating: User handbook*. Graz: AVL.

Banapurmath, N R, Noolageri, P G, Terwari, P G, & Yaliwal, V S, 2010. *Development of Carburetor for Optimum Performance of Producer Gas Fueled Dual Fuel Compression Ignition Engine*. Maharastra, India: Onward Technologies Ltd.

Beccari, A & Pipitone, E, 2009, Determination of TDC In Internal Combustion Engines by A Newly Developed Thermodynamic Approach. *Applied Thermal Engineering*, Elsevier.

Blair, G P, 1999, Design and Simulation of Four-Stroke Engines, *Warrendale: Society of Automotive Engineers*, Inc.

Bosch, 1995, *Automotive electric/electronic systems*. Stuttgart: Robert Bosch GmbH.

Brunt, M F J, Emtage ,A,L, Rai, H, 1998, The Calculation of Heat Release Energy from Engine Cylinder Pressure Data, *SAE Technical paper Series*, 1-14.

Chun, K M, & Heywood, J B, 1987, Estimating Heat-Release and Mass-of-Mixture Burned from Spark-Ignition Engine Pressure Data, *Combustion Sci. and Tech*. 1987, Vol 54, pp 133-143.

Eichelberg, G, 1939, Investigation of Internal Combustion Engine Problems, *Engineering* Oct 1939 Vol 148, 463 & 547.

Ferguson, C R & Kirkpatrick, A T, 2001, *Internal combustion engines applied thermosciences*, 2nd Edition, New York: John Wiley & Sons.

Figliola, R & Beasley, D E, 2011, *Theory and Design for Mechancial Measurements,* 5th Edition, John Wiley and Sons (Asia) Pte Ltd.

Gitano, H, *Dynamometer Basics,* Universiti Sains Malaysia, http://skyshorz.com/university/resources/dynamo_basics.pdf [Accessed 4 March 2016].

Heisler, H, 1995, *Advanced Engine Technology*, Edward Arnold, London.

Heywood, J.B., 2018. *Internal combustion engine fundamentals*. *Second Edition* New York: McGraw-Hill.

Kakaee, A.H, Zareei, J, 2013, Study and the effects of ignition timing on gasoline engine performance and emissions, *European Transport Research Review*, (2013) 5:109–116.

Kenny, W J, 2013. *Development of an Engine Testing Facility for Spark-ignition Engine Fuel*, 18, 47.

Kim, Y, Kim, W, & Lee, Y, 2015, Influences of exhaust gas temperature and flow rate on optimal catalyst activity profiles. *International Journal of Heat and Mass Transfer*, 1985:841-851.

Kistler, 2010, *Engine Combustion Analysis Engine Pressure Measurement for Research and Development,* Kistler Group.

Kröger, D G, 2004, *Air-cooled Heat Exchangers and Cooling Towers, Thermal-flow Performance Evaluation and Design*.

Liu, H, Reitz, R D, & Wang, Z, 2017, Knocking combustion in spark-ignition engines *Progress in Energy and Combustion Science* 61, 78-112.

Lotus Engine Software, Theory, *Help File*, [Accessed 17 February 2017].

Perfect Power, 2017, *XMS5A/B LetRipp2Engine Management System DIY Manual Version 1.2*.

Pfitzner, J, *Poiseuille and his law*, Anaesthesia, 1976 Volume 31, 273-275.

Polcar, A & Tunka, L, 2017, Effect of various Ignition Timings on Combustion Process and performance of gasoline Engine, *Acta Universitatis Agriculturae Et Silviculturae Mendelianae Brunensis*, Volume 65, 545-554.

Probst, C.O. 1991, *Bosch Fuel Injection & Engine Management*, Cambridge Massachusetts, Robert Bentley.

Ramos, J I, 1989, *Internal Combustion Engine Modelling*, New York: Hemisphere Publishing Corporation.

Robert Bosch GmbH (Ed.), 2007, *Bosch Automotive Electric and Electronics, Systems and Components, Networking and hybrid Drive 5th Edition* Springer Vieweg, Germany.

Roby, S, Yee, N, Wei, T, & Zhou, G, 2014, Fuel Heat of Vaporization Values Measured with Vacuum Thermogravimetric Analysis Method, *Energy & Fuels, Energy Fuels* 2014, 28, 3138−3142.

Schäffer, F & Van Basshuysen, R, 2004, *Internal Combustion Engin handbook: basics, Components, Systems and Perspectives*, Pennsylvania, Warrendale, Pa. SAE International.

Schenck Pegasus GmbH, 1997. *Eddy Current dynamometer*. Darmstadt: Schenck,

Sihling, K & Woschni, G, 1979, Experimental Investigation of Instantaneous Heat Transfer in the Cylinder of a High Speed Diesel Engine, *SAE Technical Paper 790833*.

Stone, R, 2012, *Introduction to Internal Combustion Engines,* Palgrave Macmillan, Hampshire.